Politecnico di Milano

SCUOLA DI INGEGNERIA INDUSTRIALE E DELL'INFORMAZIONE
Corso di Laurea Magistrale in Ingegneria Biomedica

Tesi di Laurea Magistrale

A novel semi-automatic MATLAB tool for the analysis of the patient-specific aortic valve cusps biomechanics using solid elements

Candidati:
Giovanni Rossini
Matricola 824381

Marco Sabbatini
Matricola 822713

Relatore:
Prof. Alberto Cesare Redaelli

Correlatori:
Ing. Emiliano Votta
Ing. Francesco Sturla

Anno Accademico 2015–2016

La somma dei due, l'$1 + 1$ degli uomini dà un risultato superiore a 2, certe volte. Succede quando la cordata è affiatata. Succede in montagna quando i cervelli pensano insieme e i polmoni respirano allo stesso ritmo.

E. Previtali

Contents

1 Abstract

Introduction

The aortic root (AR) is the functional and anatomical unit connecting the outlet of left ventricle to the ascending aorta. It includes the aortic valve (AV), the Valsalva sinuses, the aortic annulus, the sino-tubular junction (STJ), the interleaflets triangles and the proximal ascending aorta.

With the aim to better understand AR structural mechanics, different approaches are available in the scientific literature. These involve the following main steps: the definition of AR geometry, the discretization of the reconstructed domain, the consistency between AR geometry and loading conditions, and the modeling of the mechanical response of AR tissues.

The quantitative reconstruction of AR geometry is the first step towards the implementation of a structural model. In terms of geometrical realism, three generations of models can be identified in the literature: first, models relying on a very simple and idealized geometry, typically based on the assumption of i) identical sinus-leaflet unit, ii) plane-symmetry of each unit, and iii) straight longitudinal axis of the AR bulb and of the proximal ascending aorta, as well exemplified by the work of Gyaneshwar [15]. Second, models that still made use of idealized geometrical paradigms, but used measurements from *in vivo* images to set the dimensions of AR substructures, as repoted in the work published by Conti et al. [12]. Third, models based on the complete 3D reconstruction of patient-specific anatomies through the segmentation of clinical images, as presented in the work of Chandran et al. [10]. These models represent the current state of the art.

The discretization of the geometry is the second main step. For the aortic wall and the aortic valve, both topologically 2D shell elements and 3D elements are used in literature. However, these two options are not fully equivalent, in particular when discritizing the aortic valve: using 3D elements implies more complex meshing algorithms and higher computational expense, but also allows for more realistic simulations of valve dynamics and for accounting for the multi-layer structure of the valve leaflets.

When modeling AR tissues mechanical properties, many studies assumed for simplic-

ity a linear, elastic, isotropic behavior for all of the aortic root structures. This may be sufficiently appropriate for the AR wall, which shows a non-marked anisotropy, as discussed in the work of Gundiah [18], but for the valvular structures a more complex formulation is mandatory to take into account both the anisotropy and the hyperelasticity of the tissue, as shown in Chandran [10] and Conti [12].

Analysing AR throughout the cardiac cycle also requires to define the initial loading state to be applied to the reconstructured geometry. Several studies usually assume the end-diastolic configuration of the AR as the initial one, and neglect the stresses acting on the *in vivo* AR in this configuration; in some cases the loading of the aortic wall is completely neglected [24], in other cases the aortic pressure imposed in the simulations ranges from 0 to 40 mmHg, assuming an 80 mmHg off-set represented by the end-diastolic pressure, underestimating aortic wall stresses [26]. These approaches made the modeled loading conditions inconsistent with the modeled AR geometry; the only exception was provided by Labrosse et al. [24], who estimated the unpressurized geometry of the subject-specific AR model through an iterative approach. This method was effective, but computationally very expensive, and not suitable when accounting for fine anatomical details.

In this context, a recent Masters thesis [44] developed at the Computational Biomechanics Laboratory of the Department of Electronics, Information and Bionengineering of Politecnico di Milano, proposed a noval modelling approach. The latter reconstructed the AR geometry from cMRI, made use of a single layer of shell elements to discretize the geometry of aortic valve leaflets, and computed the pre-stress field associated to the loads acting on the reconstructed geometry through a single step procedure.

The principal aim and novelty of the present work is the design, implementation, and tesing of a semi-automated algorithm to generate patient-specific image-based aortic root finite element models completely discretized with hexahedral elements, including the possibility to set the space-dependent patterns of leaflets thickness. Such algorithm had to be integrated in a automated pipeline allowing for the computation of the AV pre-stresses and for the subsequent simulation of AR structural response throughout the cardiac cycle.

In order to test the impact of this novel approach, this method was applied to a small cohort of subjects and its results were compared to the ones yielded by models discretized using AV leaflets either with shell elements or uniformely thick solid elements.

Material and Methods

The whole modelling process was handled by a Matlab© script that automatized the working pipeline going from segmented images to the setting of the finite element simulations to be run in the commercial explicit finite element solver ABAQUS/Explicit© (Simulia, Dessault Systemes). The entire pipeline consisted of five steps: i) acquisition of cine-cMRI data and segmentation of the AR structures in the end-diastolic frame; ii) reconstruction and discretization of AR 3D geometry; iii) definition of tissues mechanical properties definition; iv) generation of the input files for the finite element computation of the pre-stress field acting on the AR in the reconstructed geometrical configuration; v) generation of the input files for the finite element computation of AR biomechanics throughout a cardiac cycle simulation.

The Matlab© script we implemented exploits the external CAD software Gambit© (Ansys, Fluent Inc., Canonsburg, PA, USA), which is run as a batch process. Data are exchanged between Matlab© and Gambit© through ASCII files, accordingly with the flowchart in Figure 1. In the end-diastolic frame, patients MRI images are manually processed by in home Matlab© software, which allows for tracing sinuses of Valsalva, the ascending aorta, annulus, STJ and leaflets. Each traced profile is described by a cubic spline and sampled, so to export the in plane coordinates of a set of points for each traced structure.

These raw data are automatically transformed in the 3D space and filtered in order to eliminate the noise due to manual segmentation. A network of 3D splines is then generated on the aortic wall and on the leaflets, interpolating the filtered points. An optional smoothing operation was implemented in our script in order to assure a corner-free reconstruction of the leaflets surface; this procedure may be necessary when the leaflets are not clearly visible during the manual tracing. Thanks to it two models of the same geometry, one with and one without the smoothing procedure, were written, ready to be imported by the CAD software Gambit©. The 3D surface of the each AR structure

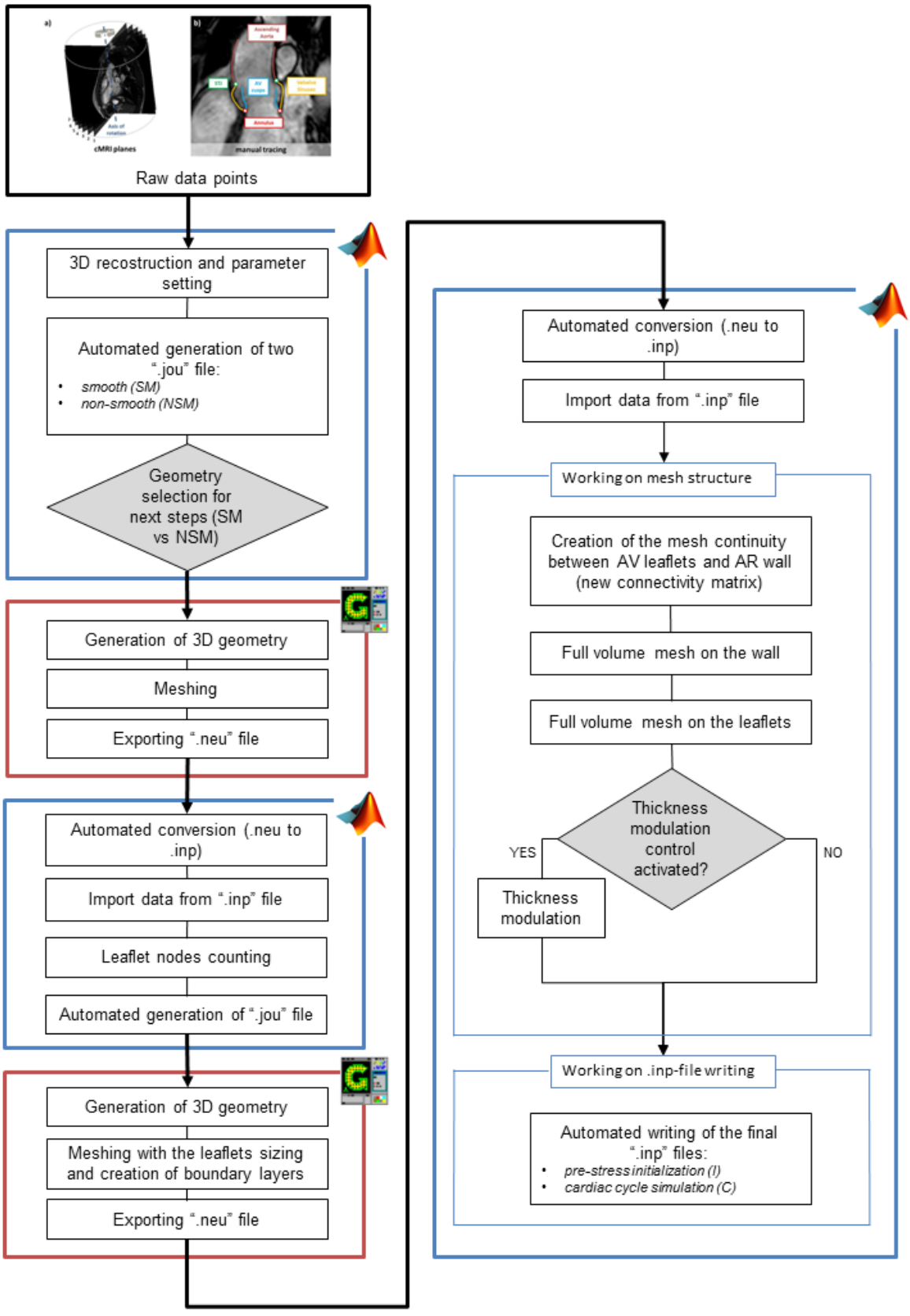

Figure 1: Schematic flow-chart of our automated script. *Blue* boxes involves Matlab© tools, whereas *Green* boxes involves Gambit© tools.

is created on the profile of the splines and discretized with square shell elements; the entire procedure is handles by the CAD software Gambit©, which is fed with a text file (*.jou* format) where all of the operations are described. The input file is automatically generated by the Matlab© tool. The mesh yielded by Gambit© is further processed to connect the leaflets to the aortic wall, manipulating the connectivity matrix, and to generate the solid elements. A full volume mesh for the aortic wall was created using an extrusion procedure along the node normal; instead, depending on the model the user wants to generate, the mesh of the leaflet can be of two types:

- **SH** model: wall made of 8-node solid elements with reduced integration (Abaqus C3D8R elements); leaflets made of 4-node shell elements (Abaqus S4 elements, with only a virtual constant shell thickness).

- **3D-HT** (Homogeneous Thickness) model: wall made of C3D8R elements; leaflets made of three layers of 8-node solid elements (Abaqus C3D8 elements), obtained using a similar extrusion procedure to the one used for the wall elements but, in addition, a manipulation of the direction of the node normal was introduced in order to avoid mesh discrepancies.

- **3D-MT** (Modulated Thickness) model: wall made of C3D8R elements; leaflets made of three layers of 8-node solid elements (Abaqus C3D8 elements), obtained with the same procedure of 3D-HT model; in this case, a space-dependent thickness value for each point of the leaflet surface was assigned taking into account the physiological variations in aortic cusp thickness [16].

Two different material formulations were used in our AR model, one for the aortic wall and another one for the valve leaflets. The mechanical response of the aortic wall was assumed linear, elastic and isotropic, with a 2 MPa Young's modulus and a 0.45 Poisson's ratio to reproduce the almost incompressible behavior of the real tissue [12]. AV leaflets' tissue was described as a transversely anisotropic and hyperelastic material through the model originally proposed by Guccione and colleagues [17] to mimic the passive response of myocardial tissue. This model is based on the following strain energy function U:

$$U = \frac{C}{2}(\exp Q - 1) + K(\frac{J^2 - 1}{2} - \ln J) \tag{1}$$

where C is the first constitutive parameter in MPa, J the $det\boldsymbol{F}$, K the compressibility module and Q is formulated as follow:

$$\begin{aligned} Q = & b_1 * tr(\boldsymbol{E}) + b_2 * E_{ff}^2 + \\ & + b_3 * (E_{ss}^2 + E_{nn}^2 + E_{sn}^2 + E_{ns}^2) + \\ & + b_4 * (E_{nf}^2 + E_{fn}^2 + E_{fs}^2 + E_{sf}^2) \end{aligned} \tag{2}$$

The terms E_{ij} are the components of the Green-Lagrange strain tensor and b_1, b_2, b_3 and b_4 are the other constitutive parameters; so the model just needs six parameters $(C, b_1, b_2, b_3, b_4, K)$ to completely describe the material properties. These were identified based on experimental data from biaxial tensile tests by Billiar et al. [3] [4]. The consistutive model was implemented into a VUANISOHYPER_STRAIN subroutine for ABAQUS/Explicit©.

A density equal to $11\,\mathrm{g/cm^3}$, 10-fold the physiological value [15], was assumed for all AR's tissue taking into account the inertia related to the presence of the blood.

The initial configuration of the AR was defined at early systole, when AV leaflets are approximately unloaded. Hence, cMRI data in the first systolilc frame were used to define AR reference geometry. The finite element computation of the pre-stress field acting on the AR in this configuration was required. To this aim, an iterative process was performed as described in detail in a recent work by Votta et al. [35]; briefly: the stress-free AR configuration was pressurized by applying a pressure load of 82 mmHg to the inner surface of the aorta and of the aorto-ventricular junction; then, the computed nodal displacement field was checked for the entire aortic wall; if the peak value of displacement magnitude did not exceed the in-plane resolution of cMRI, that inflated configuration was considered equivalent to real configuration related to the cMRI, and the corresponding Cauchy true stress field characterizing the aortic wall was considered the pre-stresses field to be applied when simulating AR biomechanics throughout the cardiac cycle. Otherwise, the stress-free AR configuration was updated and set equal to inflated configuration just obtained, and the pressurization simulation was performed again.

After that, the structural response of the pre-stressed AR over two consecutive cardiac cycles was computed; to this aim, physiological time-dependent ventricular and aortic pressures were applied to relevant regions of the aortic wall and a consistent trans-aortic

pressure drop to the leaflets' surfaces.

Results

The mechanical response of the AR during the cardiac cycle was evaluated through the analysis of the stress-strain state. In particular, the attention was focused on the leaflet belly region, the most stressed area of the cusps, at diastolic peak, the moment showing the highest stress values. In SH models, the stress distribution (Figure 2) showed a patchy distribution, and a clear separation between the belly region and the coaptation area could not be detected. Conversely, in the solid elements models (3D-HT, 3D-MT) the distribution was much more regular. In addition, calculated stress values proved the strong impact of the thickness modulation procedure on the 3D-MT model biomechanichs; in particular, max principal, radial and circumferential stresses were notably increased in the thinned belly region. For all subjects, for example, the circumferential stress values averaged over the three leaflets' bellies for the 3D-MT models are more than 4-fold as compared to the corresponding values for 3D-HT models, and more than 2-fold as compared to the corresponding value for SH models (Table 1).

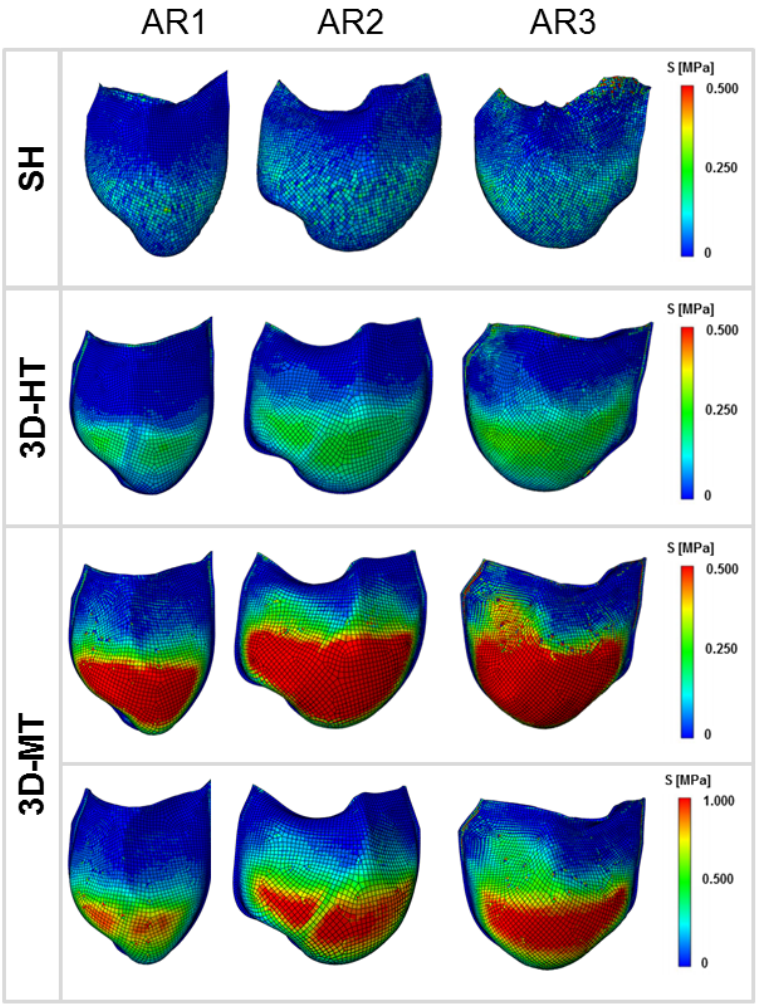

Figure 2: Max principal stress computed at the diastolic peak for the AR1 subject (*left column*), AR2 subject (*central column*), AR3 subject (*right column*). *First line*: max principal stress distribution on the mid surface of the three SH models. *Second line*: max principal stress distribution on the mid solid level of the three 3D-HT models. *Third line*: max principal stress distribution on the mid solid level of the three 3D-MT models. *Fourth line*: max principal stress distribution on the mid solid level of the three 3D-MT models in a different stress scale to better highlight the stress distribution in these models.

	subject AR1			**subject AR2**			**subject AR3**		
	SH	3D-HT	3D-MT	SH	3D-HT	3D-MT	SH	3D-HT	3D-MT
$\overline{\sigma}_{max\_principal}$ **[MPa]**	0.407	0.204	0.857	0.332	0.176	0.712	0.414	0.210	1.048
$\overline{\sigma}_{circ}$ **[MPa]**	0.362	0.200	0.829	0.277	0.173	0.709	0.353	0.208	1.037
$\overline{\sigma}_{rad}$ **[MPa]**	0.137	0.065	0.245	0.149	0.076	0.286	0.172	0.092	0.336

Table 1: Average max principal, circumferential and radial stress across the three leaflet (LC, RC and NC) for all subjects. $\overline{\sigma}_{max\_principal}$ = averaged max principal stress. $\overline{\sigma}_{circ}$ = averaged circumferential stress. $\overline{\sigma}_{rad}$ = averaged radial stress.

As one of the primary aims of this work was the investigation of the stress distri-

bution across the leaflet thickenss, the circumferential and radial stress were evaluated across the leaflet surface in all the models. The measures were performed at the diastolic peak in three different points (A, B, C) of the left-coronary leaflet (Figure 3.a); at each location, the stress values were extracted on the aortic side, on the ventricular side and at the mid-section of the leaflet. This three positions were geometrically distinct in models using solid elements, and corresponded to different integration points in models using shell elements.

a)

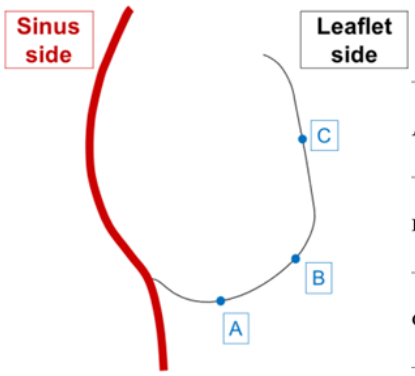

b)

	Location	AR1 models: σ_{circ}			AR1 models: σ_{rad}		
		SH	3D-HT	3D-MT	SH	3D-HT	3D-MT
	V side	0.252	0.144	0.315	0.133	0.074	0.149
A	*mid section*	0.045	0.066	0.241	0.026	0.040	0.117
	A side	0.109	0.029	0.183	0.140	0.021	0.090
	V side	0.526	0.229	0.770	0.115	0.063	0.232
B	*mid section*	0.096	0.170	0.640	0.025	0.050	0.198
	A side	0.169	0.135	0.548	0.127	0.037	0.170
	V side	0.022	0.009	0.051	0.005	0.001	0.023
C	*mid section*	0.016	0.021	0.071	0.005	0.002	0.029
	A side	0.038	0.046	0.106	0.035	0.010	0.036

Figure 3: a) schematic longitudinal section representing the locations (*green* points) across the leaflet surface in which the stresses were evaluated. b) subject AR1; circumferential stress(σ_{circ}) and radial stress (σ_{rad}) within the cross section of the LC leaflet at diastolic peak. *V side* = ventricular side of the leaflet surface. *mid section* = middle section of the leaflet surface. *A side* = aortic side of the leaflet surface.

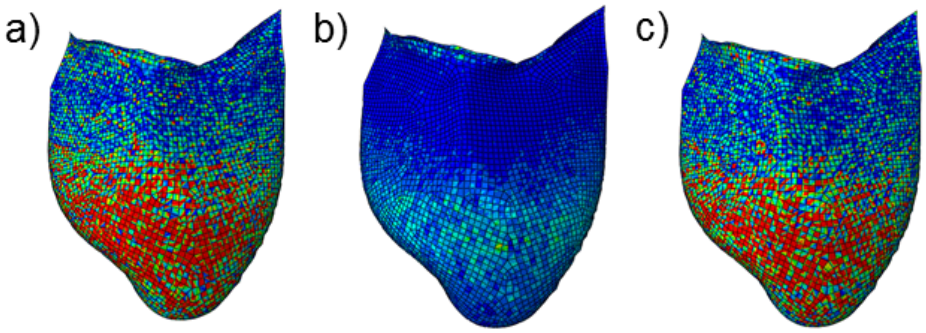

Figure 4: Stress distribution on the V side (a), mid-section (b) and A side (c) for the SH model of the AR1 LC leaflet.

The most evident stress gradient through the leaflet thickness was obtained at location A and B, consistently with the marked local curvature (Figure 3.b). Of note, in SH models the V side and the A side exhibited an even more patchy and noisy stress distribution as compared to the mid section (Figure 4); hence, side-to-side stress

variations are not reliable in these models, and only results for 3D-HT and 3D-MT models can be considered reliable.

Conclusions

As already said, the principal aim and novelty of the present work is the design, implementation, and testing of a semi-automated algorithm to generate patient-specific image-based aortic root finite element models completely discretized with hexahedral elements, including the possibility to set the space-dependent patterns of leaflets thickness. Such algorithm had to be integrated in a automated pipeline allowing for the computation of the AV pre-stresses and for the subsequent simulation of AR structural response throughout the cardiac cycle. A particular attention was payed to the analysis of stress and strain patterns in the leaflets belly, which is the region that experiences the highest stress and strain values during the cardiac cycle, and was mechanics strongly depends on its thickness. Computed results highlighted that the use of solid elements indeed lead to a more reliable quantification of leaflet stresses and of the associated gradient through the leaflet thickness. Moreover, it was evident that leafelt stresses strongly depend on the local leaflet thickness, thus suggesting that in the context of patient-specific modeling a reliable quantification of the patient-specific tissue thickness distribution should be mandatory. Hence, the most important improvement concerns the imaging technique; as already said, cMRI cannot provide any information about the patient leaflets' thickness distribution and a higher resolution imaging technique, e.g. 3D ultrasound imaging, have to be considered in order to be able to trace also the patient-specific tissue thickness distribution. In addition, other modelling improvement could be implemented in order to overcome the following limitations: i) a more complex extrusion function could be implemented for the aortic wall, in order to obtain a thickness value closer to the real one; ii) a more realistic material formulation should be implemented for the wall elements, taking into account its anisotropy; iii) different material formulations for the three layers of the leaflet could be defined taking into account the high differences among the stress-strain curves of the the three laminae of the leaflet [30].

2 Sommario

Introduzione

La radice aortica (AR) è l'unità funzionale ed anatomica che connette l'uscita del ventricolo sinistro all'aorta ascendente; in particolare contiene i lembi della valvola aortica (AV), i seni di Valsalva, l'annulus aortico, la giunzione sino-tubulare (STJ), i triangoli interleaflet e il tratto prossimale di aorta ascendente.

Con lo scopo di comprendere al meglio ogni aspetto dell'analisi della meccanica della AR, diversi approcci sono stati sviluppati in letteratura analizzando i seguenti aspetti: definizione della geometria della AR, discretizzazione del dominio ricostruito, consistenza tra la geometria della AR e condizioni di carico, e modellazione della risposta meccanica dei tessuti della AR.

La ricostruzione quantitativa della geometria della AR rappresenta il primo step nell'implementazione di un modello strutturale. Per quanto concerne il realismo geometrico, in letteratura possono essere individuate tre generazioni successive di modelli: dapprima questi si basavano su una geometria molto semplice e idealizzata derivante dalle seguenti assunzioni di i) unità seni-lembi identiche fra loro, ii) simmetria planare di ogni unità, e iii) asse longitudinale dritto per i seni aortici e l'aorta prossimale, di cui si può avere un esempio nel lavoro di Gyaneshwar [15]. I modelli sviluppati in seguito, pur usando ancora geometrie paradigmatiche e idealizzate,utilizzavano misure *in vivo* per dimensionare le varie strutture della AR, come visto nel lavoro di Conti [12]. La terza e più attuale generazione comprende modelli geometrici basati sulla ricostruzione 3D completa di anatomie paziente-specifico attraverso la segmentazione di immagini cliniche come presentato nel lavoro di Chandran [10].

La discretizzazione della geometria rappresenta il secondo importante step. Parete e valvola aortica vengono discretizzate sia con elementi 2D shell che con solidi 3D. Questi due tipi di soluzioni non sono del tutto equivalenti, soprattuto per quanto riguarda la discretizzazione della valvola aortica: utilizzare elementi 3D comporta maggiori costi computazionali e un più complesso algoritmo di meshing, d'altro canto però permette di effettuare simulazioni della dinamica valvolare più realistiche e di ottenere strutture valvolari multi-strato.

Per quanto riguarda la definizione delle proprietà del materiale, molti studi assumevano per semplicità un comportamento lineare elastico e isotropo per tutte le strutture della AR. Questo metodo può risultare sufficientemente adatto per quanto riguarda la parete aortica, che non mostra un livello di anisotropia estremamente marcato [18], mentre una fomulazione più complessa è richiesta per modellare i lembi valvolari, dove è necessario tener conto sia dell'anisotropia che dell'iperelasticità, come fatto nei lavori di Chandran [10] e Conti [12].

L'analisi della dinamica della AR durante il ciclo cardiaco richiede anche la definizione di uno stato iniziale di sforzo da applicare al geometria 3D ricostruita e discretizzata. Diversi studi assumono la configurazione della AR a fine diastole come configurazione iniziale, trascurando gli sforzi agenti sulla struttura *in vivo*. In altri lavori invece la pressione imposta durante le simulazioni di ciclo cardiaco variava tra 0 a 40 mmHg, assumendo una pressione di off-set pari a 80 mmHg rapprentativa dalla pressione di fine diastole, con la conseguente sottostima delle condizioni di carico della parete aortica [26]. Questi approcci rendono le condizioni di carico inconsistenti con la geometria della AR ricostruita, con la sola eccezione del lavoro di Labrosse [24], in cui la geometria paziente-specifico della AR non pressurizzata è stata modificata iterativamente. Questo metodo si è rivelato efficace, ma molto pesante dal punto di vista computazionale e non adatto se si vuole tenere in conto di un alto dettaglio anatomico.

Il principale scopo ed elemento di novità del presente lavoro riguarda la progettazione, l'implementazione e il test di un algoritmo semi-automatico per la generazione di modelli agli elementi finiti paziente-specifico di AR basati su immagini cMRI e completamente discretizzati con elementi solidi esaedri, includendo la possibilità di ottenere una modulazione dello spessore dei lembi valvolari. Tale algoritmo è stato poi integrato in un processamento dei dati automatizzato atto alla elaborazione dei pre-stress e alla successiva valutazione della risposta strutturale della AR lungo tutto il ciclo cardiaco. Con lo scopo di analizzare l'efficacia di questo nuovo approccio modellistico, tale metodo è stato applicato ad una piccola gamma di soggetti e i corrispettivi risultati sono stati poi comparati con quelli ottenuti su modelli con lembi valvolari discretizzati sia con elementi shell che con elementi solidi esaedri a spessore omogeneo.

Materiali e Metodi

L'intero processo di modellizzazione viene gestito da Matlab© (The MathWorks, Natick, Massachusetts, USA) che rende automatico tutto il processamento dei dati, dalla segmentazione delle immagini al settaggio delle simulazioni agli elementi finiti che vengono poi eseguite mediante il solutore esplicito ABAQUS/Explicit© (Simulia, Dessault Systemes). L'intera catena di processi è composta da cinque fasi: i) acquisizione dei dati dalle immagini cMRI e segmentazione delle strutture della AR all'istante di fine diastole; ii) ricostruzione e discretizzazione della geometria della AR; iii) definizione delle proprietà meccaniche dei tessuti; iv) generazione del file input per la valutazione dei pre-stress agenti sulla geometria ricostruita attraverso il metodo agli elementi finiti; v) generazione del file input per la valutazione della biomeccanica della AR lungo tutto il ciclo cardiaco attraverso il metodo agli elementi finiti.

Lo script in Matlab© da noi implementato sfrutta il software CAD Gambit© (Ansys, Fluent Inc., Canonsburg, PA, USA), eseguito in batch. I dati vengono interscambiati tra Matlab© e Gambit©, medianti file ASCII, coerentemente con quanto mostrato nel diagramma di flusso in Figura 5. All'istante di fine diastole, le immagini MRI dei pazienti sono manualmente processate mediante il software Matlab©, che permette il tracciamento dei seni di Valsalva, dell'aorta ascendente, dell'annulus, del STJ e dei lembi. Ogni profilo così tracciato viene poi descritto da spline cubiche e campionato, in questo modo vengono estratte le coordinate 2D del set di punti per ogni struttura tracciata.

Questi dati, ancora grezzi, sono automaticamente trasformati nello spazio 3D e filtrati in modo da eliminare eventuali rumori dovuti alla segmentazione manuale. Interpolando i punti filtrati, una rete di spline 3D viene generata sulla parete aortica e sui lembi. Un'opzionale procedura di "smoothing" è stata implementata nel nostro script con lo scopo di assicurare una ricostruzione dei lembi senza eccessive irregolarità geometriche. Questa procedura può risultare necessaria quando i lembi non sono chiaramente visibili durante il tracciamento manuale. Grazie a questa procedura due modelli della stessa geometria vegnono prodotti, uno con e uno senza la procedura di "smoothing", pronti per essere implementati mediante il software CAD Gambit©. La superfice 3D di ogni struttura della AR viene creata sulla base del profilo delle spline e discretizzata con

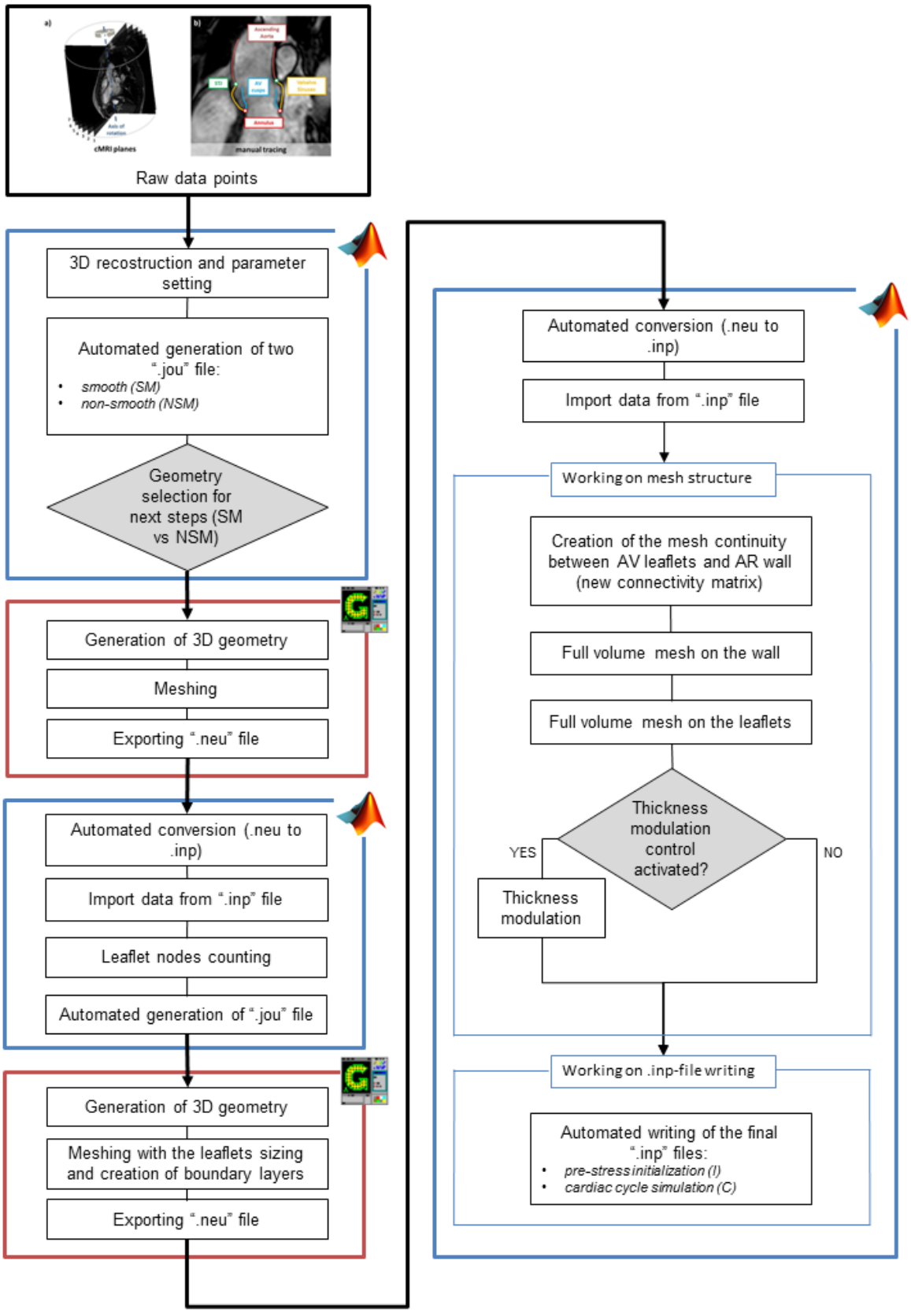

Figura 5: Flow chart schematico del nostro script semi-automatico. I riquadri *blu* coinvolgono operazioni in Matlab©, mentre i riquadri in *verde* coinvolgono operazioni in Gambit©.

elementi shell quadrati; l'intero processo viene eseguito dal software CAD Gambit©, al quale viene fornito il testo file (formato *.jou*) in cui sono descritte tutte le instruzioni da eseguitre. Il file input viene automaticamente generato mediante il tool di Matlab©. La mesh ottenuta mediante Gambit© viene successivamente processata per connettere i lembi alla parete aortica, manipolando la matrice di connettività, e per generare gli elementi solidi. Una mesh completamente solida per la parete aortica viene creata mediante una procedura di estrusione lungo la normale ai nodi; invece, in base al modello che si vuole generare, la mesh dei lembi può essere di due tipologie:

- modello **SH**: parete creata con elementi solidi a 8 nodi con integrazione ridotta (elementi C3D8R di Abaqus); i lembi vengono creati con elementi shell a 4 nodi (elementi S4 di Abaqus, con solo uno spessore virtuale costante).

- modello **3D-HT** (Homogeneous Thickness): parete creata con elementi C3D8R; i lembi vengono creati con tre layer di elementi solidi a 8 nodi, ottenuti utilizzando un metodo di estrusione simile a quello usato nell'inspessimento della parete, ma, in aggiunta, una procedura di manipolazione delle direzioni delle normali ai nodi è stata introdotta per evitare eventuali discrepanze nella mesh.

- modello **3D-MT** (Modulated Thickness): parete creata con elementi C3D8R; i lembi vengono creati con tre layer di elementi solidi a 8 nodi, ottenuti utilizzando lo stessa procedura del modello 3D-HT; in questo caso, con lo scopo di considerare le variazioni fisiologiche dello spessore delle cuspidi valvolari come riportato in letteratura [16], ad ogni singolo nodo della superfice del lembo viene assegnato un valore di spessore in relazione alla sua posizione all'interno della superfice del lembo stessa.

Due differenti formulazioni del comportamento del materiale sono state utilizzate nel nostro modello di AR, una per descrivere il comportamento della parete aortica e una per i lembi. La risposta meccanica della parete è stata modellata con un materiale elastico lineare e isotropo, con un modulo di Young di 2 MPa e un modulo di Poisson di 0.45; ciò ha reso possibile riprodurre il comportamento quasi incomprimibile del tessuto reale. I lembi valvolari sono stati descritti con un materiale iperelastico e trasversalmente anisotropo mediante il modello originariamente proposto da Guccione

[17] per modellizzare la risposta passiva del tessuto miocardico. Questo modello utilizza la seguente *strain energy function* U:

$$U = \frac{C}{2}(\exp Q - 1) + K(\frac{J^2 - 1}{2} - \ln J) \tag{3}$$

dove C è il primo parametro costitutivo espresso in MPa, J è il $det\boldsymbol{F}$, K il modulo di comprimibilità e Q è formulato come segue:

$$\begin{aligned} Q = {} & b_1 * tr(\boldsymbol{E}) + b_2 * E_{ff}^2 + \\ & + b_3 * (E_{ss}^2 + E_{nn}^2 + E_{sn}^2 + E_{ns}^2) + \\ & + b_4 * (E_{nf}^2 + E_{fn}^2 + E_{fs}^2 + E_{sf}^2) \end{aligned} \tag{4}$$

I termini E_{ij} sono le componenti del tensore delle deformazioni di Green-Lagrange, mentre b_1, b_2, b_3 e b_4 sono altri parametri costitutivi; con questo modello i sei parametri $(C, b_1, b_2, b_3, b_4, K)$ sono sufficienti per caratterizzare completamente il materiale. Quest'ultimi sono stati identificati sulla base dei risultati sperimentali ottenuti da test biassiali su cuspidi naturali di Billiar e colleghi [3] [4]. Il modello costitutivo è stato poi implementato in una subroutine VUANISOHYPER_STRAIN per ABAQUS/Explicit©. Una densità pari a $11\,\mathrm{g/cm^3}$, cioè 10 volte la densità fisiologica [15], è stata utilizzata per tutti i tessuti della AR, in modo da tenere in conto dell'inerzia relativa alla presenza del sangue. La configurazione iniziale della AR è stata definita ad inizio sistole, quando i lembi valvolari possono essere considerati scarichi. Infatti, le immagini cMRI utilizzare per la ricostruzione della geometria si rifanno all'istante di inizio sistole. Il campo di pre-stress relativo a questa configurazione è stata poi acquisito mediante un processo iterativo descritto con maggiore dettaglio nel recente lavoro di Votta e colleghi [35]. Brevemente: la configurazione *stress-free* della AR ricostruita è stata pressurizzata applicando una pressione statica di 82 mmHg alla superficie interna della aorta e della giunzione tra aorta e ventricolo; in seguito è stato valutato il valore massimo dello spostamento nodale per l'intera parete aortica: se il valore di tale picco non eccedeva la risoluzione delle immagini cMRI, la configurazione pressurizzata è stata considerata equivalente alla configurazione reale e il campo di pre-stress (sforzi di Cauchy) ottenuto viene considerato corretto da applicare alla geometria prima di simulare il ciclo cardiaco completo. Diversamente, se il valore di picco di spostamento risulta maggiore della risoluzione, la configurazione *stress-free* viene aggiornata alla configurazione trovata e

la pressurizzazione viene effettuata nuovamente.
Una volta trovata il campo di pre-stress relativa alla configurazione acquisita dalle immagini cMRI, la risposta strutturale del modello di AR è stata valutata su due cicli cardiaci consecutivi; a questo scopo, una curva di pressione tempo-dipendente fisiologica ventricolare e una aortica sono state applicate alle rispettive regioni di interesse della parete aortica e una coerente differenza fisiologica di pressione transvalvolare è stata applicata ai lembi aortici.

Risultati

La risposta meccanica della AR nel ciclo cardiaco è stata valutata attraverso l'analisi dello stato di sforzo e deformazione. In particolare, ci si è concentrati sulla pancia dei lembi, che rappresenta la zona più sollecitata, al picco diastolico, momento in cui si registrano i maggiori valori di sforzo sui lembi. I modelli SH presentano una distribuzione di sforzo (Figura 6) a "macchia di leopardo", e una chiara separazione tra la zona della pancia e l'area di coaptazione non può essere determinata. Contrariamente, nei modelli ad elementi solidi (3D-HT, 3D-MT) la distribuzione di sforzo è molto più regolare. Inoltre, i valori di sforzo calcolati mostravano il forte impatto della procedura di modulazione dello spessore sulla biomeccanica del modello 3D-MT; in particolare, i valori di sforzo principale massimo, circonferenziale e radiale risultato notevolmente maggiori nelle zone della pancia dove lo spessore è minore. Per tutti i soggetti in esame, ad esempio, il valore di sforzo circonferenziale mediato tra le pance dei tre lembi per il modello 3D-MT è più di 4 volte maggiore del corrispettivo valore nel modello 3D-HT, e più di 2 volte maggiore del corrispettivo modello SH (Tabella 2). Dato che uno degli obbiettivi principali del presente lavoro era quello di investigare la distribuzione di sforzo lungo lo spessore del lembo per i tre modelli, sono stati valutati lo sforzo circonferenziale e radiale attraverso al superficie dei lembi. Le misure sono state effettuate al picco di diastole in tre diversi punti (A, B, C), per il lembo sinistro di ogni modello (Figura 7.a); in ogni punto, i valori di sforzo sono stati estrati sul versante aortico ("aortic side"), sul versante ventricolare ("ventricular side") e sulla sezione media ("mid section") del lembo.

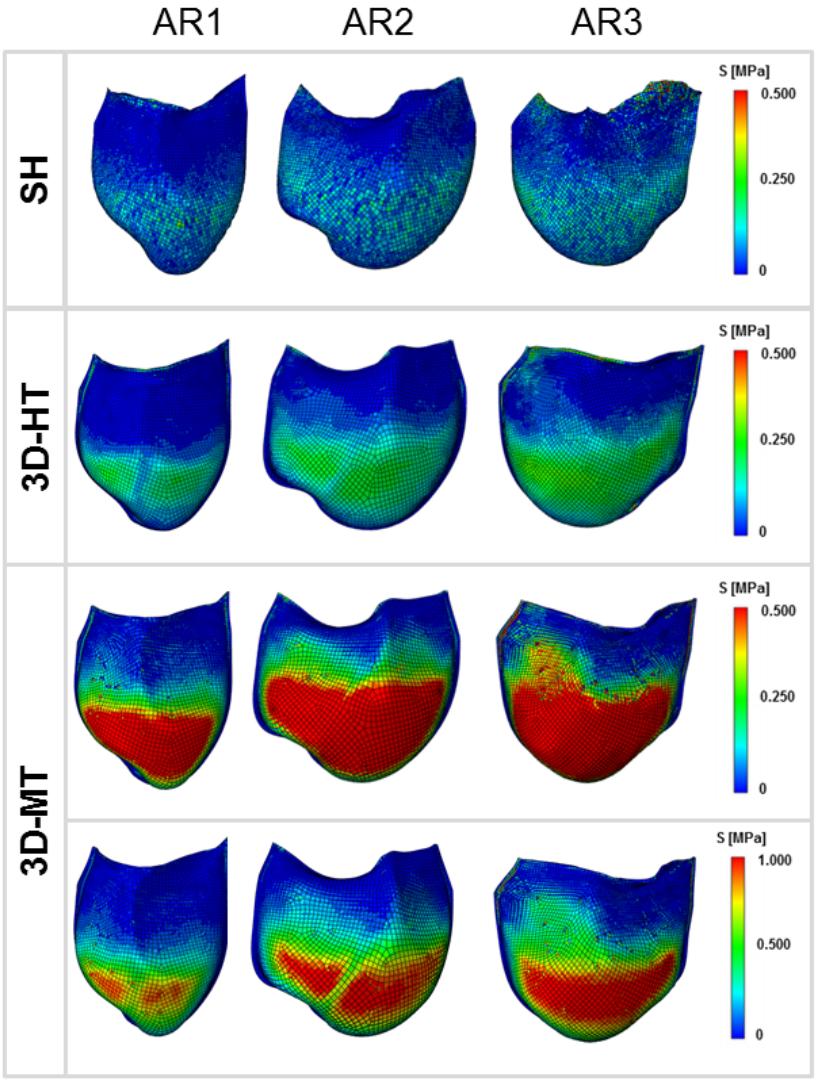

Figura 6: Valor di sforzo principale massimo al picco diastolico per i soggetti AR1 (*lato sinistro*), AR2 (*centro*), AR3 (*lato destro*). *Prima riga*:distribuzioni dello sforzo principale massimo sulla superficie media dei tre modelli SH. *Seconda riga*:distribuzioni dello sforzo principale massimo sulla superficie media dei tre modelli 3D-HT. *Terza riga*:distribuzioni dello sforzo principale massimo sulla superficie media dei tre modelli 3D-MT. *Quarta riga*:distribuzioni dello sforzo principale massimo sulla superficie media dei tre modelli 3D-MT con una scala diversa, in modo da evidenziare la distribuzione di sforzo in questi modelli.

	subject AR1			**subject AR2**			**subject AR3**		
	SH	3D-HT	3D-MT	SH	3D-HT	3D-MT	SH	3D-HT	3D-MT
$\overline{\sigma}_{max\_principal}$ **[MPa]**	0.407	0.204	0.857	0.332	0.176	0.712	0.414	0.210	1.048
$\overline{\sigma}_{circ}$ **[MPa]**	0.362	0.200	0.829	0.277	0.173	0.709	0.353	0.208	1.037
$\overline{\sigma}_{rad}$ **AVG [MPa]**	0.137	0.065	0.245	0.149	0.076	0.286	0.172	0.092	0.336

Tabella 2: Valori di sforzo principale massimo, circonferenziale e radiale mediati fra i tre lembi per (LC, RC e NC) ogni soggetto. $\overline{\sigma}_{max\_principal}$ = sforzo principale massimo medio. $\overline{\sigma}_{circ}$ = sforzo circonferenziale medio. $\overline{\sigma}_{rad}$ = sforzo radiale medio.

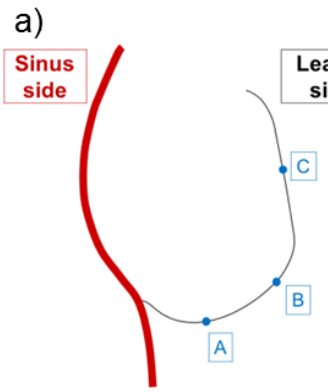

b)

	Location	AR1 models: σ_{circ}			AR1 models: σ_{rad}		
		SH	3D-HT	3D-MT	SH	3D-HT	3D-MT
	V side	0.252	0.144	0.315	0.133	0.074	0.149
A	*mid section*	0.045	0.066	0.241	0.026	0.040	0.117
	A side	0.109	0.029	0.183	0.140	0.021	0.090
	V side	0.526	0.229	0.770	0.115	0.063	0.232
B	*mid section*	0.096	0.170	0.640	0.025	0.050	0.198
	A side	0.169	0.135	0.548	0.127	0.037	0.170
	V side	0.022	0.009	0.051	0.005	0.001	0.023
C	*mid section*	0.016	0.021	0.071	0.005	0.002	0.029
	A side	0.038	0.046	0.106	0.035	0.010	0.036

Figura 7: a) Rappresentazione schematica di una sezione longitudinale con indicati i punti sulla superfice del lembo (punti *verdi*) in cui sono stati calcolati gli sforzi. b) soggetto AR1; valori di sforzo circonferenziale (σ_{circ}) e radiale (σ_{rad}) lungo la sezione trasversale del lembo coronario sinistro al picco di diastole per il soggetto AR1. *V side* = versante ventricolare dalla surperfice del lembo. *mid section* = layer medio della superfice del lembo. *A side* = versante aortico della superfice del lembo.

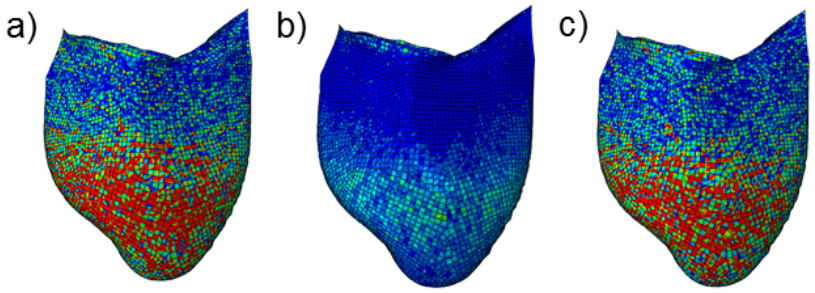

Figura 8: Distribuzione dello sforzo massimo principale sul versante ventricolare(a), sulla sezione media (b) e sul versante aortico (c) del lembo coronario sinistro del soggetto AR1.

Queste tre posizioni sono geometricamente distinte nei modelli ad elementi solidi, mentre corrispondono a tre differenti punti di integrazione nei modelli ad elementi shell (Figura 7.b). Il gradiente di sforzo più accentuato si trova nelle posizioni A e B, esattamente in corrispondenza delle zone con una più marcata curvatura (Figura 7.b). Da notare che, nei modelli SH il versante ventricolare e quello aortico presentano una distribuzione ancora più rumorosa e "a macchia di leopardo" della corrispettiva sezione media ("mid section") (Figura 8); per questo motivo, le variazioni tra una strato e l'altro del lembo non sono affidabili nei modelli SH, e un ottimo grado di affidabilità può quindi essere conferito solo ai modelli ad elementi solidi (3D-HT, 3D-MT).

Conclusioni

Come già menzionato, il principale scopo ed elemento di novità del presente lavoro riguarda la progettazione, l'implementazione e il test di un algoritmo semi-automatico per la generazione di modelli agli elementi finiti paziente-specifico di AR basati su immagini cMRI e completamente discretizzati con elementi solidi esaedri, includendo la possibilità di ottenere una modulazione dello spessore dei lembi valvolari. Tale algoritmo è stato poi integrato in un processamento dei dati automatizzato atto alla elaborazione dei pre-stress e alla successiva valutazione della risposta strutturale della AR lungo tutto il ciclo cardiaco. Un'attenzione particolare è stata posta sull'analisi dello stato di sforzo e deformazione nella pancia dei lembi, regione dove sono presenti le maggiori sollecitazioni durante il ciclo cardiaco e che viene modificata maggiormente durante il processo di modulazione dello spessore. I risultati ottenuti hanno dimostrato che l'utilizzo di elementi solidi comporta una più affidabile quantificazione degli sforzi sul lembo e del corrispondende gradiente di sforzo lungo il suo spessore. Inoltre, è risultato evidente che gli sforzi sono fortemente dipendenti dal valore locale di spessore del lembo, suggerendo la forte necessità di introdurre una più affidabile quantificazione paziente-specifico dello spessore dei lembi. In questo contesto si inserisce un possibile miglioramento riguardante le tecniche di imaging utilizzate per l'acquisizione dei dati dal paziente: come già discusso, le immagini cMRI non permettono di ottenere alcuna informazione circa lo spessore nei lembi del paziente, dunque tecniche con una maggiore risoluzione, ad esempio il *3D ultrasound imaging*, dovrebbero essere prese in considerazione con lo scopo non solo di tracciare la posizione dei lembi, ma anche di ottenere informazioni paziente-specifico della distribuzione dei valori di spessore lungo i lembi stessi. In aggiunta, ulteriori miglioramenti possono essere apportati per superare le seguenti limitazioni: i) implementare una funzione di estrusione per i nodi della parete aortica più complessa, al fine di ottenere uno spessore più vicino a quello fisiologico; ii) utilizzare una modello costitutivo per gli elementi della parete aortica più realistico del semplice legame elastico lineare isotropo, che tenga conto dell'anisotropia del tessuto vascolare; iii) implementare un legame costitutivo diverso per ciascuno dei tre strati dei lembi valvolari, così da includere nel modello le differenze nel comportamento meccanico tra le tre tunicae dei lembi valvolari [30].

3 Anatomy and Physiology

3.1 Heart anatomy and physiology

The heart is placed in the middle of the chest (anterior mediastinum), between the lungs and above diaphragm. It has a conic shape, with the apex pointing downwards and the transversal axis oriented from the right to the left and from the interior to the exterior of the chest (Figure 9).

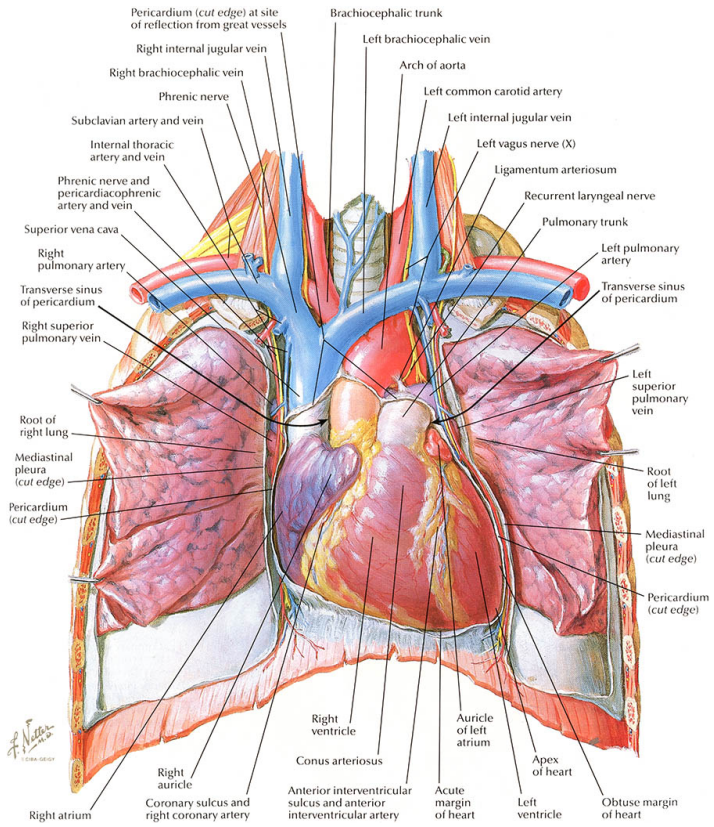

Figure 9: Anterior view of toracic cavity with heart in the middle [39].

From a functional standpoint, the heart consists of two pulsatile volumetric pumps in series. Each of them consists of two connected chambers: the atrium, which is located superiorly, receives blood from the veins and successively moves it into the second cavity, i.e. the ventricle, which is located inferiorly and pumps blood in the arteries that supply the organs within the body. Namely, the right ventricle pumps the blood to the lungs through the pulmonary arteries, while the left ventricle pumps the blood to all of the body peripheral systems through the aorta and the corresponding

branches. The right and left hearts are separated by a wall called *septum* (Figure 10).

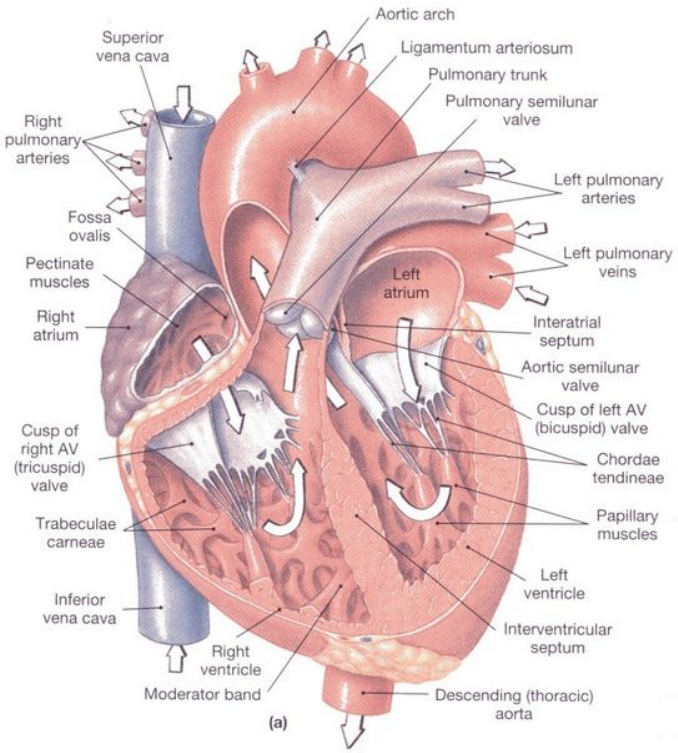

Figure 10: Anatomy of the heart [39]. Arrows indicate the direction of blood flow through the cardiac chambers.

Between each atrium and the corresponding ventricle there is an atrioventricular valve that allows for the unidirectional blood flow from the former latter. The atrioventricular valve is called tricuspid valve (i.e. with three leaflets) and mitral valve (with two leaflets) in the right and left heart, respectively. Between each ventricle and the corresponding outgoing vessel there is a semilunar valve that guarantees the blood unidirectional flow out of the heart. The semilunar valve is called pulmonary and aortic valve in the right and left heart, respectively, owing to the artery connected to the valve. Both these valves are made of three leaflets. The opening and closure of the valves are mostly a passive phenomena driven by pressure differences between the upstream and downstream compartments separated by the valve. Based on such pressure differences, and hence on the valves' closed or open configuration, the cardiac cycle characterizing heart function can be divided in three functional phases:

- *atrial diastole*: atrioventricular valves are closed to allow for the filling of the atrial with the blood coming from the pulmonary veins (left atrium) and venae

cavae (right atrium); pressure increases along with atrium filling.

- *atrial systole and ventricular diastole*: atrioventricular valves open under the atrial pressure and blood flows from the two atria to the two ventricles filling them completely. When the ventricular pressure exceeds the atrial pressure the atrioventricular valves close again to prevent from atrial regurgitation.

- *ventricular systole*: the ventricular wall undergo a fast contraction and the ventricular pressure increases fast (isovolumetric contraction). When pressure in the left ventricle exceeds the aortic pressure (80 mmHg) and pressure in the right ventricle exceeds the pulmonary artery pressure (8 mmHg) the two semilunar valves open allowing for blood ejection. Subsequently, the ventricular pressure starts to decrease to the diastolic levels and a new cardiac cycle starts.

In Figure 11 the time-course of aortic pressure, ventricular volume, ventricular and atrial pressure for the left heart is plotted. At the bottom of the figure also the ECG and phonocardiogram are represented. The right heart is characterized by similar patterns, but with lower absolute values.

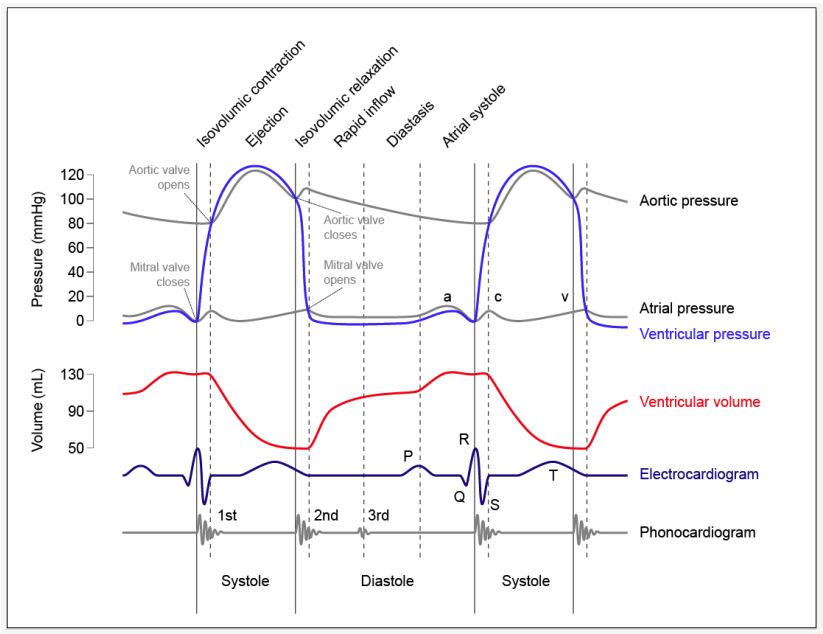

Figure 11: Time-dependency of aortic pressure, left atrial pressure, left ventricular pressure and left ventricular volume. Plots are synchronized with a phonocardiogram and an ECG. Values are referred to a standard healthy adult subject.

3.2 Aortic root anatomy

The aortic root is the functional and anatomical unit connecting the outlet of left ventricle to the ascending aorta and hosting the sub-structures of the aortic valve (Figure 12).

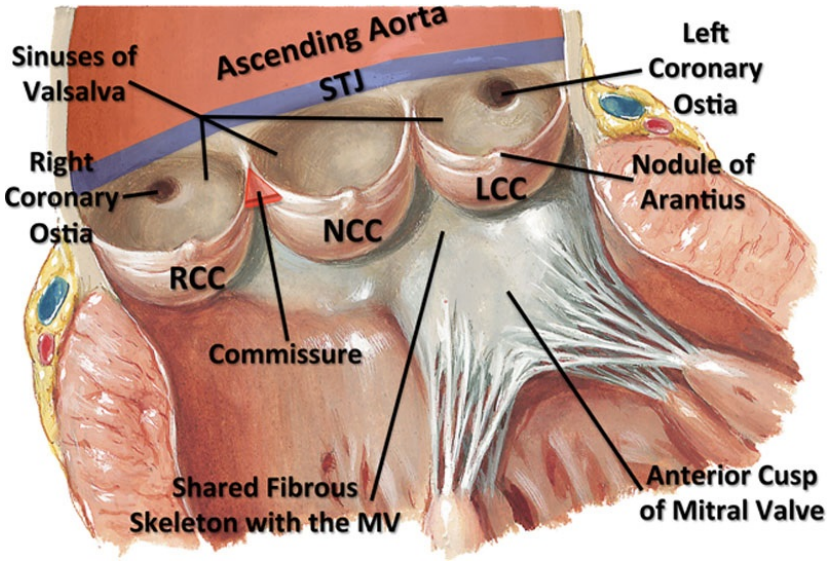

Figure 12: Anatomy of the aortic root along its long axis. The interleaflet triangle between the non- and left coronary cusp is continuous with the anterior leaflet of the mitral valve. The commissures are the coaptation lines that run parallel between the leaflets. LCC = left coronary cusp; NCC = noncoronary cusp; RCC = right coronary cusp; STJ = sino-tubular junction; MV = mitral valve [39].

The aortic wall encompassing the aortic root can be divided in two main portions: a tri-lobated bulb, consisting of the three Valsalva sinuses, and the tubular ascending aorta, which represents the most distal portion of the aortic root. The Valsalva sinuses are called left-coronary, right-coronary and non-coronary, based on their position and on the fact that two sinuses each contain the orifice of a main arterial coronary. According to the measurements performed by Berdajs et al. [2] on 25 specimens of human aortic root under stationary flow rate conditions, each Valsalva sinus has specific dimensions: the right-coronary sinus has the largest volume, which is equal to 15.6 ± 0.34 ml (mean value $\pm$ standard deviation), followed by the non-coronary sinus (1.33 ± 0.27 ml) and by the left-coronary sinus (1.04 ± 0.23 ml). The height (the extension along the axial direction) of right, left and non-coronary sinus is 19.45 ± 1.91 mm, 17.45 ± 1.39 mm and 17.68 ± 1.77 mm, respectively. The thickness of the aortic wall is highly heterogeneous over different regions of the wall: in the proximal zone it ranges

from 0.60 to 1.98 mm; next to the STJ it varies between 1.82 and 2.14 mm [16]. The boundary between these two portions is called sinotubular junction (STJ). The STJ is approximately circular, with a diameter ranging from 14.4 ± 0.4 mm during late diastole to 16.7 ± 0.4 mm during the ejection phase [25], and it is approximately $10-15\%$ smaller than the diameter evaluated at the sinuses base [21]. The Valsalva sinuses host the aortic valve leaflets; these insert on the aortic wall at the proximal end of the Valsalva sinuses, along a crown-shaped line called annulus. The three points at the boundary between adjacent leaflets are called commissures (Figure 13). According to the in vivo measures carried out on 10 patients by using MRI, the inter-commissures distance between the right, left and non-coronary commissure are respectively 24.2 ± 4.0 mm, 21.1 ± 3.0 mm, 22.0 ± 3.6 mm [12].

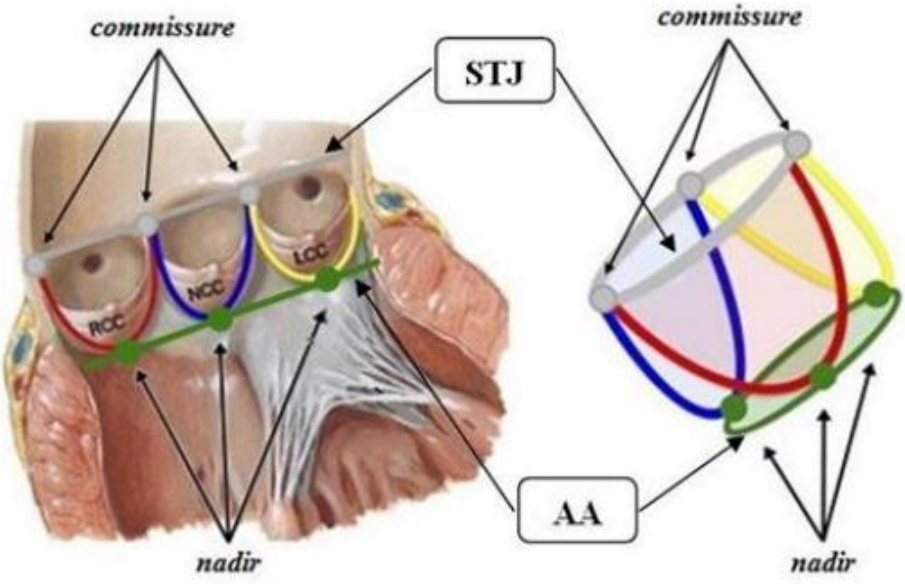

Figure 13: On the *left* hand panel: section of the aortic root showing its main stuctures (aortic annulus - AA - and nadir points in green, sinotubular junction - STJ - and commissures in grey. On the *right* hand panel: schematic representation of the aortic root.

The ideal circle connecting the three nadirs of crown-shaped annulus is called basal ring, which represents its connection between the aortic root and the left ventricle. The portions of the aortic wall delimited distally by the commissures, proximally by the basal ring, and laterally by the insertions of two adjacent leaflets are called inter-leaflets triangles (Figure 14).

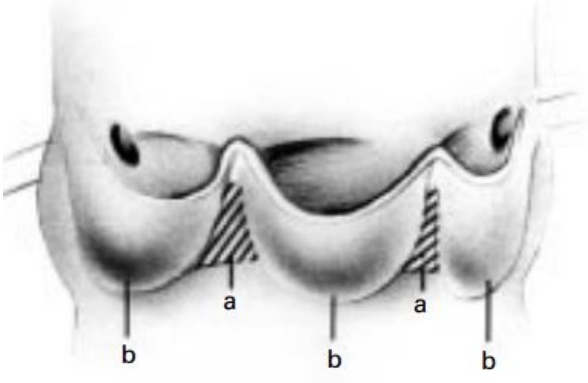

Figure 14: Sketch of the aortic root opened longitudinally through the left coronary sinus, showing the interleaflet triangles (a) and the valve leaflets (b) [34].

3.2.1 Aortic valve anatomy

The aortic valve is located in close proximity of the two atrioventricular valves. In particular, the non-coronary and left-coronary leaflets of the aortic valve face the mitral valve (Figure 15).

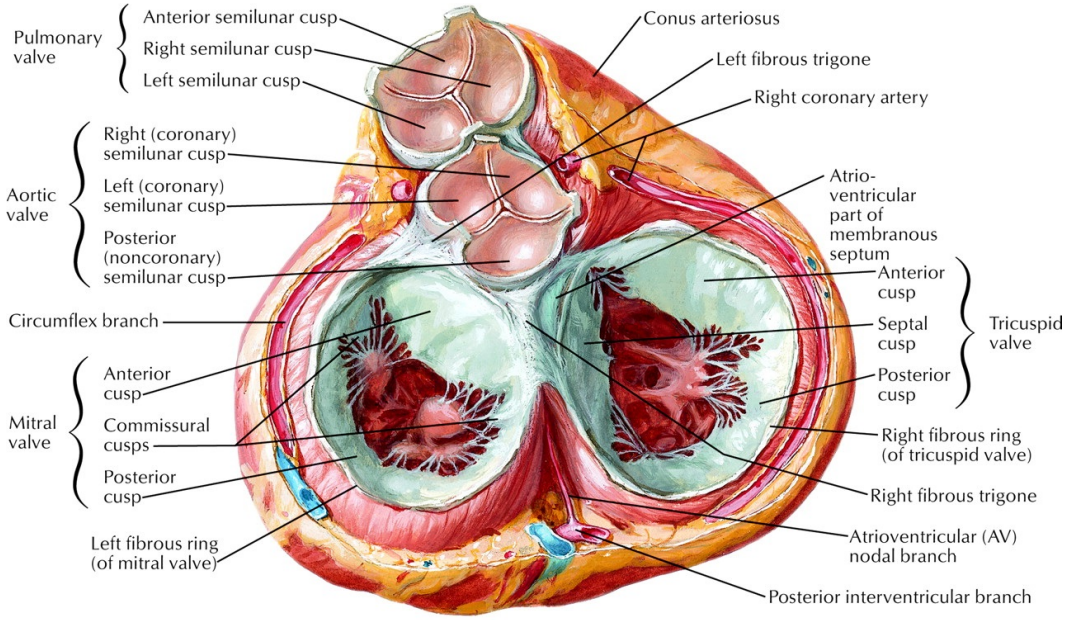

Figure 15: Valvular plane as seen from the atrial side; valves are represented in their diastolic configuration [39]. Three aortic valve leaflets and their respective positions are clearly visible: RC leaflet (right-coronary), LC leaflet (left-coronary) and NC leaflet (non-coronary).

From the structural point of view, the aortic valve is composed by three leaflets classified as the Valsalve sinuses: left-coronary (LC), right-coronary (RC), non-coronary

(NC). In each leaflet, the line of insertion is longer than their free margin. Each leaflet covers approximately one third of aortic valve orifice. Differences in terms of leaflet extent exist, the non-coronary leaflet being wider than the coronary ones, but were reported to be not statistically significant (Table 3).

	RC	LC	NC
Heigth [mm]	13.30 ± 0.60	13.90 ± 0.80	13.70 ± 0.40
Free margin length [mm]	33.00 ± 1.40	31.50 ± 1.40	32.70 ± 1.30
Attachment edge length [mm]	46.40 ± 2.00	47.60 ± 2.20	48.10 ± 1.60
Perimeter [mm]	79.40 ± 3.30	79.10 ± 3.50	80.80 ± 2.80
Area [mm^2]	29.70 ± 1.70	30.90 ± 2.70	31.70 ± 1.80

Table 3: Valve leaflets size [21].

Within each leaflet, four regions are usually identified [33] (Figure 16):

- *basal region*: it is located all along the insertion line of the leaflet and runs from commissure to commissure. It is characterized by an high density of fibrous collagen tissue.
- *belly region*: it is the central portion of the leaflet, as well as the widest and thinnest of the four regions. When inspected, this region is almost transparent.
- *coaptation region*: the portion of the leaflet that gets in contact with the complementary leaflets when the valve is closed, i.e. during ventricular diastole.
- *free margin*: it's the free boundary of the leaflet. The central point of this region is characterized by the so-called nodulus of Arantius, i.e. a thicker and almost spherical anatomical feature that helps achieving the full continence of the valve during ventricular diastole.

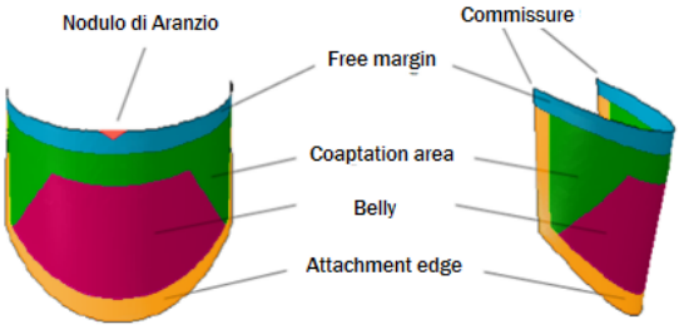

Figure 16: Schematic representation of the four regions of an aortic valve leaflet, as seen from an anterior (left hand panel) and lateral (right hand panel) view.

The leaflets thickness is non-uniform and varies from region to region along the entire anatomy [11] (Table 4).

	LC & RC	NC
Attachment edge [mm]	1.60	1.55
Free margin [mm]	1.53	1.96
Coaptation area [mm]	$0.68 - 1.29$	$0.68 - 1.65$
Belly region [mm]	$0.18 - 0.58$	$0.18 - 0.58$

Table 4: Valve leaflets thickness values reported by *Grande et al.* [16].

3.2.2 Ascending aorta anatomy

The largest artery in the body, the aorta, is the main vessel of the arterial system. It originates from the left ventricle and ends in the abdomen, where it branches into the two common iliac arteries. The aorta can be divided into three main tracts: ascending aorta, aortic arch and descending aorta. The ascending aorta is 5 cm long, with a diameter of 33 mm in females and 36 mm in males [27]; the most proximal 2 cm of its the ascending aorta consist in the aortic root, and the next 3 cm consist in the tubular section. The aortic wall has a thickness ranging from 2.128 mm and 2.137 mm [16]. Being the first vessel that receives the blood ejected by the heart, the aortic wall experiences notable huge mechanical and fluid dynamic stresses.

3.3 Aortic root dynamics

In the work of Dagum et al. [13] on six adult, castrated, male sheep underwent implantation of miniature radiopaque markers in the aortic root, mitral annulus, and left ventricle, different dynamics and deformation processes have been shown to occur in each AR section[13]. In particular four distinct deformation modes have been found: two *circumferential deformation*, one on the aortic root base (annulus) and the other on the commissure level (STJ), one *longitudinal deformation* and a *torsional deformation* characterized by local shear stresses in the aortic root wall (Figure 17). In systole, the dynamics of the aortic root starts with a sudden circumferential expansion of the annulus and of the STJ during the isovolumetric contraction phase.While the STJ expansion is uniform, the annulus undergoes an asymmetric deformation: the expansion is larger in the left sector ($11.2 \pm 2.5\%$) and smaller in the non-coronary sector ($3.2 \pm 1.1\%$). At the same time the aortic root is stretched longitudinally. During the ejection phase the expansion of the STJ continues, whereas the annulus undergoes a non-uniform circumferential contraction: the circumferential shortening is more marked in the left and right sectors ($-9.7 \pm 1.5\%$, $-9.4 \pm 2.2\%$ respectively) than in the non-coronary one ($-3.9 \pm 1.1\%$)[13]. In particular, during the first third of the ejection phase the aortic root is maximimally expanded at all levels, whereas in the last two thirds of the ejection phase the inner volume of the AR decreases slowly at first and then more and more rapidly [25]. In that phase non-homogeneous torsional stresses are present: in the left and non-coronary commissural region the torsion is clockwise (looking at the aortic root from the ascending aorta), whereas in the right commissural region the torsion is anticlockwise. In that phase no significant longitudinal deformation occurs. During the isovolumetric relaxation phase, the aortic root undergoes a further circumferential shrinking, both at the STJ level (symmetric) and annulus (asymmetric) levels. In particular the left side of the annulus feels a larger deformation than the left side ($-9.9 \pm 3.6\%$, $-3.5 \pm 2.1\%$ respectively). Furthermore torsional deformation and a uniform longitudinal compression are present in the wall . In the diastolic phase the aortic root undergoes a longitudinal stretch and a circumferential expansion; shear and torsional deformations in that phase have opposite directions as compared to the ejection phase: anticlockwise in the left and non-coronary commissural regions and

clockwise in the right commissural region.

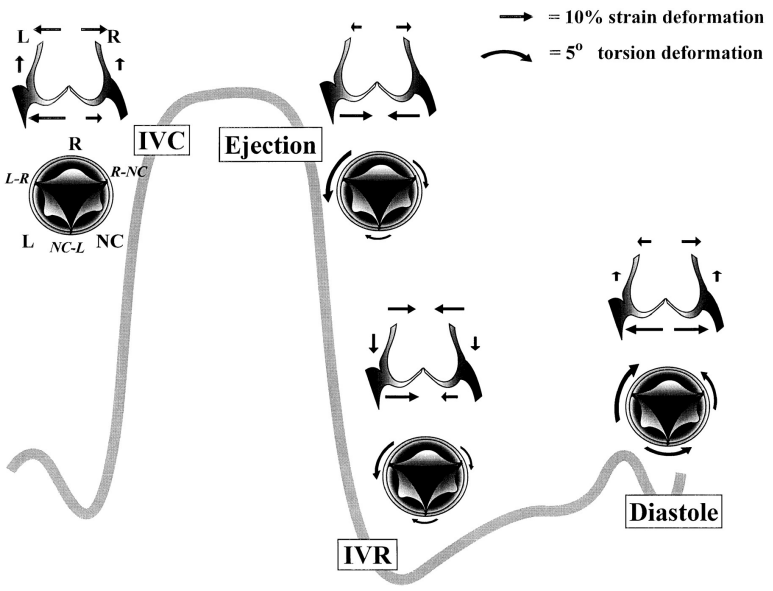

Figure 17: Aortic annular deformation of left (L), right (R), and non-coronary (NC) sectors of aortic annulus. Annular deformation throughout the cardiac cycle is shown at end of IVC (isovolumic contraction) relative to its end-diastolic configuration, at end of ejection relative to end-IVC configuration, at end of IVR (isovolumic relaxation) relative to end-ejection configuration, and at end of diastole relative to end IVR configuration.

A very important role is played by the interleaflet triangles: their dynamics is influenced by the aortic pressure and by the ventricular pressure, in particular when the upper part of the aortic root expands during systole. During systole, the expansion of the upper part of the aortic root allows the leaflets to open, while the contraction of the lower part decreases the distance they will need to cover to coapt. The rounded shape of the sinuses creates an interstice between the leaflet and the wall which allows the formation of vortexes which are very important to avoid dangerous leaflets impact on the wall. After the systolic peak those secondary flows ease the movement of the leaflets, promoting the valve closure [34][33]. The perfect synergy between the different processes described above and shown in (Figure 17) allow to maximize the ejection, optimize the transvalvular hemodynamics and ease the the leaflets movement during the cardiac cycle.

3.4 Microstructure of the aortic root

As usual in a biological environment, cardiovascular tissues are composed of connective tissues characterized by cells and extracellular matrix (ECM). The cellular part of the cardiovascular tissue is mainly composed of endothelial and muscle cells. The ECM is mainly composed by glicosamminoglycans (GAGs), two types of structural proteins, i.e. collagen and elastin, and two types of adhesive proteins, i.e. fibronectin and laminin. The microstructural properties of these macro molecules, together with their spatial organization, determine and the mechanical properties at the tissue level.

3.4.1 Ascending aorta wall structure

The proximal wall of the ascending aorta, which represents the distal part of aortic root, has three layers or *tunicae*, which differ from each other from both in a structural and an histological standpoint (Figure 18):

- *tunica intima (I)*: it represents the inner layer and is 0.33 mm thick [49]. Even though it is composed of a single endothelial layer directly supported by the basal membrane, it has an important mechanical strength owing to the presence of a huge number of circumferential oriented type I and type III collagen fibers.

- *tunica media (M)*: it is the intermediate layer, separated from intima and adventitia by an elastic lamina (inner and outer respectively); it is 1.32 mm thick [49], it is composed of bundles of type I and III collagen fibers, elastin and a packed smooth muscle cell network. All of these constituents are arranged in a helicoidal pattern, which allows this tunica to bear high circumferential stress levels associated to the intraluminal pressure load.

- *tunica adventitia (A)*: it is the outer layer of aorta and it is 0.96 mm thick [49]. Surrounded by lax connective tissue, it mainly contains fibroblasts, fibrocites, amorph substance and thick bundles of type I collagen fiber. It is perfused by the *vasa vasorum*, i.e. a small network of radially oriented arterial capillaries that provide nutrients and oxygen to the tunica.

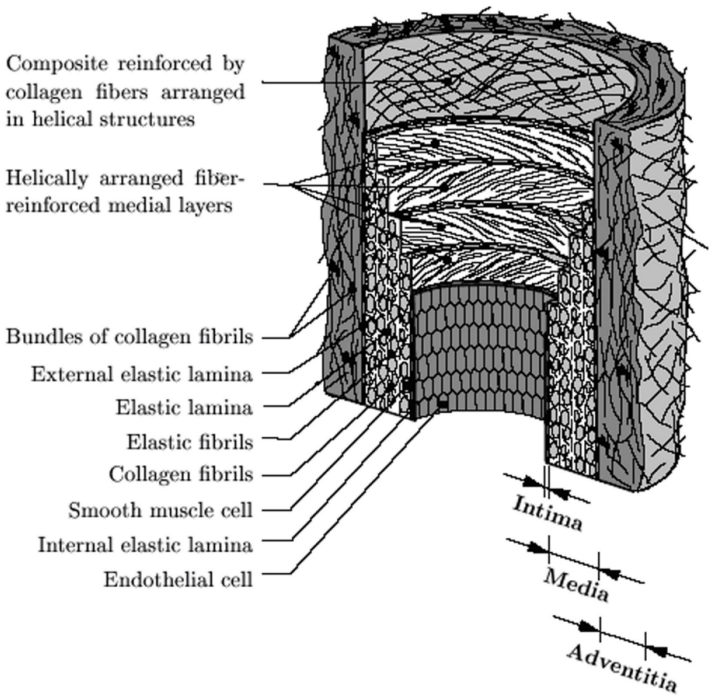

Figure 18: Sketch of the main components of a healthy elastic artery composed of three layers: intima (I), media (M), adventitia (A) [41].

This complexity microstructure leads to different mechanical properties for the tunicae, although they all share three features: non-linearity, anisotropy characterized by a stiffer behavior in the circumferential direction as compared to the axial direction (Figure 19), and extremely high resistance to volumetric deformations. The mechanical properties of the three tunicae can be described based on the study by Holzapftel [40], even though it was focused on the wall layers of 13 specimens of human arterial coronaries from elderly subjects (age 71 ± 7.3 years). In that study it was observed that the tunica intima exhibits a high values of stiffness and the highest degree of anisotropy, while the adventitia has a markedly non linear response due to the progressive recruitment of collagen fibers during loading. The almost incompressible stress-strain behavior of the tunicae is a consequence of the strong aqueous component inside the ECM, which often leads to assumed perfect incompressibility, as shown in the works of Choung and Fung [7]. In particular, some compression tests were performed on rabbit aortae by applying a 30 kPa pressure. Results showed a volume change by to $0.5 - 1.26\%$ associated to the ejection of liquid from the wall, thus supporting the incompressibility hypothesis.

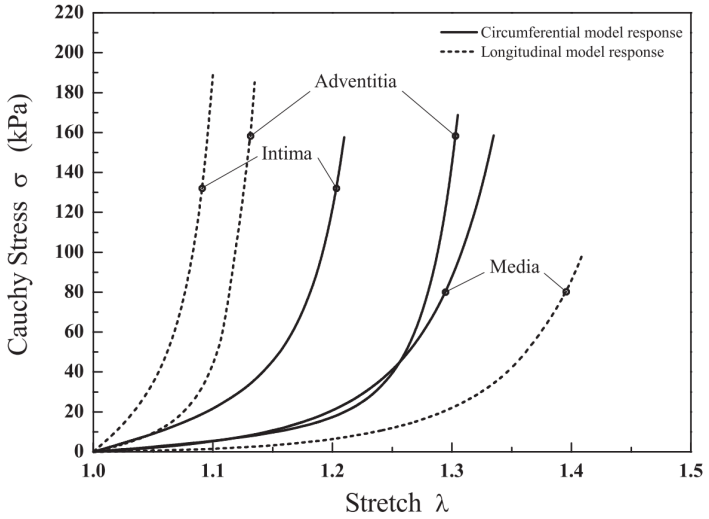

Figure 19: Stress-strain curves for the three tunicae of coronary artery wall [40].

The superimposition of the properties of the three tunicae leads to the global mechanical behavior of the aortic wall at the organ level, which can be described as non-linear elastic, i.e. hyperelastic, anisotropic and incompressible. The recruitment hypothesis of the collagen fibers explains the mechanical behavior of the aortic wall: initially, at low loads, only the elastin extends in order to support the stresses then, increasing the loads magnitude, the collagen fibers, aligning progressively with the stresses direction, start to sustain the loads reaching a straight configuration at high stress values. It follows that elastin allows the artery to stretch, while collagen prevents excessive distortion.

3.4.2 Aortic valve leaflets' structure

The tissue of aortic leaflets organized into three different layers through the leaflet thickness, whose combined behavior is responsible for the peculiar characteristics of the entire leaflet: very low flexional rigidity, to guarantee a fast opening in systole, and a very high tensile strength, which allows for bearing the important high pressure differences in diastole.

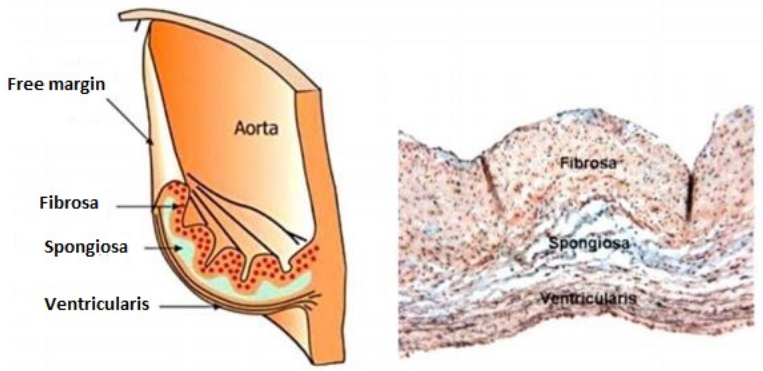

Figure 20: *Left hand panel*: sketch of an aortic leaflet depicting the three laminae. *Right hand panel*: histological section of the three laminae in the aortic leaflet

The three layers show very different properties and are called laminae (Figure 20):

- *lamina fibrosa*: it is the thickest layer (about 40% of the total leaflet thickness) [48] and covers the entire aortic surface of the leaflet. In this lamina, type I collagen fibers are orientated circumferentially (from commissure to commissure); these are folded in systole, when the tissue undergoes flexion, and stretched in diastole, when the tissue undergoes traction due to the trans-valvular pressure difference.

- *lamina ventricularis*: it is the layer exposed to the ventricle and it account for about 30% of the leaflet thickness [48]. It contains a dense net of collagen and elastin [42], where the radially oriented elastin fibers help reducing the radial deformation during the systole, facilitating the transvalvular blood flow.

- *lamina spongiosa*: it is the middle layer and account for about 30% of the total leaflet thickness. It contains many hydrated GAGs and PGs, which serve as lubricant during the relative motion of the other two layers.

The above described microstructure gives to the aortic leaflets a particular mechanical response with five main characteristics: non homogenous, elastic (layer structure), anisotropic (preferential directions of the collagen fibers), non-linear (collagen fiber progressive recruitment), and isochoric (water and GAGs presence). Many authors studied the mechanical response of aortic leaflets' tissue using biaxial tests [43][29][3]. The first constitutive model of aortic valve leaflets' tissue was formulated by Billiar

and Sacks based on load-controlled biaxial tests on human specimens [4]. The results yielded by those tests in terms of membrane tension vs. real strains in the radial and circumferential directions highlighted marked anisotropy of the tissue. In particular, the mechanical response in the circumferential directions is much stiffer than the response in the radial one (Figure 21). Indeed, the peak strain differs by more than 30% between the two directions.

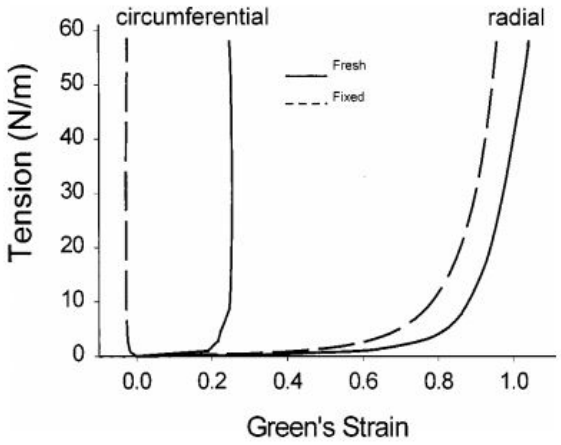

Figure 21: Representative circumferential and radial stress-strain curves from a fresh and a glutaraldehyde-fixed AV cusp, which show the pronounced mechanical anisotropy of both tissues [3].

3.4.3 Aortic root wall structure

The Valsalva sinuses have an inner structure similar to the one characterizing the aortic wall, as they are made by three layers. The innermost one, i.e. the *intima*, is rich in endothelial cells in contact with blood. The middle one, i.e. the *media*, is full of smooth muscle cells, PGs, elastin and type II and III collagen fibers preferentially oriented in the circumferential direction. The outermost layer, i.e. the *adventitia*, is characterized by type I collagen fibers preferentially aligned to the axis of the vessel. The interleaflet triangles are mainly composed by a fibrous structure containing contractile and cytoskeleton proteins and smooth muscle cells [14]. In particular, the triangles close to the non-coronary leaflet are mostly made of fibrous tissue, whereas the triangle between the right and left leaflet is composed primarily of muscle tissue, the fibrous tissue being confined in the apex zone [38]. The annulus, containing the leaflet insertion, is a fibrous ring rich in collagen where sometimes it is possible to find elastin and demyelinated nervous terminals.

4 State of Art

4.1 Introduction

The high prevalence of cardiac diseases and to the corresponding social and economical burden has been motivating great efforts in the study of the pathophysiology of the heart and in the development of innovative clinical solutions to cardiac diseases. In particular, a massive research activity has been focusing on the aortic root (AR), either to undestand the mechanicsms underlying pathological processes (e.g. calcification of aortic valve leaflets leading to aortic stenosis, and AR aneurysm leading to aortic dissection) or to analyze the effects of surgical and interventional procedures (e.g. valve sparing techniques, and trans-catheter aortic valve implantation).

In this context, the contionuous increase in computational power of microprocessors and in availability of parallel or distributed computing systems has boosted the exploitation of numerical simulations to aid reasearch on the AR. The latest developments in this specific type of activity merge image processing techniques and finite element or finite volume methods to quantify the structural response and the fluid dynamics, respectively, of the AR on a patient-specific basis.

In this chapter we will focus in particular on the different approaches available in the scientific literature for the analysis of AR structural mechanics. Such analysis involves five main steps: the definition of AR geometry, the consistency between AR geometry and loading conditions, the discretization of the reconstructed domain, the modeling of the mechanical response of the AR tissues, and the setting of proper boundary conditions to mimic kinemeatic constraints and mechanical loading due to blood pressure. Each of these steps will be discussed in the following sections.

4.2 Definition of AR geometry

The quantitative reconstruction of AR geometry is the first step towards the implementation of a structural model. In terms of geometrical realism, three generations of models can be identified in the literature. The most seminal models relied on a very simple and idealized geometry, and were based on the assumption of i) identical

sinus-leaflet unit, ii) plane-symmetry of each unit, and iii) straight longitudinal axis of the AR bulb and of the proximal ascending aorta. This approach is well exemplified by the work of Gyaneshwar [15] where the geometry was created using the procedure illustrated by Thubrikar in his work on the aortic valve [46]. In that work [46], he explored the design of trileaflet valves, such as the aortic valve, to ensure optimal dynamic performance during numerical simulations . More specifically he defined some geometric criteria to guarantee appropriate leaflet coaptation in the closed valve configuration, a proper valve height-to-diameter ratio to minimize dead space, no folds in the leaflets and minimum leaflet flexion to make the use of energy as efficient as possible. An accurate surface model of the valve meeting Thubrikar's parameters was constructed using a computer aided design software SDRC/IDEAS© (EDS, Plano, Texas, USA), where also the thickness variation of the leaflets was incorporated. In Figure 22.a the final model is shown with substantial details of geometry reported in Table 5. The main limitation of this is that, even though it provides extremely valuable insight, the physiological variability in valve design was not properly elucidated and described and, as a result, this approach seems to be somehow too rigid to accommodate the dimensional variability observed in normally functioning valves.

The second generation of models still made use of idealized geometrical paradigms, but removed the aforementioned assumptions and used measurements from *in vivo* images to set the dimensions of AR substructures. For instance, in the the work published by Conti et al. [12] the 3D geometry was based on a paradigm that accounted for the *in vivo* geometrical asymmetry of the leaflet-sinus units, as well as for the curved and tilted profile of the centerline of the lumen of the AR. The dimensions of the different parts of the model were based on measurements performed on cardiac magnetic resonance imaging (cMRI) performed on 10 healthy subjects, which were averaged over the 10 subjects to derive a representative model of the healthy AR. In the end-diastolic frame, the AR main geometric parameters were measured: annulus diameter, commissural positions, width of the Valsalva sinuses, and ascending aorta orientation. Each measurement was then averaged from three offline estimations by two blinded experienced operators (Table 6). Once acquired by cMRI, data were scaled so to be consistent with a 24 mm annular diameter, which is an average valve size [22], and then

were used to define each unit of the entire AR structure. To account for variations in aortic cusp thickness, different values were assigned to the thickness of the leaflets in four different regions: free margin, attachment edge, coaptation area, and belly [16] (Table 7). Furthermore, non-coronary leaflet regions were assumed to be thicker than the corresponding right and left regions [16][31]. Thickness values were assumed to be constant only for the aortic duct (2.3 mm), Valsalva sinuses (1.6 mm) and interleaflet triangles (2.3 mm) according to data reported in literature [16]. Of note, tissue thickness had to be defined based on data from the literature, because cMRI images did not yield any valuable information of this aspect. The final result is shown in Figure 22.b. The cMRI-derived morphological parameters used to define the 3D AR geometrical model appeared to be reliable, given the high intra and inter-operator repeatability of measurements, as well as the consistency with previous findings from the literature. However, the geometrical model was based only on measurements from 10 subjects: even though each measurement was averaged from three offline estimations by two blinded operators, and parameters' mean values were used, more subjects should have been recruited in order to reduce random errors, limit uncertainties due to individual differences and obtain statistically sound data. Moreover, the usage of cMRI do not give the possibility to assess tissues thickness values, which were then obtained from the literature; this may be a source of uncertainty, especially with respect to leaflet stresses: leaflets indeed mainly undergo bending, and so the stresses acting on them depend on the third power of the thickness. Despite the limitations described above, the computed results confirmed that morphological differences between leaflet-sinus units induce important differences in stress values; thus, discarding a symmetrical design to adopt an asymmetrical one can provide more accurate stress-strain patterns.

The third and current generation of geometrical models is based on the complete 3D reconstruction of patient-specific anatomies through the segmentation of clinical images. An example of such state of the art is the patient-specific AR model reconstructued from real-time 3D ultrasound images presented in the work of Chandran et al. [10]. Their aim was to create a computational tool to build AR models with tricuspid and bicuspid valve (TAV and BAV, respectively). The model was created starting from real-time 3D echocardiography (rt3DE) in the Gorman Laboratories at the University

of Pennsylvania, which allowed for the reconstruction of the AR and aortic valve in a fully closed position as shown in Figure 22.c. This model provided a patient-specific geometry reconstruction that took into account the asymmetry of the AR structure. However, this work remarked an important limitation related to the usage of ultrasound images: even though it was possible to obtain the detailed 3D geometry of the valvular apparatus, ultrasound imaging lacked sufficient resolution to provide accurate information on the thickness of the leaflets or of the AR and so, as a common practice, it had to be assumed constant and the effect of variation of the thickness on the deformation and stress distribution on the structures of interest were essentially neglected. Another representative work on patient-specific AR modeling is the one by Labrosse et al.[24]. Here, a complex process for the AR geometry recostruction, including the leaflets, was performed using an integrated framework which extracted geometrical informations about AR from subject-specific 3D+t TEE images (3D ultrasound images). In particular, the dedicated software acquired the 3D coordinates of 21 anatomical landmarks of the AV apparatus in a total of ten indivuals. The number of landmarks was chosen to be as low as possible to be at the same time practical but still sufficient for an accurate representation of individual AV anatomies. The landmarks were manually extracted from the images using an automated graphical-user interface dubbed AVQ, which was specially designed for this purpose in Matlab© (The MathWorks, Natick, MA, USA).The reconstruction process produced a structure with three finite elements through the aortic thickness and two across the leaflets thickness. For the sake of simplicity, the thickness was assumed identical both for the three leaflets and for the aortic wall, and constant across each region. Age-matched thickness values were defined for the leaflets, based on the linear interpolation of data from human aortic leaflets of subjects with age ranging from 15 to 85 years [28]. The final results is shown in Figure 22.d. This model started from robust patient-specific datasets where: first a dedicated software was created to acquire the 3-D coordinates of the anatomical landmarks, and than further measurements from ten 3D+t TEE datasets of normal AVs were assessed for inter- and intra-observer variability. All these tests demonstrated mean measurement errors well within the acceptable range assuring high feasibility of the geometrical information aquired. The main limitation of this work with respect to

anatomical realism is related to the reconstruction process. An aggressive smoothing of morphological data was performed, and these were used to morph an ideal geometry. The final result hence was rather distant from the actual AR morphology.

	Values
Radius of commissures R_c	12.0 mm
Radius of bases	12.0 mm
Height of valve	17.0 mm
Angle of free edge to plane passing through commissures	32°
Angle of undersurface of the leaflets to plane passing through the thress commissures	22°
Coaptation height at center	4.84 mm
Commissural height	8.52 mm
Lenght of leaflet free edge	29.75 mm
Length of leaflet in radial direction	16.8 mm
Sinus depth	17.52 mm
Sinus height	21.12 mm

Table 5: Gyaneshwar's model: dimensions of AR used in the study.

	RC	LC	NC
Intercommissural distance L [mm]	24.2 ± 4.0	21.1 ± 3.0	22.0 ± 3.6
Annular diameter D_a [mm]	23.9 ± 3.8	25.6 ± 4.7	25.6 ± 3.2
Intermediate width D_I [mm]	31.1 ± 4.2	31.9 ± 5.0	32.7 ± 6.2
Intermediate height h_I [mm]	6.1 ± 1.5	6.2 ± 1.1	6.6 ± 1.5
Maximum width D_m [mm]	32.1 ± 6.0	32.4 ± 5.4	35.1 ± 4.0
Height of maximum width h_m [mm]	10.8 ± 2.6	11.4 ± 2.5	11.9 ± 2.8
STJ diameter D_{STJ} [mm]	27.1 ± 6.6	25.9 ± 5.8	29.9 ± 4.1
Height of the sinuses H_{STJ} [mm]	21.9 ± 3.9	21.2 ± 4.2	22.0 ± 3.4

Table 6: Conti's model: MRI measurements (average ± standard deviation) of the aortic root in the end diastolic frame. LC = left-coronary. RC = right-coronary. NC = non-coronary.

	LC & RC	NC
Attachment edge [mm]	1.60	1.55
Free margin [mm]	1.53	1.96
Coaptation area [mm]	$0.68 - 1.29$	$0.68 - 1.65$
Belly region [mm]	$0.18 - 0.58$	$0.18 - 0.58$

Table 7: Conti's model: different values were assigned to the thickness of the shell elements in different regions of the leaflet. LC = left-coronary. RC = right-coronary. NC = non-coronary.

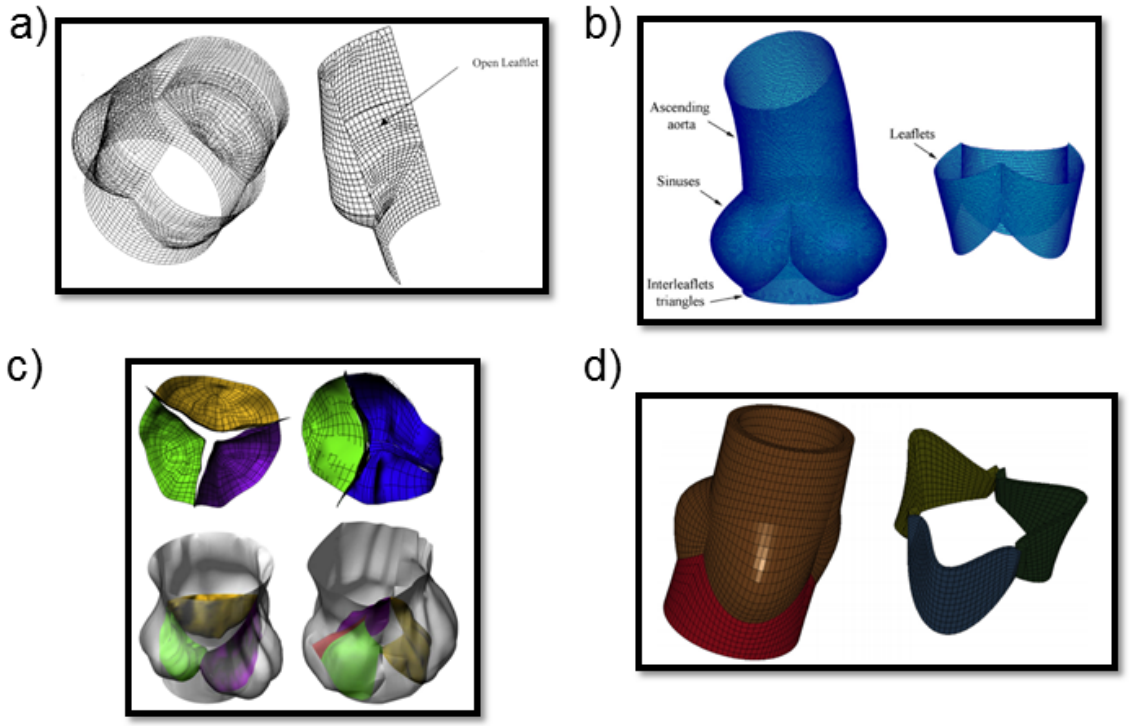

Figure 22: Geometry comparison between the model described above. a) Gyaneshwar's model: *left hand panel*, finite element model of the aortic valve with sinuses; *right hand panel*, cut section of the finite element model showing the leaflet in open position. b) Conti's model: *left hand panel*, three-dimensional FE model of the physiological aortic root; *right hand panel*, detail of the aortic leaflets. c) Chandran's model: *left hand panel*, reconstructed TAV employed in the finite element analysis, leaflets in the *upper side* and sinuses in the *bottomer side*; *right hand panel*, reconstructed BAV employed in the finite element analysis, leaflets in the *upper side* and sinuses in the *bottomer side* d) Labrosse's model: *left hand panel*, unpressurized aortic root model; *right hand panel*, view of the leaflets inside the model.

4.3 Consistency between AR geometry and loading conditions

While the aortic valve can be assumed approxinately unloaded at two time-points through the cardiac cycle, when the ventricular and aortic pressures match each other, the aortic wall, including the Valsalva sinuses, undergoes non-negligible pressure loads throughout the whole cardiac cycle. As a consequence, no matter what time-point is selected to reconstruct the AR geometry from medical images, the obtained geometry cannot be treated as a stress-free configuration. Thus, the correct stress pattern actually characterized the reconstructed geometry should be identified. In this section, two approaches to this problem are presented. The first one was in the work by Conti et al. [12] and in the study by Labrosse and colleagues [24]. Anatomical data were obtained from medical images at end-diastole, when ventricular and aortic pressures were assumed equal to 80 mmHg and the aortic valve was assumed unloaded. In order to obtain consistency between the AR 3D geometry and the pressure loads, a two step-procedure was adopted in these studies (Figure 23). First, the root dilation associated with end-diastolic pressures was estimated using equations describing the response of an elastic, thick-walled cylinder [5]. On the basis of this estimation, the initial dimensions of the model were set. Then, this first guess of the geometry was refined through a set of preliminary simulations. In each simulation, the 80 mmHg end-diastolic aortic and ventricular pressures were applied to the proper regions of the undeformed model. Deformed root dimensions and nodal circumferential displacements were extracted: if the deformed dimensions were not consistent with end-diastolic MRI measurements, the unloaded root geometry was redefined exploiting the calculated displacements. These preliminary simulations were then iterated until the model's end-diastolic dimensions differed from the corresponding MRI data less than 2%. Of note, the result of this procedure resulted in an end-diastolic geometry that was consistent with the measured geometrical parameters, but did not necessarily match the detailed geometry as reconstructed from medical images.

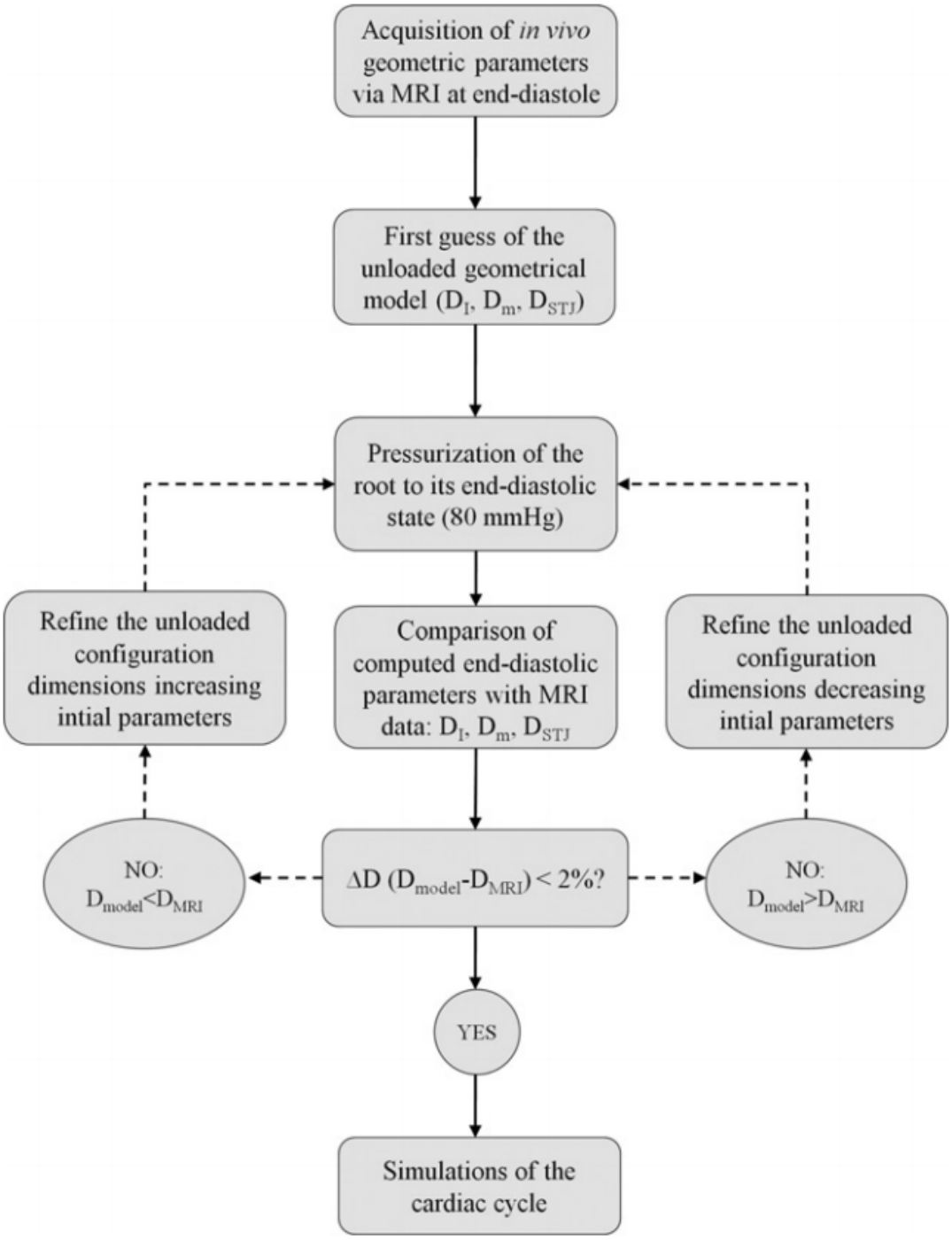

Figure 23: Flowchart of the method #1 to define the initial geometry of the aortic root, as proposed in the work of Conti et al [12]. The estimated unloaded dimensions of the Valsalva sinuses and of the ascending aorta (intermediate width D_I, maximum width D_m, STJ diameter D_{STJ}) were refined by means of an iterative process, until model's end-diastolic dimensions (D_{model}) differed from the corresponding MRI data (D_{MRI}) by less than 2%

The second method was developed in a recent Master thesis [44] and is currently part of a manuscript under review [35], and it is aimed at obtaining consistency be-

tween the loaded geometry and the geometry reconstructed from medical images in a pointwise fashion. To this aim, the pre-stress field characterizing the latter was computed and assigned to the geometrical model. In detail, the configuration of the aortic root reconstructed from cMRI (Ω_{img}) was used as starting configuration for the computation of the pre-stresses that, together with the intraluminal pressure, should give an equilibrium state for this configuration. Ω_{img} was loaded with an 82 mmHg intraluminal pressure, while the two ends of the aortic wall were constrained with respect to longitudinal and circumferential translations, based on two local cylindrical reference frames. The simulation was then iterated as following: in the inflated configuration (Ω_{82}) the computed nodal displacement field (u_{82}) was checked for the entire aortic wall; if the peak value of displacement magnitude did not exceed the in-plane resolution of cMRI, i.e. 1.10 mm in this study, configuration Ω_{82} was considered equivalent to Ω_{cMRI}, and the corresponding Cauchy true stress field (Ω_{82}) characterizing the aortic wall was considered the pre-stresses field σ_{pre} to be applied when simulating AR biomechanics throughout the cardiac cycle. Otherwise, σ_0 was updated and set equal to σ_{82}, and the pressurization simulation was performed again. At the end of the iteration process, the stress field σ_{82} was exported into a text file and used as pre-stress field in the subsequent simulation of AR biomechanics throughout the cardiac cycle. A flowchart of the entire process is shown in Figure 24.

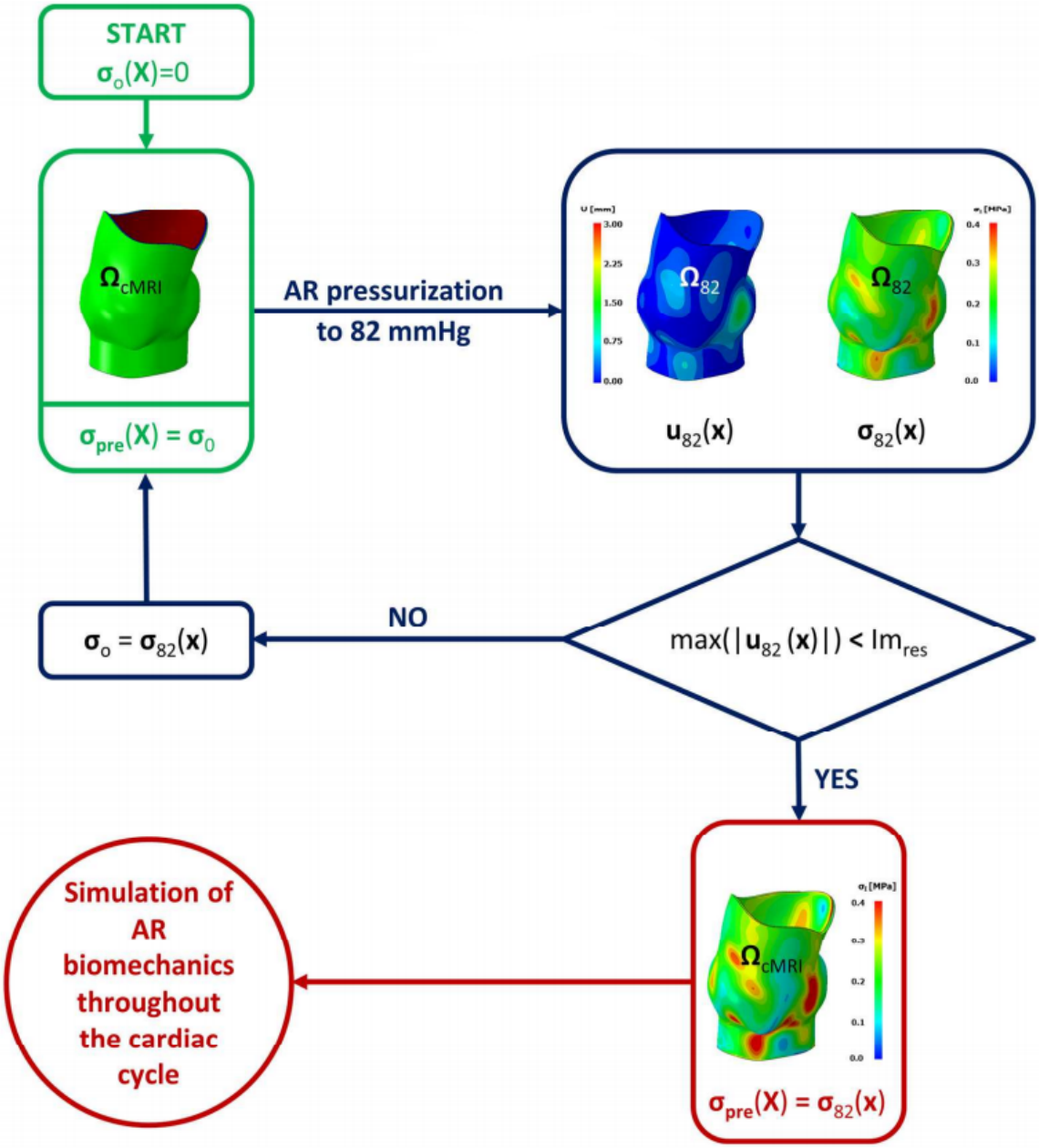

Figure 24: Flowchart of the method #2 to define the pre-stress computation. AR geometry reconstructed from cMRI (Ω_{cMRI}) is initially characterized by zero prestresses ($\sigma_{pre} = \sigma_0 = 0$). The AR model is pressurized up to 82 mmHg. From the pressurized configuration (Ω_{82}), aortic wall nodal displacements (u_{82}) and Cauch stresses (σ_{82}) are extracted; if the magnitude of the peak nodal displacement is lower than the in-plane resolution of medical images (Im_{res}), the final pre-stress field is set equal to σ_{82}, otherwise the initial stresses are set to σ_{82} and the inflation simulation is iterated. X and x indicate the initial and current configuration of the model, respectively.

The primary difference between these two approaches regards the preservation of the initial geometry configuration. While the first approach modifies, simulation after simulation, the initial dimensions of the model, the second one preserves the initial

structure manipulating the pre-stress state to be applied as intial condition in the subsequent simulations. The latter is more suitable with patient-specific models in which the initial AR dimensions do not have to be modified, due to the fact that they are directly obtained from *in vivo* MRI images. For this reason, the second method was adopted in this work, as explained in detail in the next chapter.

4.4 Discretization of the domain

The discretization of the domain is another important aspect of the modeling procedure. The element type and its characteristic dimension, i.e. the mesh size, are crucial aspects which entail the consistency and the reability of the results obtained from the simulations. Here, a brief introduction to different features about the discretization of the domain is presented.

Mesh size: the increasing of the mesh size is always related to a decreasing in computational costs, and this is an important aspect regarding the applicability of simulations. However, it may produce results with bad accuracy; hence, high mesh size produce big elements which generally are not able to correctly fit the represented geometry and also are not able to estimate the real variables pattern resulting in loss of essential informations. To the best of our knowledge, in the field of domain discretization of the AR geometry (including leaflet discretization), the vast majority of the published studies does not assume an element characteristic dimension higher than 1.0 mm.

Element type: working on highly curved geometries, as the physiological anatomies of AR sinuses and AV cusps, generally makes it non-trivial to achieve a satisfactory mesh quality, i.e. to avoid excessive ly distorted elements that would be prone to generate artifacts in the subsequent simulations. This aspect contributes to driving the choice of the elements used in the discretization of the geometry, which may be linear or of higher order. Also, aortic valve leaflets and aortic wall may be discretized using solid, topologically 3D elements or shell elements, which are topologically 2D and assumed a plane stress state. In this context, the choice between shell elements and solid elements presents pros and cons on both sides. Shell elements are well suited to repro-

duce curved geometries avoiding excessive distortions or negative volumes, especially when the model has to reproduce very irregular profiles. Thanks to their formulation, shell element are able to reduce the computational cost up to 3.5 times with respect to a solid mesh with an equivalent mesh size. At the same time, though, shell elements can have an excessive bending stiffness [32]. Also, due to the plane stress hypothesis, in general they are not well suited to quantify the variations of field variables through the thickness of the elements. Another problem occurs when using shell mesh to discretize aortic valve leaflets: at the leaflet-aortic wall interface, shell elements are connected to the aortic wall through two nodes laying on a line. If the latter is not markedly curved, undesired rotations of the leaflet shell elements may occur along the insertion line. As a result, when simulating the closure of the aortic valve an excessively prolapsing configuration of the leaflet may be computed even if these coapt properly.

Conversely, the use of solid elements allows for defining multiple layers within the thickness of the aortic wall and of the leaflets [22], as well as to better capture the variations in field variables through the thickness. Moreover, having multiple nodes through the leaflet thickness at the interface between the latter and the aortic wall should prevent from unrealistic rlocalrotations of the leaflet. However, the use of solid elements can make the generation of the computational grid more complicate.

Finally, it is possible use either full-integration elements or reduced-integration elements. Using elements with reduced integration implies a lower-order integration to form the element stiffness; this implies on the one hand a reduced computation time, especially in three dimensions, but on the other hand a potentially less accurate computation of the field variables [1]. Some studies, as the work by Soncini [32] and the one by Conti [12], chose to neglect this problem for the leaflets discretization, in favor of a reduced computational cost.

In Table 8 are shown different approaches for the discretization of the domain.

	AR wall discretization	**AV leaflet discretization**
Soncini et al. [32]	4-node SHELL el., R	4-node SHELL el., R
Labrosse et al. [22]	8-node SOLID el., F	8-node SOLID el., F
Conti et al. [12]	3-node SHELL el., R	3-node SHELL el., R
Chandran et al. [10]	4-node SHELL el., F	4-node SHELL el., F
Grande et al. [16]	6-node SHELL el., F	6-node SHELL el., F

Table 8: Summarizing of the different discretizations of the domain. R = reduced-integration elements. F = full-integration elements.

4.5 Modeling of the mechanical response of the AR tissues

The main issues regarding the modeling of the material properties of AR tissues is that, even though the patient-specific geometry of the AR can be obtained with reasonable accuracy from clinical images (e.g. cMRI) as previuosly discussed, it is not feasible to account for patient-specific mechanical properties. It is well known that physiological aortic root tissues exhibit, both for AV cusps and aortic wall, a multi-axial non-linear stress-strain relationship [47]; experimental studies have demonstrated in particular that leaflets are stiffer along the circumferential direction compared to the radial direction.

As a first approach, some FE studies assumed, for simplicity, a linear isotropic elastic material specification for the valvular structures (both leaflets and wall), generally with an elastic modulus of 2 MPa and a Poisson's ratio of 0.3, as in the study of Gyanashwar et al. [15]. This kind of formulation reduces the computational costs, but introduces a strong semplification that may be a source of inaccuracy, especially with respect to leaflet stress-strain state computation.

More recently, some other studies incorporated a Fung-type constitutive model based on biaxial experimental data. This represent a strain-based approach to describe the hyperelastic behavior of the material; some fundamental equations regarding the hyperelasticity theory are reported in Appendix B. The general equation of a Fung-type

strain energy function is the following:

$$U = \frac{C}{2}(e^{Q} - 1) \tag{5}$$

where U is the strain energy function characterizing the hyperlestatic response of the material and C the stiffness parameter; Q is a function of strain composed of the Green-Lagrange strain tensor E and material anisotropy tensor D:

$$Q = E \cdot DE \tag{6}$$

For example, Jermihov [19] and Chandran [10] used in their study this kind of formulation for the leaflets; however, they still adopted an isotropic, linear, elastic material for the root and the sinuses tissues, with an elastic modulus of 2 MPa and a Poisson's ratio of 0.3.

Another complex material specification was presented in the work of Conti [12]. Here, the mechanical response of aortic leaflets was modelled by a transversely isotropic and incompressible hyperelastic model, implemented by ABAQUS/Explicit© code in a VUMAT subroutine, based on an invariant-based strain energy function with the following form:

$$W = c_0 \exp(c_1(I_1 - 3)^2 + c_2(I_4 - 1)^2) - 1 \tag{7}$$

where $I_1 = tr(\boldsymbol{C})$ is the first invariant, $I_4 = \lambda^2$ is the fourth invariant, $\boldsymbol{C}$ is the right Cauchy-Green tensor, λ is the stretch of the fibres and c_0, c_1 and c_2 are constitutive parameters. Also in this work, the mechanical response of the other tissues was still assumed to be linear, elastic and isotropic with elastic modulus of 2 MPa and a Poisson's ratio of 0.45.

Both the last two kind of material formulations are well suited to reproduce the complex aortic cusp tissue, taking into account the anisotropy and the hyperelasticity, which are key points characterizing this type of tissue. The choice of a complex formulation only for the leaflets is related to the fact that, using a complex and more precise material definition for all AR structures, causes an huge increasing in computational costs. Within this context, it is preferable a more accurate material definition for the leaflets instead of the wall, because they are the most relevant structures inside the aortic root, especially when valve dynamic have to be investigated. In addition to this,

to the best of our knowledge, fitting the AR wall properties with a linear, isotropic formulation provides a simplification that may be neglected wihtout making high errors [18].

Another work exploiting a strain-based energy function to define the aortic root tissue behavior is the one by Labrosse [24]. The energy function used is of the following type:

$$U = \frac{c_1}{2}(\exp(c_2 {E_\theta}^2 + c_3({E_z}^2 + {E_r}^2)) - 1) \tag{8}$$

where E_θ, E_z and E_r are the componentes of the Cauchy-Green strain tensor in the circumferential, longitudinal and radial direction, respectively, and c_1, c_2 and c_3 are material constants. Moreover, in order to reproduce more precise behavior of the aortic root tissues, age-matched material properties were implemented both for the aortic wall and the cusps. To this aim, for the aortic wall tissue, they used the circumferential and longitudinal stretch ratios in 14 excised pressurized human ascending aortas under closed ends and free extension conditions to determine the average circumferential and longitudinal stretch ratios for pressures between 0 and 160 mmHg in two average groups, one at age 54, and one at age 72. Then, based on evidence of linear variation of these stretches with age, they linearly interpolated the circumferential and longitudinal stretch ratios at any given age based on those at 54 and 72. Combining these data with an average measured unpressurized human ascending aortic wall thickness of 1.86 mm [23], they calculated the parameters of an hyperelastic, transversely isotropic material, representing the age-matched human ascending aorta; more specifically, they used the Guccione's material formulation [17]. For the aortic leaflets, they relied on the planar equibiaxial data published in Martin and Sun's work [45] from porcine aortic valves (age $6 - 9$ months) and human aortic valves (average age of 80.6 years). The strains were measured under controlled membrane tensions; data were digitized from the published document and averaged for the three leaflets. In this case, they considered that the data obtained from pigs were valid to describe aortic leaflets in 18-year old humans, as suggested in Martin and Sun [45]. For lack of more detailed data, and as in Weinberg et al. [37] where observations reported in Christie and Barratt-Boyce [6] were simplified, they assumed a linear variation of circumferential and radial stretch ratios with age. Therefore, they linearly interpolated the circumferential and radial strains under set

membrane stresses at any given age based on those at 18 and 80.6 years.

4.6 Boundary conditions

The choice of the boundary conditions is a key points in AR finite elemens models analysis. Different approaches can be found in scientific literature regarding the constrains to be applied to the AR components; a brief summary of the most intresting boundary conditions used for AR numerical simulations is reported below
. In the work of Soncini et al. [32], during the entire duration of the simulated phenomenon, nodes belonging to the annulus were fully constrained and the edge at the top of the ascending aorta was constrained with respect to the circumferential and longitudinal translations; in addition, multi-point constraints were used to limit mesh distortion near the leaflet free margin. A similar approach to the distal and proximal nodes constrains can be found in the work of Chandran [10]; here, however, the base of the annulus and the top of the STJ were fixed from motion along the axis (longitudinal direction), and were not fully constrained as seen before. A completely different approach was use instead in the work of Conti et al. [12], where any node was constrained, but the changes in dimensions of the valve annulus over the cardiac cycle were accounted for by imposing proper nodal displacements on the nodes belonging to the annulus consistently with data reported by Lansac et al. [25].
Concerning the pressure loads imposed during cardiac cycle simulations, a common approach is used in all the most important work in literature. A physiological, time-dependent aortic pressure is applied to the aortic inner wall, ventricular pressure to the interleaflet triangles inner wall and a consistent trans-aortic pressure drop to the leaflet surfaces, as in Figure 25 from the work of Conti et al.[12].

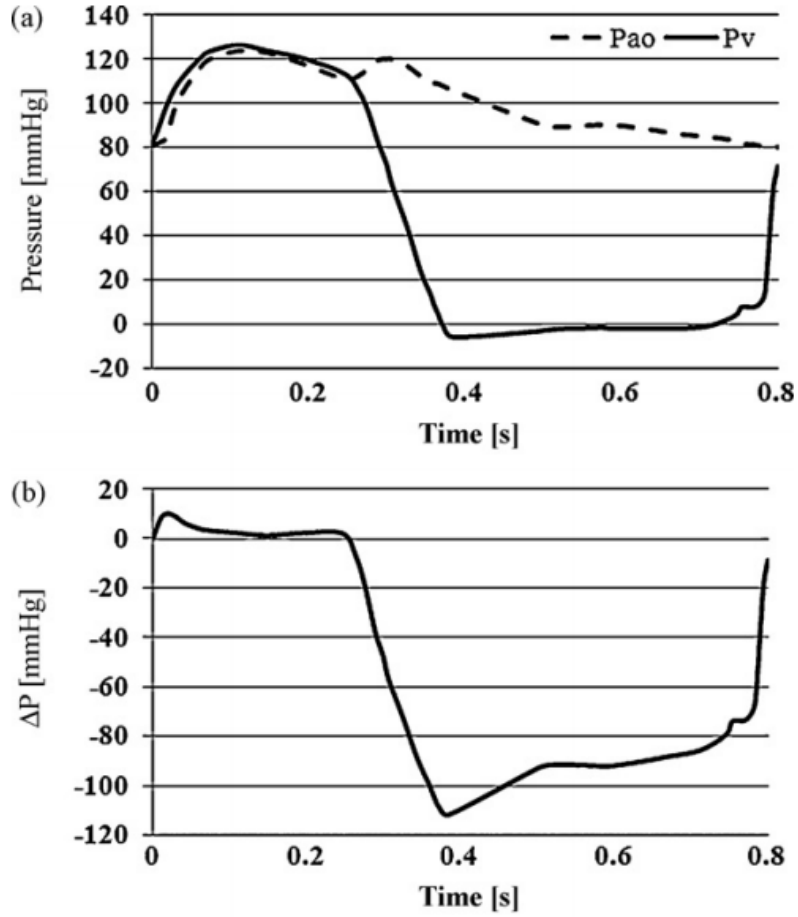

Figure 25: Time-varying pressure change for the complete cardiac cycle. a) Left ventricular (Pv) and aortic pressure (Pao) pulses. b) Transvalvular pressure difference (ΔP) between left ventricle and aorta.

4.7 Conclusion

The topics presented in this chapter highlight the main issues to be accounted in AR modeling, with special emphasis on the aspects related to the geometry reconstruction, the consistency between AR geometry and loading conditions, the discretization of the reconstructed domain, the modeling of the mechanical response of the AR tissues, and the setting of proper boundary conditions to mimic kinemeatic constraints and mechanical loading due to blood pressure. Within this context, the aim of this thesis is primarily to provide a full 3D patient-specific AR model, starting from MRI clinical images which allows for the finite element simulation of AR biomechanics and allows for consistency between AR geometry and the pressure loads acting on it by computing the corresponding pre-stresses and imposing these on the reconstructed geometry.

5 Materials and Methods

5.1 Introduction

As discussed in the previous chapter, five main aspects need to be accounted for when implementing a finite element model of the AR: geometry reconstruction, discretization of the domain, identification of the stress field consistent with the reconstructed geometry and with the pressure loading it, modeling of tissue mechanical properties, and definition of proper boundary conditions. In this regard, the present work advances the modeling approach proposed in a recent Masters thesis [44] developed at the Computational Biomechanics Laboratory of the Department of Electronics, Information and Bionengineering of Politecnico di Milano. The latter reconstructed the AR geometry from cMRI, made use of a single layer of shell elements to discretize the geometry of aortic valve leaflets, and computed the pre-stress field associated to the loads acting on the reconstructed geometry through a single step procedure.

The principal aim and novelty of the present work is the design, implementation, and testing of a semi-automated algorithm to generate patient-specific image-based aortic root finite element models completely discretized with hexahedral elements, including the possibility to set the space-dependent patterns of leaflets thickness. Such algorithm had to be integrated in a automated pipeline allowing for the computation of the AV pre-stresses and for the subsequent simulation of AR structural response throughout the cardiac cycle.

In order to test the impact of this novel approach, this method was applied to a small cohort of subjects and its results were compared to the ones yielded by models discretized using AV leaflets either with shell elements or uniformely thick solid elements. The whole modelling process was handled by a Matlab© script that automatized the working pipeline going from segmented images to the setting of the finite element simulations to be run in the commercial explicit finite element solver ABAQUS/Explicit© (Simulia, Dessault Systemes). The entire pipeline consisted of five steps (Figure 26): i) acquisition of cine-cMRI data and segmentation of the AR structures in the end-diastolic frame; ii) reconstruction and discretization of AR 3D geometry; iii) definition of tissues mechanical properties; iv) generation of the input files for the finite element

computation of the pre-stress field acting on the AR in the reconstructed geometrical configuration; v) generation of the input files for the finite element computation of AR biomechanics throughout a cardiac cycle simulation.
Each of these steps will be discussed in a section within this chapter.

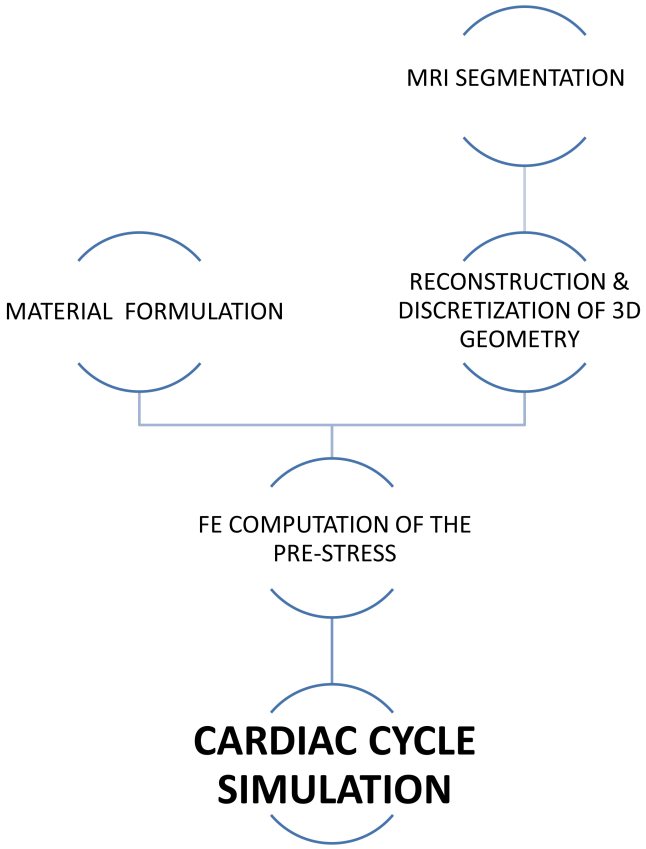

Figure 26: Our schematic modeling approach.

With this new armamentarium, we tested three working hypothesis, which were mainly related to the new approach to the discretization of the domain, mandatory step to reach our principal goal:

1. The use of solid elements in the discretization of leaflet geometry limits, or even prevents from, undesired and urealistic local rotations of the leaflets at the insertion onto the aortic wall, thus leading to a more realistic configuration of the aortic valve when simulating its closure.

2. The use of solid elements in the discretization of leaflet geometry allows for capturing variations in strains and stresses through the thickness of the leaflets, which cannot be captured when using shell elements.

3. When using solid elements, different regional distributions of leaflet thickness may lead to markedly different results in terms of leaflet strains and stresses when simulating AR function throughout the cardiac cycle.

In order to test these hypothesis, cMRI data of three healthy subjects were considered, and for eaxch subject three models were implemented through our Matlab© tool and used to compute AR biomechanics throughout the cardiac cycle:

- **SH** model ("shell model"), caharterized by an aortic wall discretized into 8-node solid elements with reduced integration (ABAQUS© C3D8R elements), and by leaflets discretized into 4-node shell elements (ABAQUS© S4 elements) assumed homogeneously thick.

- **3D-HT** model ("3D homogeneous thickness model"), in which leaflets discretization was modified: leaflets were discretized using three layers of 8-node solid elements (ABAQUS© C3D8 elements), and leaflet thickness was still assumed homogeneous. The comparison between the results yielded by 3D-HT models and the corresponding SH models allowed for testing the first two working hypothesis.

- **3D-MT** model ("3D modulated thickness model"), which differed by the 3D-HT model because leaflet thickness was modulated to match region-specific thickness values. The comparison between the results yielded by 3D-MT models and the corresponding 3D-HT models allowed for testing the third working hypothesis.

5.2 Acquisition of cMRI data and segmentation of AR structures

Our modelling approach was applied to cMRI datasets of three healthy volunteers with an average age of 28 years (Table 9).

	AR1	AR2	AR3
Gender [M/F]	M	M	M
Age [years]	28	31	27
Weight [Kg]	65	90	90

Table 9: Characteristic of the three volunteers enrolled in the study.

The acquisition and segmentation processes are described in detail in [44], however the main steps of these procedures are explained below.

T1-weighted cine-cMRI sequences were acquired on 18 planes evenly rotated (one every 10°) around the axis passing through the centre of the annulus and the centre of the sino-tubular junction (Figure 27.a). Acquisitions were performed on a 1.5 T Achieva scanner (Philips Healthcare Medical System, Irvine, Calif). In-plane spatial resolution and slice thickness were equal to 1.10 mm and 7 mm, respectively. 30 frames/cardiac cycle were acquired with R-wave triggering.

Images were manually processed in the first systolic frame, identified as the first frame characterized by an open aortic valve. As in previous studies [12][32][8][36], the transvalvular pressure acting on AV leaflets was considered negligible. In this configuration, processing was performed by in home Matlab© software, which allows for tracing AR substructures by simply clicking multiple points on the image. In each plane, two annular points, which lay on the annulus, the Valsalva sinuses, two STJ points, and the ascending aorta were defined. Leaflets were traced only if clearly visible (Figure 27.b). Finally, when all AR substructures were traced, 20 to 25 points were selected. Tracing was performed by two independent observers on each dataset, in order to asses the inter-observer variability of the procedure.

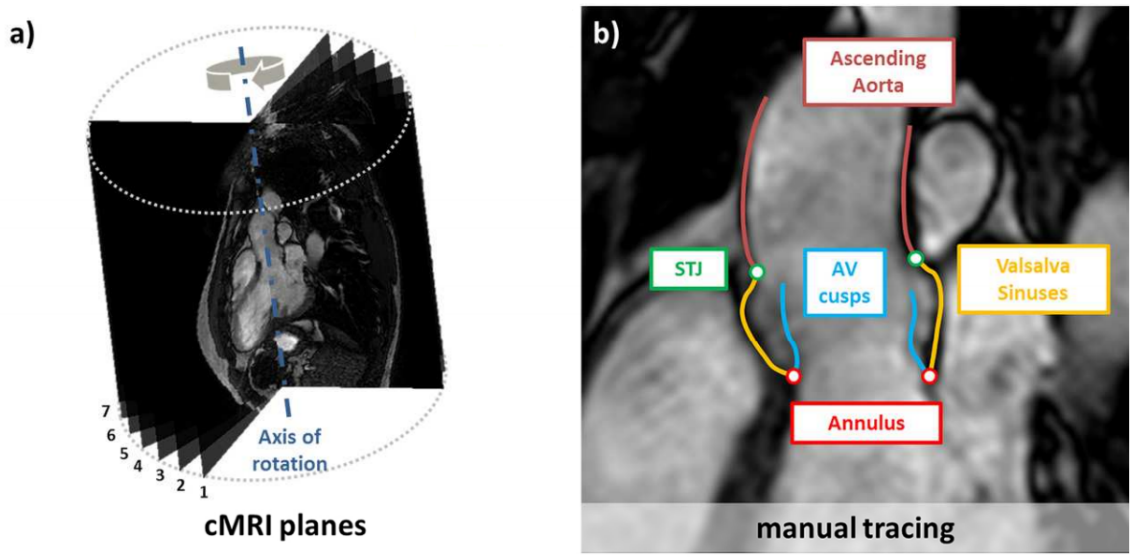

Figure 27: cMRI data acquisition and image processing: a) cMRI cine protocol of acquisition; b) manual tracing of AR sub-structures on a cMRI plane including two annular points, the Valsalva sinuses, two STJ points, the ascending aorta, and leaflets whenever clearly visible.

5.3 Reconstruction and discretization of AR 3D geometry

The 3D reconstruction of the anatomy of the sub-structures of the AR was carried out starting from the raw data points identified in the segmentation phase. The Matlab© script we implemented exploits the external CAD software Gambit© (Ansys, Fluent Inc., Canonsburg, PA, USA), which is run as a batch process. Data are exchanged between Matlab© and Gambit© through ASCII files, accordingly with the flowchart in Figure 28.

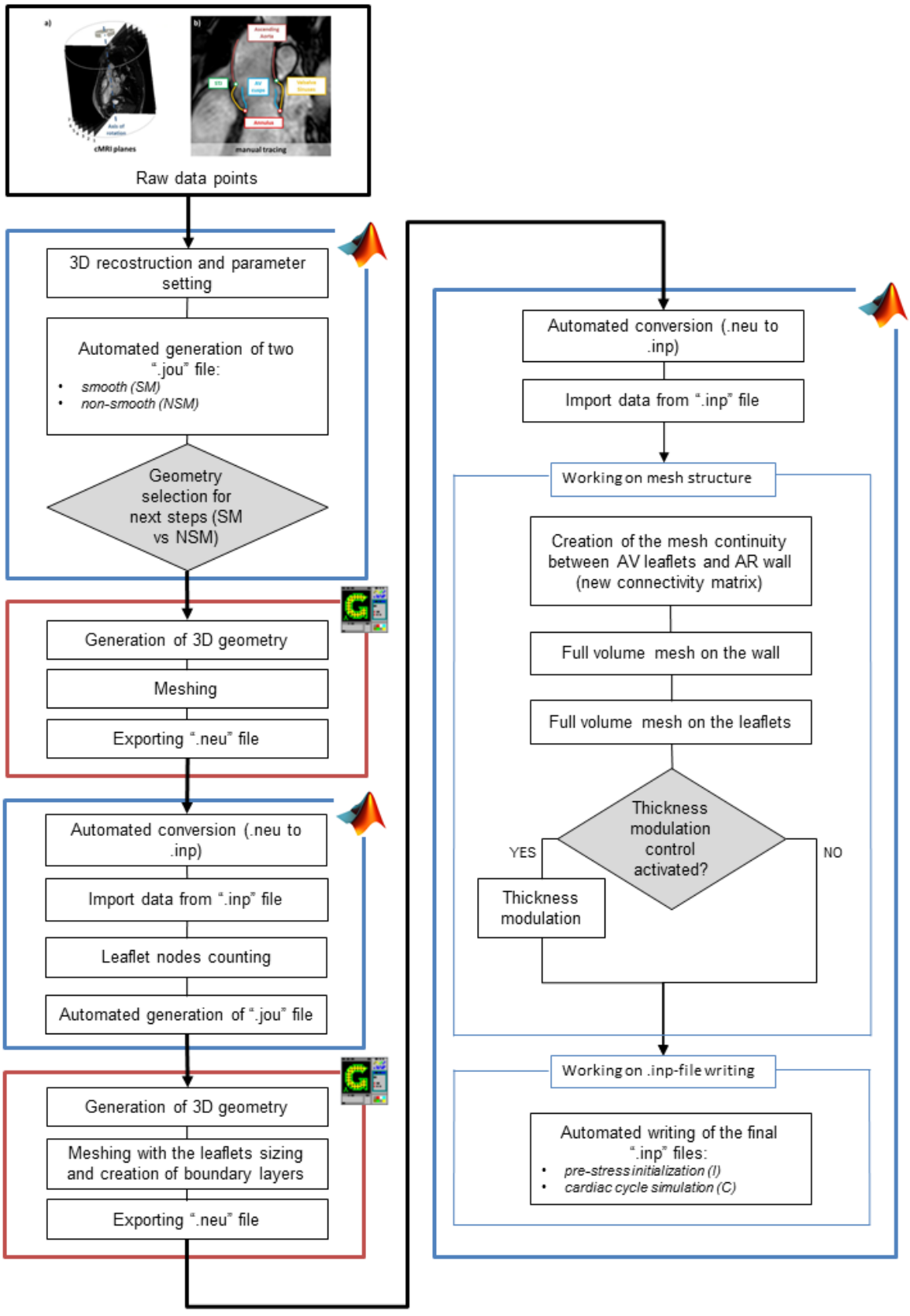

Figure 28: Schematic flow-chart of our automated script. *Blue* boxes involves Matlab© tools, whereas *Green* boxes involves Gambit© tools.

The automated procedure implemented by our tool is divided in five principal steps, each one with the input data coming from the outputs of the previous one. Three steps are handled by Matlab©, the remaining two steps are handled by Gambit©; a more detailed description of each step will follow in the next sections.

5.3.1 Processing of raw data points and 3D geometry reconstruction (MATLAB I)

The processing of the raw data points was done using a Matlab© script performing the operations described in the recent Master thesis work[44]. Points on the profiles of the ascending aorta and of the sinuses were assumed to lay on the inner surface of the aortic wall. In order to obtain the latter, traced points were interpolated by cubic splines, which were then re-sampled to obtain, over each substructure, a set of N points uniformly distributed along the longitudinal AR axis, independently of the specific number of points selected by the observer during the manual tracing of AR substructures (N=4 for each side of the ascending aorta, N=5 for each Valsalva sinus and N=5 for each leaflet). As a result, for each substructure N levels of points were obtained, the i-th level containing the i-th point of each profile of the sub-structure of interest. For the Valsalva sinuses and the ascending aorta in particular, since two profiles were traced on each image plane, each level clustered 36 points. These were filtered as following: the least square plane π_i and the centre of mass G_i of the 36 points of the i-th level were identified, and a local cylindrical reference frame (ρ, θ, z) was defined, the z-axis being normal to π_i and passing through G_i. In this reference frame, the axial and radial coordinates of the points were filtered through approximating 4^{th} order Fourier functions (Figure 29.a).

$$z(\theta) = a_0 + \sum_{i=1}^{4} [a_i \cos(i\theta) + b_i \sin(i\theta)] \tag{9}$$

$$\rho(\theta) = c_0 + \sum_{i=1}^{4} [c_i \cos(i\theta) + d_i \sin(i\theta)] \tag{10}$$

The approximating functions were sampled at the original values of angular coordinate θ to obtain the corresponding filtered cylindrical coordinates. On the 3^{rd} level of points generated for the Valsalva sinuses, i.e. for the level located halfway between the annulus

and the STJ, the filtered radial coordinates $\rho(\theta)$ of the points were used to identify the three sides of the ascending aorta that correspond to the Valsalva sinuses. In particular, the angular coordinates $(\theta_{C1}, \theta_{C2}, \theta_{C3})$ corresponding to boundaries of the three sinuses were identified. θ_{C1} was the value of θ associated to the minimum value of ρ; in two intervals of θ values centred at $\theta_{C1} + \frac{2\pi}{3}$ and $\theta_{C1} - \frac{2\pi}{3}$, respectively, θ_{C2} and θ_{C3} are the values corresponding to the respective local minima of ρ (Figure 29.b). Polar coordinates were transformed back into the global Cartesian reference frame and used to define vertexes. The vertexes laying on the annulus were copied and translated along the normal to their least square plane, towards the ventricular volume; ten copies were generated for each vertex, uniformly distributed over a distance by 10 mm. This region mimicked the presence of the basal-ring, which connects the AR annulus to the underlying myocardium and is not well visible from the images. As a results, three regions of the aortic wall were obtained, each one comprising one of the three sides of the ascending aorta, the corresponding Valsalva sinus and the corresponding side of the basal ring. The coordinates of the points obtained by leaflets tracing were filtered as for the points of the aortic wall; however, in this case 2^{nd} order Fourier functions were used, in order to cope with the noise affecting raw data.

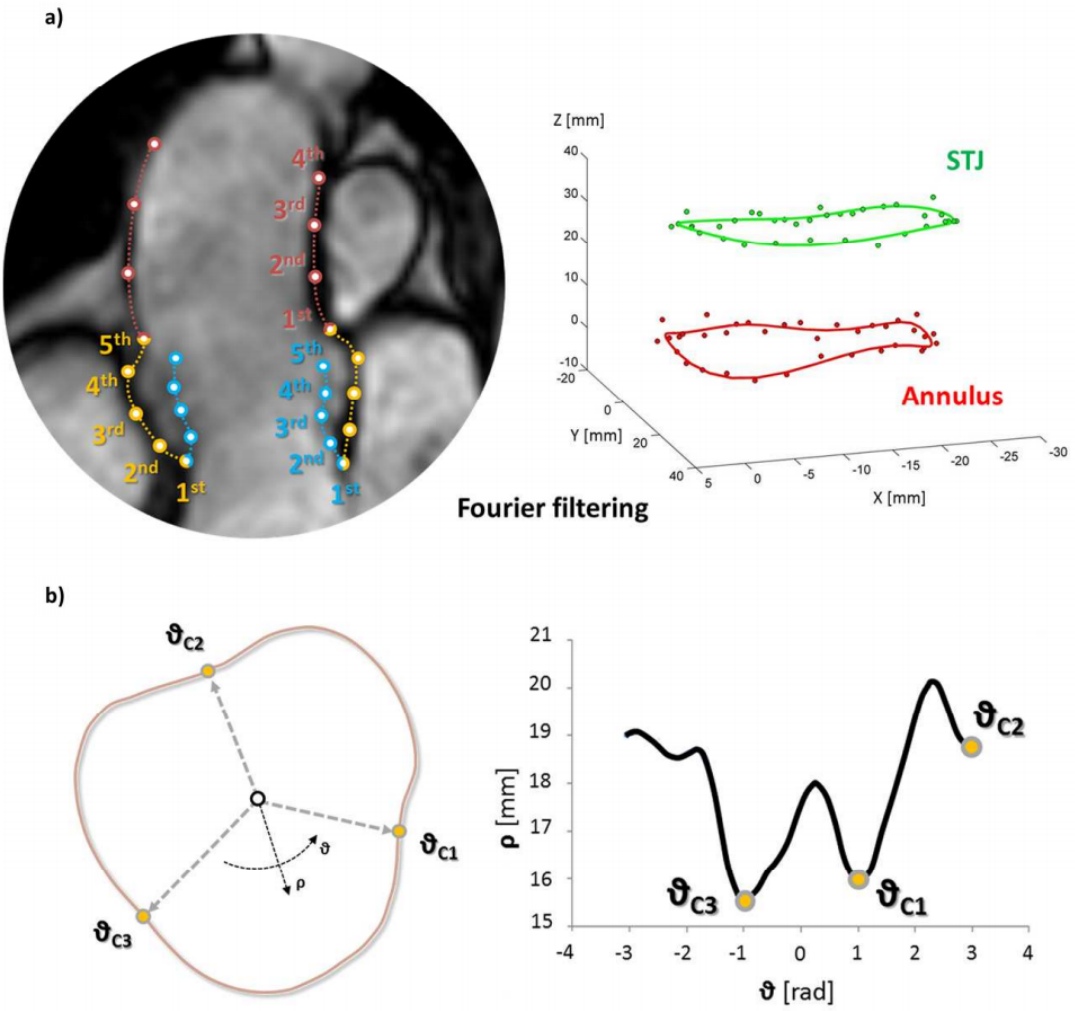

Figure 29: a) sets of uniformly distributed points, along the longitudinal axis of the AR, on AR sub-structures and Fourier filtering of cMRI data; b) definition of commissural boundaries, between the three Valsalva sinuses, on the 3rd filtered level of points generated for the Valsalva sinuses.

A novel optional smoothing operation was implemented in our script in order to assure a corner-free reconstruction of the leaflets surface. This procedure may be necessary when the leaflets are not clearly visible during the manual tracing. Detecting the profile of aortic valve leaflets on cMRI can be difficult, due to the low contrast between the leaflets and the surrounding blood. This limitation is linked to the fact that cMRI 2D images indeed are the planar representation of the result of an average operation over the thickness of a 3D slice. As a result, irrealistically folded or bent leaflet profiles can be obtained from the tracing procedure; these issue complicates the subsequent discretization procedure, in particular if solid elements are to be generated, e.g. through sweeping of the leaflet 2D discretized geometry.

Smoothing procedure description – the tracing procedure yielded five levels of points (traced levels) for each leaflet; the smoothing operation was performed on points from the 2^{nd} level to the 5^{th} level (Figure 30.a). This operation has two main goals: avoid abruptly folded shapes of the leaflet surface and avoiding unrealistically steep profiles of the leaflet free-margin (as exeplified in Figure31). The following operations were performed level by level, from the 2^{nd} one to the 5^{th} one, on the each set X_i of the points belonging to each specific level:

1. the plane P_{comm} containing the two commissures and the nadir was created.
2. all the X_i were projected on the plane P_{comm} creating the points X_{Pi} (Figure 30.b).
3. two other points were created: the mean point C_m between the two commissures (C_{left}, C_{right}) and the mean point X_m of the points X_{Pi}.
4. a new point X_H was defined at half distance on the line connecting C_m and X_m.
5. a plane $P_{\perp}$ perpendicular to P_{comm} was created at the point X_H; then, all points X_{Pi} were projected on $P_{\perp}$ as X_{Si} (Figure 30.c).

Applying the smoothing process to all the traced levels of the leaflet provided as final result a new surface for the smooth AR model, as shown in Figure 30.d.

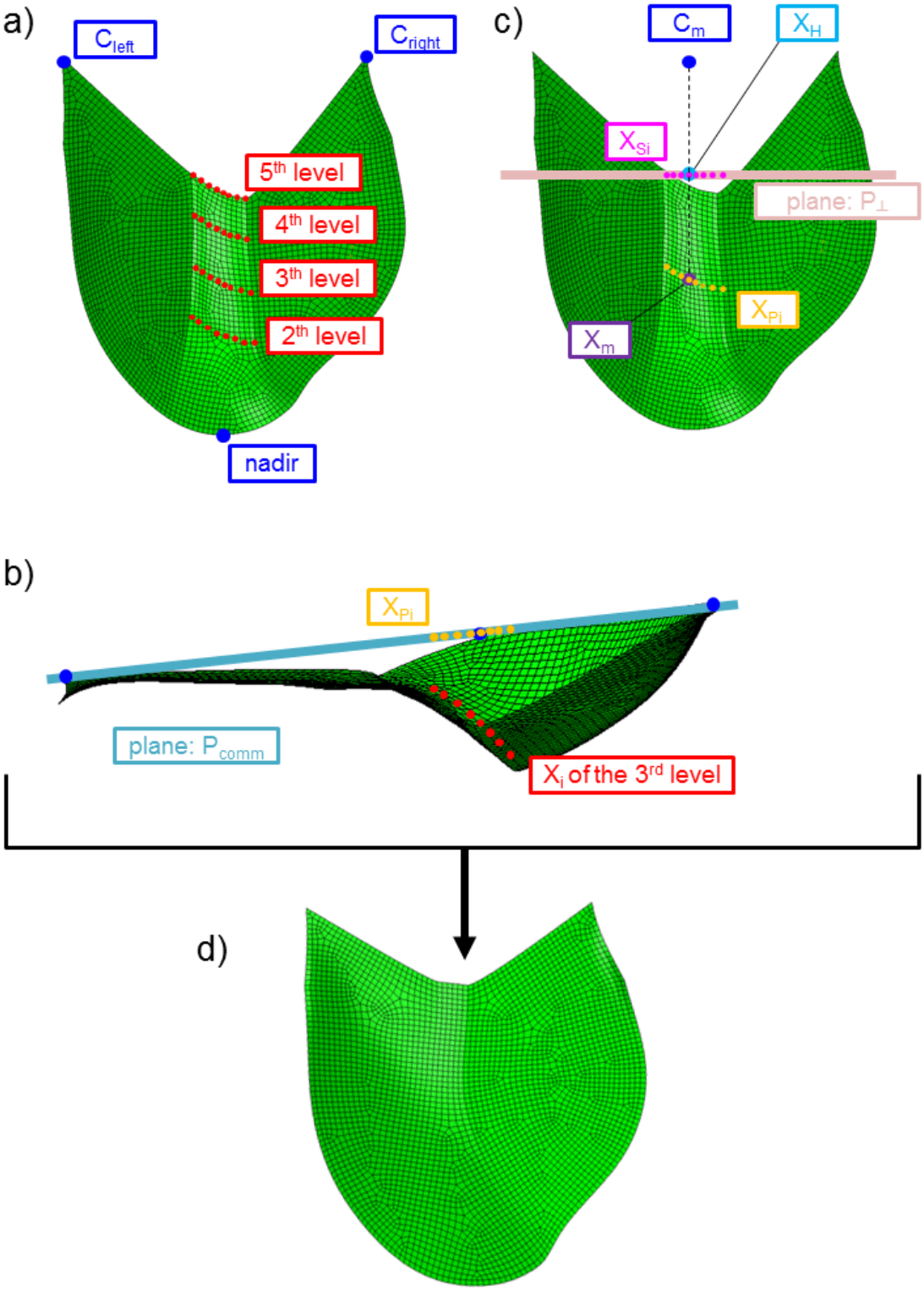

Figure 30: A brief explanation of the main steps of the smoothing procedure: a) the starting configuration: *red* points represent the four levels (from the 2^{nd} level to the 5^{th}) where the smoothing procedure is performed level by level. b) step #2 for the 3^{rd} level: *red* points (X_i) are projected on the *cyan* plane (P_{comm}) creating the *orange* points (X_{Pi}). c) step #5 for the 3^{rd} level: *orange* points (X_{Pi}) are projected on the *pink* plane ($P_{\perp}$) creating the *magenta* points (X_{Si}). d) Final result obtained applying the smoothing procedur to all the traced levels of the leaflet.

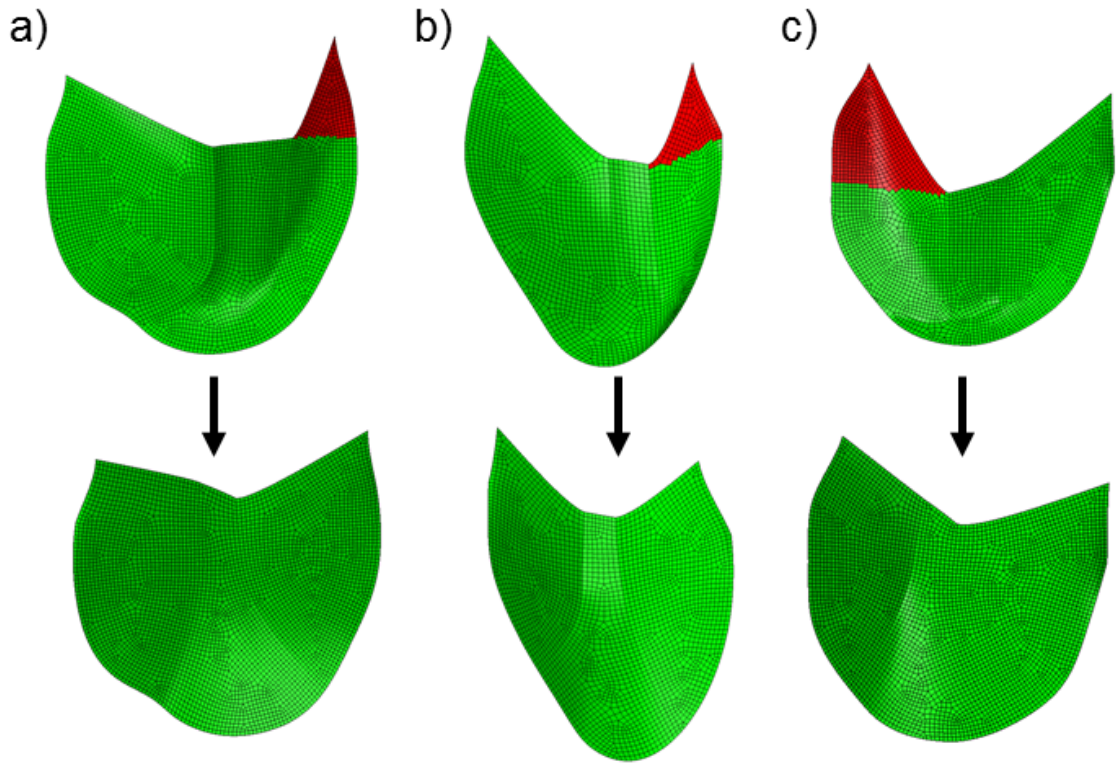

Figure 31: One example for each model of the leaflet geometry before (*upper panel*) and after (*lower panel*) the smoothing process (a) AR1 model; b) AR2 mode; c) AR3 model). *Red* zones highlight very steep leaflet regions.

Thanks to this procedure, two ASCII files, NSM.jou (without smoothing procedure) and SM.jou (with smoothing procedure), were finally written; each file contains the instructions needed by the CAD software Gambit© to generate and discretize the 3D geometrical model of the AR. The choice of the model to be actually passed to Gambit© is performed by the user still inside the Matlab© automated script; the 3D models are displayed on the screen and the user can navigate them to choose the final model to go on with (Figure 32). After the user's selection, the *.jou* file corresponding to the picked model is imported by Gambit© for the next step (GAMBIT I).

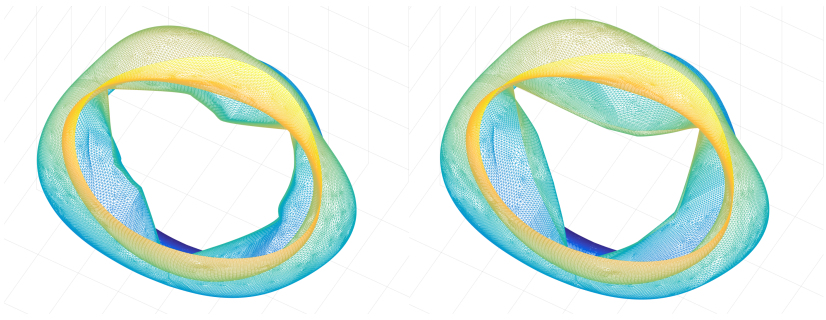

Figure 32: *Left hand panel*: non-smooth model. *Right hand panel*: smooth model.

5.3.2 Generation and discretization of the AR geometry (GAMBIT I)

This step started importing the *.jou* file coming from MATLAB I, containing the instructions for the geometry reconstruction and discretization. Owing to the previous filtering and resampling procedure, within each region vertexes were inherently arranged in a regular and mapped scheme, which allowed for interpolating them with two sets of edges defined as non-uniform rational cubic splines (NURBS), running in the axial and circumferential direction of the AR, respectively. NURBS were then interpolated by bi-cubic surfaces, defined in Gambit© as a Net Surface, to obtain three regions that shared their common boundaries and formed the whole aortic wall (Figure 33). In this reconstruction, interleaflet triangles were not distinguished from the remaining portion of the aortic wall. Hence, the crown-shaped profile of leaflets insertion line onto the aortic wall was defined, through two steps: first, a NURBS extending from commissure to commissure was defined by interpolating seven points. In particular, the two ends of the NURBS were located on the two longitudinal edges representing the boundaries with the adjacent sides of the aortic wall, and positioned below the STJ by $\frac{1}{4}$ of the extent of the edge from the STJ to the annulus. The third point was located on the annulus level and positioned halfway between the two ends along the circumferential direction. The remaining points were defined according to geometrical criteria and to prevent from unrealistic oscillations in the profile of the NURBS. Second, the NURBS was projected onto the aortic root surface to obtain the line of insertion of the leaflet. As for the aortic wall, a net of NURBS was generated interpolating filtered points, which run in the leaflet basis-to-free edge direction and in the commissure-to-commissure direction, respectively. The central portion of leaflet surface was obtained by bi-cubic interpolation of the corresponding NURBS, while the commissural regions were obtained using the corresponding boundaries as wireframe.

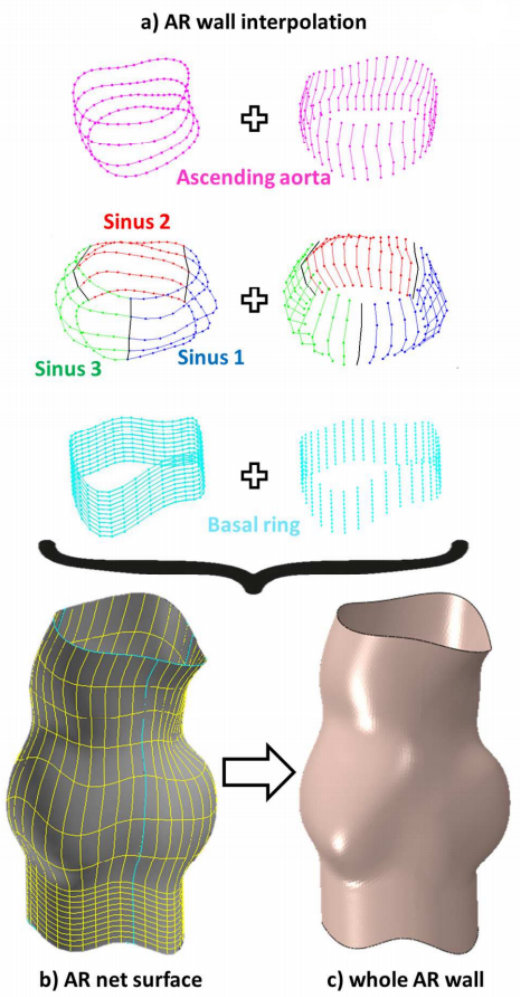

Figure 33: Reconstruction of AR geometry: a) regular and mapped scheme of vertex interpolation through non-uniform rational cubic splines (NURBS) on the ascending aorta, Valsalva sinuses and annular basal ring, in the circumferential (*left hand column*) and axial (*right hand column*) AR direction; b) Net Surface resulting from NURBS interpolation through bi-cubic surface; c) whole AR wall surface.

The aortic wall and the leaflets were discretized using four-node elements with a characteristic dimension of 0.4 mm and a pave mesh scheme. Since the aortic wall and the leaflets were reconstructed and discretized separately, there was no continuity between the meshes of the two regions at this stage of the procedure. The mesh was finally exported in a *.neu* file, i.e. an ASCII file containing the definition of the 3D cartesian coordinates of the mesh nodes and their connectivity, which was the input for the next step of the procedure (MATLAB II).

5.3.3 Nodes revision at the leaflet-sinus interface (MATLAB II)

This step started with the conversion of the *.neu* file, exported from GAMBIT I, into an *.inp* file through an ad hoc Matlab© function. The *.inp* file was read by Matlab©, and its content, i.e. the definition of nodes and connectivity, was stored in the Matlab© workspace. As already said, mesh continuity was not satisfied at the leaflet-wall interface. For this reason, the first operation performed based on the aforementioned information was aimed to obtaining mesh continuinty. In detail, the mesh of each sinus was considered; for each sinus, the nodes laying on the insertion line facing the corresponding leaflet basis were identified, based on their valence, i.e. the number of elements containing the node in exam. Indeed, since the insertion line is a boundary of the sinus surface, the valence of the nodes laying on it cannot be greater than 3. The identified nodes were then counted and used to define the number of nodes to be generated on the corresponding leaflet basis in order to obtain a one-to-one node correspondance. Following this step, a new *.jou* file to be imported by Gambit© was generated, which included the instructions to seed the leaflet boundary lines accordingly. In addition, as detailed in subsection 5.3.4, the file included also the instructions to generate appropriate bounday layers on the sinus surfaces, which were aimed at controlling the local mesh and providing the basis for the 3D solid mesh of the leaflets.

5.3.4 Generation and discretization of the revised AR geometry (GAMBIT II)

As for GAMBIT I, this step started by importing a *.jou* file, this time coming from MATLAB II. This file contained the same instructions of the file imported by GAMBIT I, except for the boundary layers on the sinuses and the sizing.

More specifically, on each sinus free-margin a boundary layer was inserted with the *blayer create* option; this operation creates four rows of ordered elements with a size of 0.4 mm, making the area closed to the each sinus free-margin very regular and easy to contol. Then the sizing calculated in the MATLAB II step was imposed to the meshing procedure of the leaflets attachement-edge. As already said, thanks to those operations

the mesh in the sinuses free-margin area exhibited a very regular aspect, an example is shown in Figure 34; this characteristic was fundamental for the procedures to be performed in the MATLAB III step, where the regularity of the mesh was mandatory for the success of the full volume mesh creation phase. Furthermore, the sizing operation made possible to reach the one-to-one node correspondance between the nodes of the leaflets attachement-edge and of the sinuses free-margin; after the meshing operation, in fact, the number of nodes of those two edges was exactly the same.

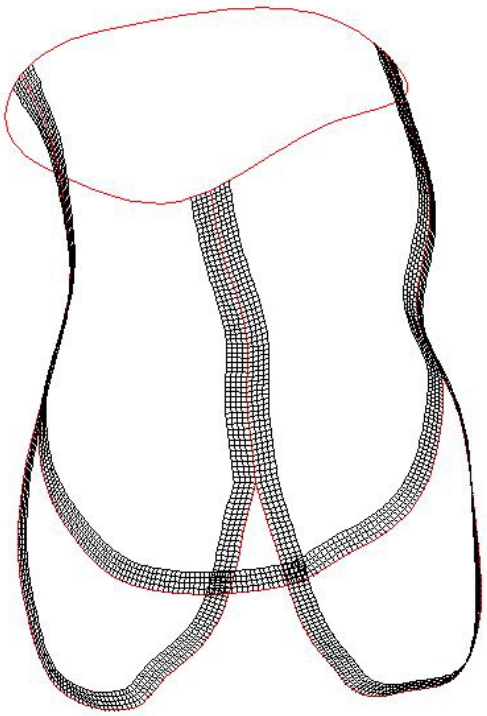

Figure 34: Boundary layers on the sinus free-margins.

At the end of this step the mesh was finally exported in a *.neu* file that will represent the input for the next step MATLAB III.

5.3.5 Full volume mesh creation and final .inp files writing (MATLAB III)

As for MATLAB II, this step started converting the *.neu* file, coming from the previous step, into an *.inp* file through the same function used before. The data were imported from the *.inp* file into the Matlab© workspace and were ready to be further processed. During MATLAB III, depending on the model to be created (SH, 3D-HT, 3D-MT), up to four main operations were accomplished: i) creation of the mesh continuity between AV leaflets and AR wall; ii) creation of a full volume mesh on the wall; iii) creation of a full volume mesh on the leaflets; iv) manipulation of the mesh to create a thickness modulation on the leaflets.

Mesh continuity → This operation was performed for all models, and consisted of two manipulations. First, the nodes of the attachment-edge of each leaflet were ordered from the left to right looking the leaflet surface from the aortic side; the nodes of the corresponding sinus free-margin were ordered accordingly. Second, the node-to-node correspondance between sinus free-margin and leaflet attachment-edge was identified; since the two edges had approximately equal extent and were seeded with an equal number of nodes, the i-th node of one edge corresponded to the i-th node of the complementary edge. Based on this correspondance, mesh continuity could be easily imposed by manipulating the corresponding connectivity matrix, i.e. by substituting each node of the leaflet attachment-edge with the corresponding node of the sinus free-margin. The result was a new connectivity matrix in which elements of the leaflets and of the sinuses shared the same nodes at the interface (Figure 35).

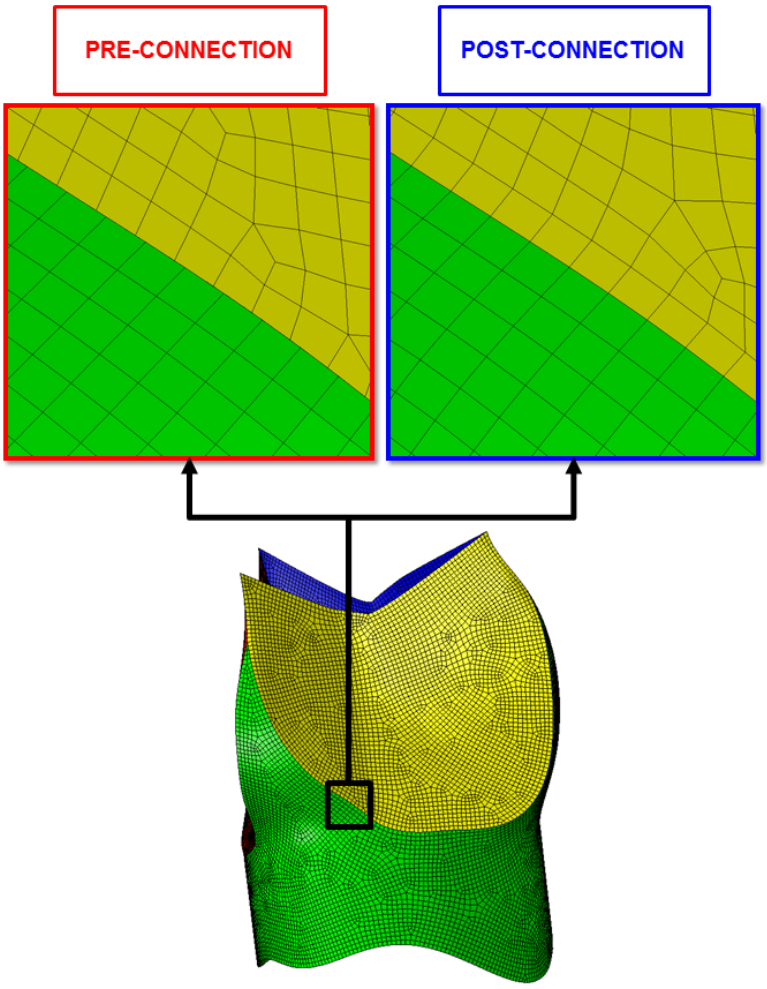

Figure 35: *Left hand panel*: pre-connection procedure; leaflet side and the wall side do not share the same nodes. *Right hand panel*: post-connection procedure; elements of the leaflets and of the sinuses share the same nodes at the interface.

Preliminary tests showed that this procedure sistematically yielded good quality meshes, provided that the characteristic dimension of the elements is lower than 1 mm. However, this threshold corresponds to a rather coarse mesh in the context of AR finite element modeling; for this reason, it was not considered a relevant limitation.

Full volume mesh on the wall → This operation was performed for all models. For each 4-node element of the aortic wall surface, three layers of hexahedral solid elements with reduced integration (ABAQUS© C3D8R elements) were generated. To this aim, an extrusion process was performed, where the original aortic wall nodes were copied and translated along the corresponding outward node normal. Depending

on the extrusion distance value, this procedure may encounter some problems, strongly dependent on the AR geometry of the model. As explain in detail in Appendix A, in case of local concavities in the original aortic wall surface, the smaller the local radius of curvature the shorter the extrusion distance that can lead to "twisted" solid elements when applying this procedure . In the three AR geometries reconstructed in the present work, such threshold was equal to 1.4, 1.2, and1.0 mm for models AR1, AR2, and AR3, respectively. Because of this preliminary result, and in order to have the same wall thickness for all AR models, a wall thickness equal to 1.0 mm was set in each model. The three layers of solid elements through the wall thickness accounted for 15%, 50% and 35% of the total thickness, consistently with ratios between the thickness of the three wall tunicae reported in the literature [16] (Figure 36).

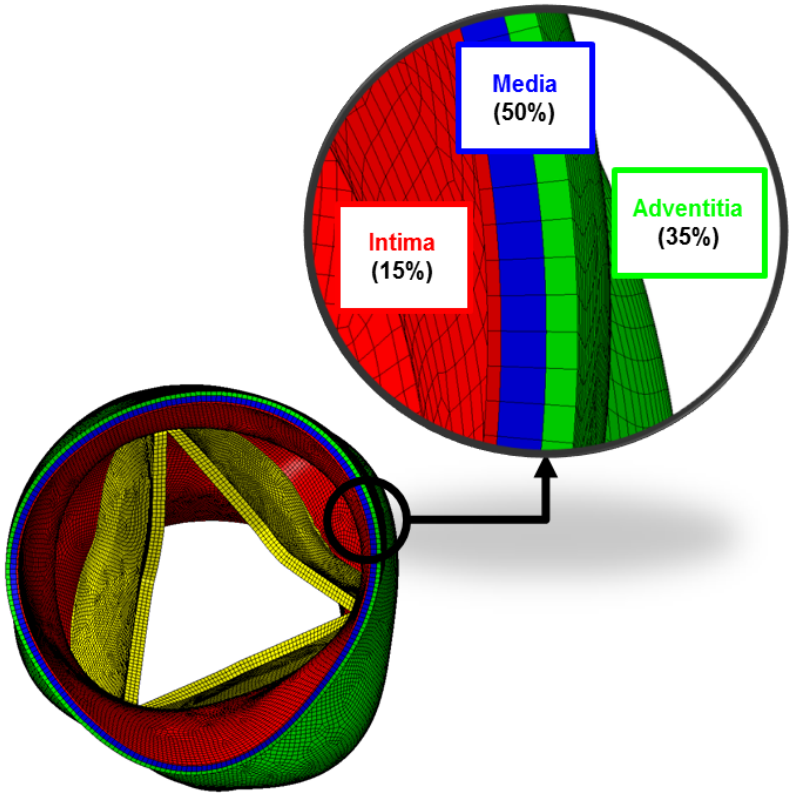

Figure 36: Final AR solid mesh and percentage redistribution of the intima (15%), media (50%) and adventitia (35%) layer.

Full volume mesh on the leaflets → This operation was performed for 3D-HT and 3D-MT models only. An extrusion process similar to the one implemented to generate the solid mesh of the aortic wall was used for the creation of the AV leaflets solid

geometry. Three layers of C3D8 elements were generated by copying and translating each node X_i of the leaflets along a specific vector v_i calculated as (Figure 37.a):

$$v_i = n_i(1 - e^{-\frac{C\alpha}{1-\alpha}}) + n_j(e^{-\frac{C\alpha}{1-\alpha}}) \tag{11}$$

where n_i is the local outward normal vector to the i-th node, n_j is the vector connecting X_j, the closest node to X_i on the sinus, and $X_j^{'}$, the sinus closest node to X_j in the extrusion direction, α is the ratio between the euclidean distance d_{ij} and the maximum distance from the sinus side within the all leaflets nodes, and C is a parameter that was empirically set equal to 2.5. In practise, the higher is the distance d_{ij}, the more v_i is a close approximation of n_i, the lower is the distance d_{ij}, the more v_i is a close approximation similar to n_j and aligned with the tangent to the aortic wall at the wall-leaflet interface. The final result are the three multi-layer leaflets shown in Figure 37.b.

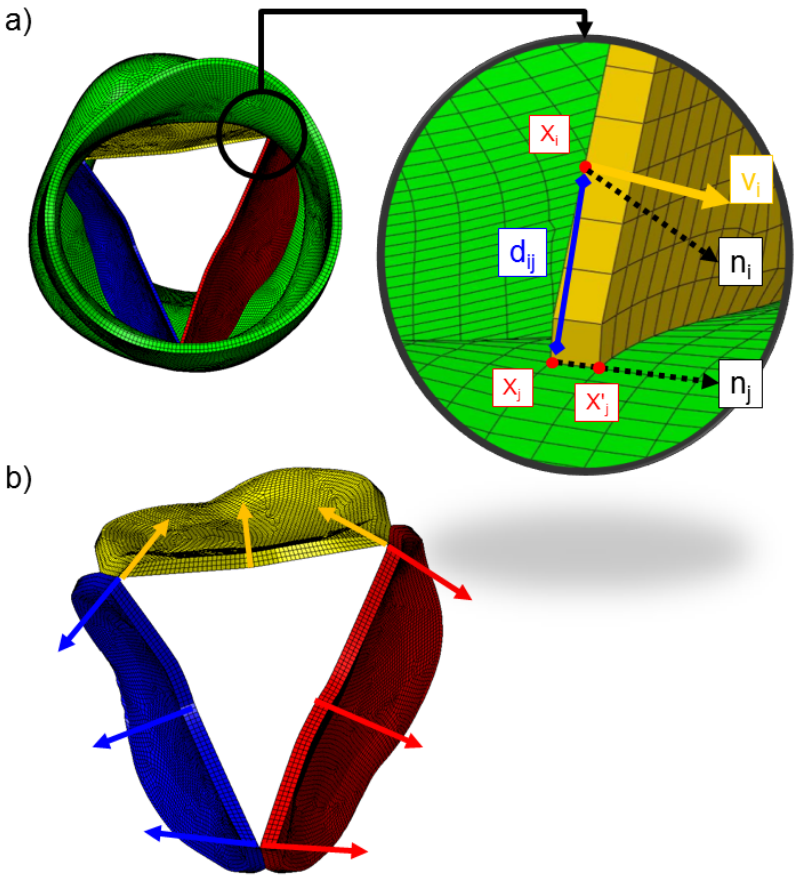

Figure 37: Procedure to create a full volume mesh on the leaflets with an homogenous thickness value along the entire surface. a) An example of the normal vector manipulation performed on each node across the leaflet surface; the *yellow* vector, v_i, is the final vector along which the node X_i is extruded. b) The principal directions along which the extrusion process was performed are shown by the arrows.

Of note, the generation of the three-layer mesh results also in three new attachment-edges that need to be connected to their counterpart on the aortic wall interior surface. However, the identification of this counterpart and of the node-to-node correspondance between leaflet and aortic wall meshes is straightforward, thanks to the use of the boundary layers on the aortic wall. Indeed, these generated three rows of nodes that closely match the new attachment-edges. Once again, mesh continuity is imposed by manipulating the connectivity matrix of the mesh (nodes "gluing" operation): the nodes of the n-th attachement-edge were substituted with the corresponding nodes on the aortic wall inner surface. In order to avoid any mesh distiortions coming from this operation, the thickness value of each layer at the connection area had to be exactly equal to the characteristic dimension of the elements. This implies that, for the 3D-HT model, the leaflet thickness was always equal to three times the mesh size set when generating the boundary layers. In Figure 38 a detail of a 3D-HT model is shown before and after the nodes gluing process.

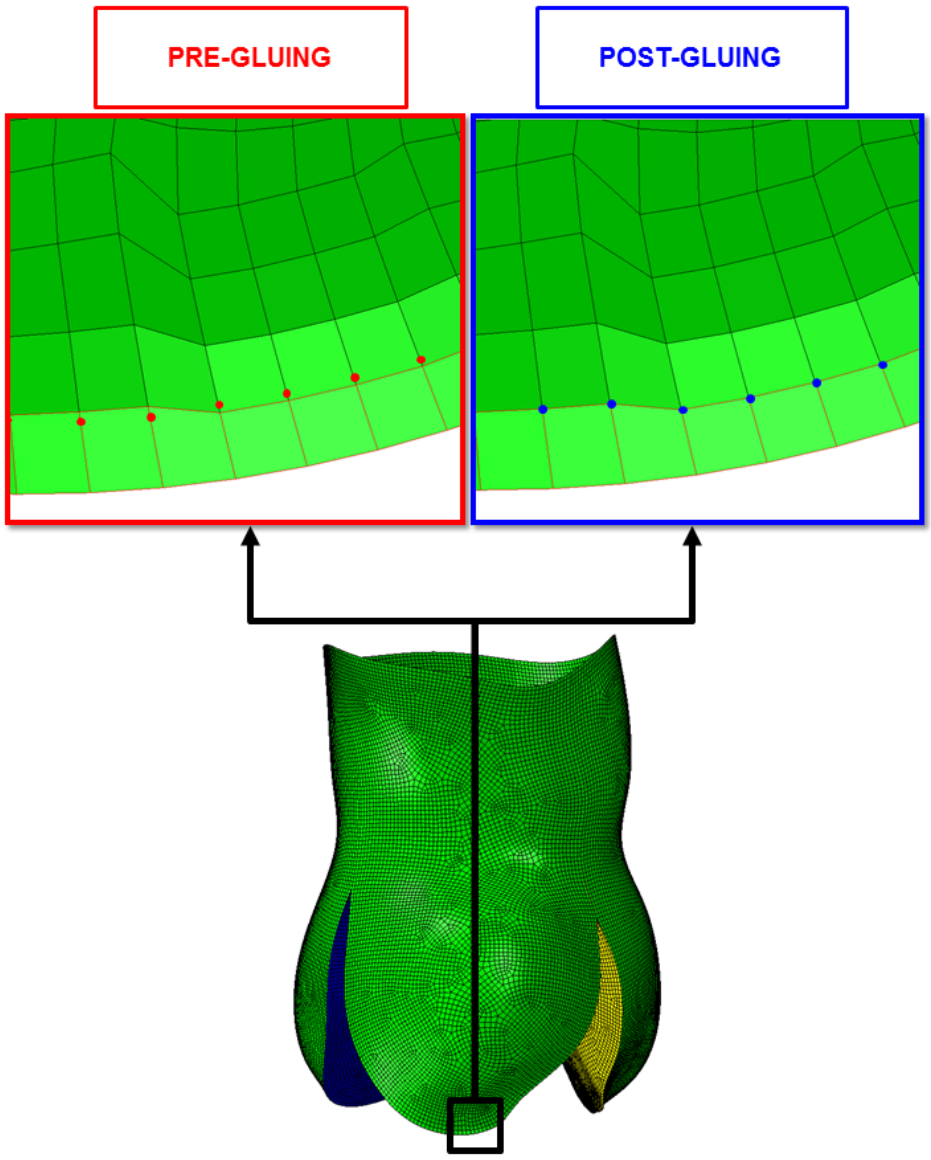

Figure 38: Gluing process for the 2nd attachment-edge of the left leaflet. *Left hand panel*: pre-gluing procedure; the leaflet side and the wall side do not share all the same nodes. *right hand panel*: post-gluing procedure; leaflets and sinuses' elements share the same nodes through the entire interface area.

Thickness modulation → This operation was performed for 3D-MT models only. During the creation of the leaflet volumetric mesh, for each node of the leaflet a space-dependent thickness value was assigned through an ad hoc Matlab© function (*modulated_thickeness.m*). Since the leaflet regional thickness was not assessable from cMRI, the thickness pattern was assumed based on region-dependent values reported in the literature and that were different for each leaflet (Figure 39) [16]. In order to reproduce the same variation in thickness, the original leaflet surface mesh were mapped; two euclidean distances were evaluated for each node: d_{FM}, the distance between the

node and the corresponding closest node of the free-margin of the leaflet, and d_{AE}, the distance between the node and the corresponding closest node of the attachment-edge of the leaflet. The leaflet surface was diveded in four regions according to the following rules:

1. $d_{FM} \leq 5\,\text{mm} \wedge d_{AE} > 5\,\text{mm} \rightarrow$ *free-margin region*: linear decreasing in thickness from 1.2 mm (mesh size) for the nodes closer to free-margin down to 0.3 mm.

   $$\Delta s = 1.2(1 - \alpha_{FM}) + 0.3\alpha_{FM} \quad \text{mm}$$

   where $\alpha_{FM} = d_{FM}/5$

2. $d_{AE} \leq 5\,\text{mm} \wedge d_{FM} > 5\,\text{mm} \rightarrow$ *attachment-edge region*: linear decreasing in thickness from 1.2 mm (mesh size) for the nodes closer to attachement-edge down to 0.3 mm.

   $$\Delta s = 1.2(1 - \alpha_{AE}) + 0.3\alpha_{AE} \quad \text{mm}$$

   where $\alpha_{AE} = d_{AE}/5$

3. $d_{FM} > 5\,\text{mm} \wedge d_{AE} > 5\,\text{mm} \rightarrow$ *belly region*: constant thickness equals to 0.3 mm.

   $$\Delta s = 0.3 \quad \text{mm}$$

4. $d_{FM} \leq 5\,\text{mm} \wedge d_{AE} \leq 5\,\text{mm} \rightarrow$ *intersection region*: decreasing in thickness from 1.2 mm (mesh size) for the nodes closer to attachement-edge down to 0.3 mm.

   $$\Delta s = 2 \times 0.3 \frac{5 + 5}{d_{FM} + d_{AE}} \quad \text{mm}$$

   In the case of nodes with d_{FM} and d_{AE} both equal to zero a control was implemented to set $\Delta s = 1.2\,\text{mm}$. Moreover, for small values of d_{FM} and d_{AE} the value of Δs could be greater than 1.2 mm: in that case another control set this parameter equal to 1.2 mm.

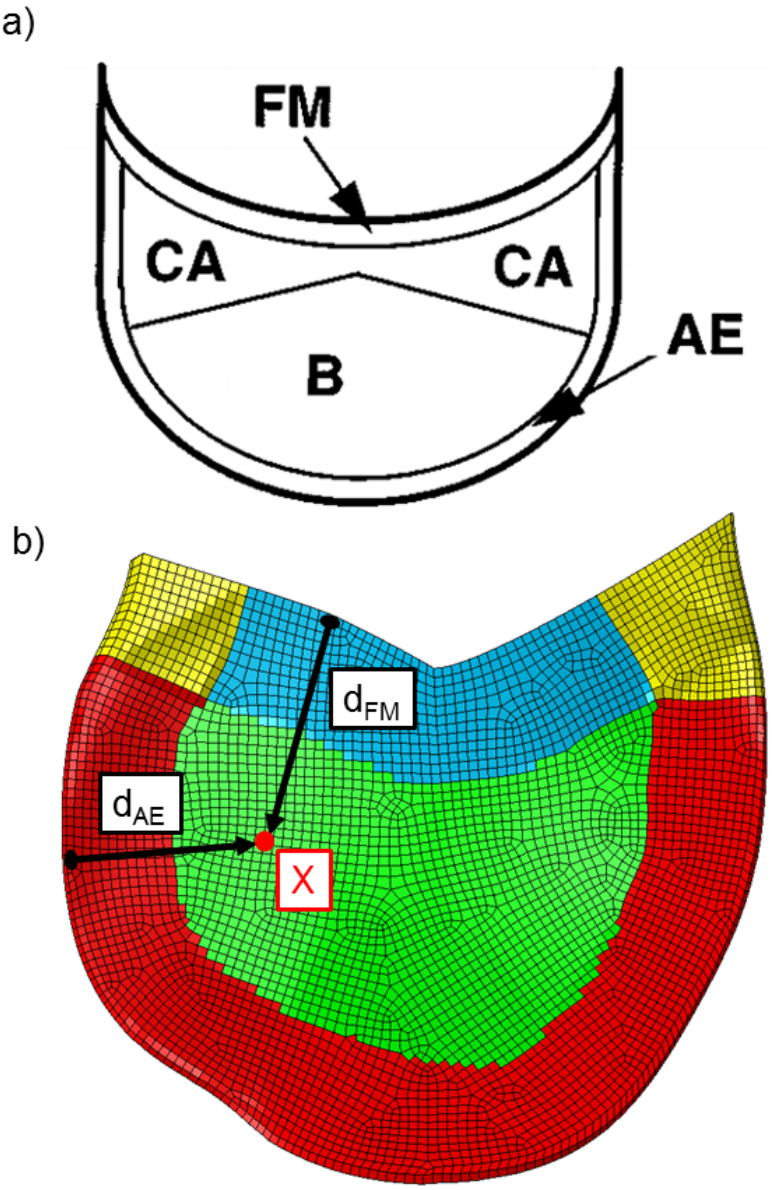

Figure 39: Thickness modulation procedure: a) diagram of leaflet regions. B: belly, FM: free margin, CA: coaptation area, AE: attachment edge. b) the four regions created in our model for the thickness modulation: *blue*: free-margin region; *red*: attachment-edge region *yellow*: intersection region; *green*: belly region. X is a generic point inside the leaflet surface, d_{FM} and d_{AE} era the corresponding distances from the two boundary edges (Free Margin, d_{FM}; Attachment Edge, d_{AE}) used to map the nodes across the leaflet surface. In this case, these two distances are higher than the corresponding thresholds, hence the point belongs to the belly region and a thickness value of 0.1 mm was assigned to it.

At the end of the procedure a volumetric mesh with three layers was created fo each leaflet; at each point of the leaflet surface, the thickness of each layer was exactly one third of the total thickness value.

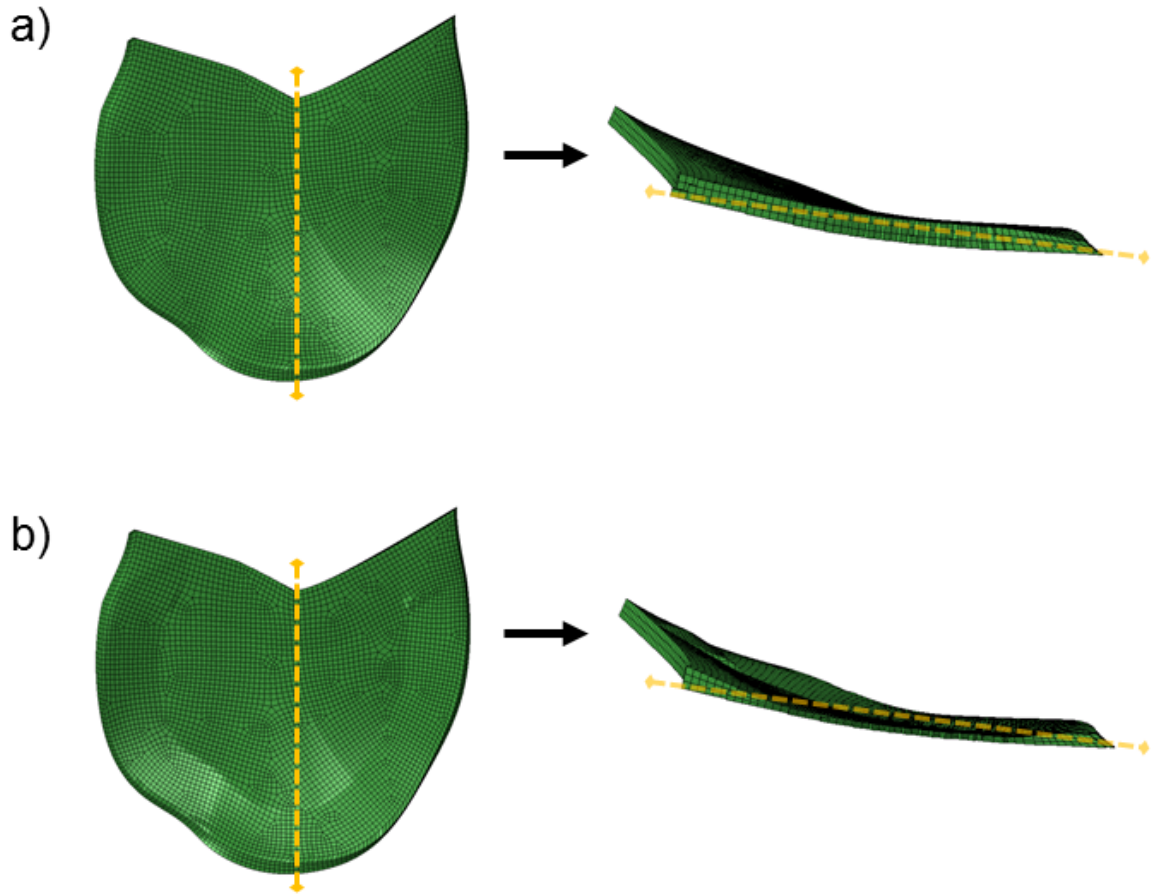

Figure 40: Differences between a leaflet with and without a modulated thickness: a) frontal view (*left hand panel*) and a section (*right hand panel*) of the leaflet with a constant thickness. b) frontal view (*left hand panel*) and a section (*right hand panel*) of the leaflet with a modulated thickness.

The described procedures allowed to obtain the final 3D discretized geometrical model of the AR. The corresponding definition, together with the definition of the tissues' mechanical properties and of the boundary conditions (see sections 5.4 and 5.6), was automatically written in the input (*.inp*) files for the subsequent simulations in ABAQUS/Explicit. Two *.inp* files was created for each model:

1. pre-stress initialization file (*namefile-I.inp*), needed for the simulation aimed to computing the pre-stresses characterizing the initial configuration of the AR.

2. cardiac cycle simulation file (*namefile-C.inp*): needed to simulate AR structural response throughout two consecutive cardiac cycles starting from the reconstructed and pre-stress AR geometry.

5.4 Tissues mechanical properties formulation

Two different material formulation was used in our AR model, one for the aortic wall and another one for the valve leaflets.

Aortic wall tissue: the mechanical response of the Valsava sinuses, of the interleaflets triangles and of the ascending aorta was modeled using a linear elastic and isotropic material, with a 2 MPa Young's modulus and a 0.45 Poisson's ratio to reproduce the almost incompressible behavior of the real tissue [12]. As detailed in the first chapter of the present thesis, the actual stress-strain response of aortic wall tissue is hyperelastic and anisotropic, however, both these features are markedly less pronounced as compared to aortic leaflet tissue [18] . Hence, the adopted approximation was considered acceptable. Also, as it will be clearer in subsection 5.5, the method adopted to compute aortic wall pre-stresses requires the use of a linear elastic model.

Leaflets tissue: AV leaflet tissue was described as a transversely anisotropic and hyperelastic material with the commissure-commissure direction assumed as the one characterized by the stiffest response owing to the presence of collagen fibers preferentially aligned along this direction. To this aim, the constitutive model proposed by Guccione and colleagues [17], which was originally proposed to model the orthothropic passive response of myocardial tissue, was implemented into a VUANISOHYPER_STRAIN subroutine for ABAQUS/Explicit©. Some fundamental equations regarding the theory of hyperelasticty, and helping to better undestand the following, are reported in Appendix B. In the implemented subroutine the Cauchy stress tensor $\boldsymbol{\sigma}$ is computed as:

$$\boldsymbol{\sigma} = \boldsymbol{S} - p\boldsymbol{I} \tag{12}$$

Where the first term is the *deviatoric term* of the stress tensor and the second one is the *volumetric term*. These are expressed as follows:

$$\boldsymbol{S} = \frac{1}{J}(\boldsymbol{F}\frac{\partial U}{\partial \boldsymbol{E}}\boldsymbol{F}^{\boldsymbol{T}}) \tag{13}$$

$$p\boldsymbol{I} = -\frac{\partial U}{\partial J} \tag{14}$$

Where U is the strain energy function characterizing the hyperelastic response of the material, $\boldsymbol{F}$ is the deformation gradient tensor, $J = det(\boldsymbol{F})$, and $\boldsymbol{E} = (1/2)(\boldsymbol{F^T F} - \boldsymbol{I})$ is the Green strain tensor.

The implementation of the subroutine requires the definition of the partial derivatives of the strain energy function with respect to the components of $\boldsymbol{E}$ and with respect to J.

The Guccione model uses this kind of strain energy function:

$$U = \frac{C}{2}(\exp Q - 1) + K(\frac{J^2 - 1}{2} - \ln J) \tag{15}$$

where C is the first constitutive parameter in MPa, J the $det\boldsymbol{F}$ and K the compressibility module and Q is formulated as follow:

$$\begin{aligned} Q = {} & b_1 * tr(E) + b_2 * E_{ff}^2 + \\ & + b_3 * (E_{ss}^2 + E_{nn}^2 + E_{sn}^2 + E_{ns}^2) + \\ & + b_4 * (E_{nf}^2 + E_{fn}^2 + E_{fs}^2 + E_{sf}^2) \end{aligned} \tag{16}$$

Where subscripts s,n,f define the local orthonormal coordinate system defining the three directions characterizing the orthothropic response of the tissue. b_1, b_2, b_3 and b_4 are the other constitutive parameters. In conclusion, the model just needs six parameters $(C, b_1, b_2, b_3, b_4, K)$ to completely describe the material properties, which are given to ABAQUS/Explicit© through the final *.inp* file. As said before, the formulation of Guccione was created to reproduce the passive behavior of the myocardial tissue and so a new set of parameters was needed to fit the behavior of the aortic cusps tissue. To identify this new set we used the constitutive model formulated by Billiar et al. [3] [4] as reference; we used it to reproduce the stress-strain behaviour of fresh porcine leaflets undergoing biaxial tensile tests (Figure 41).

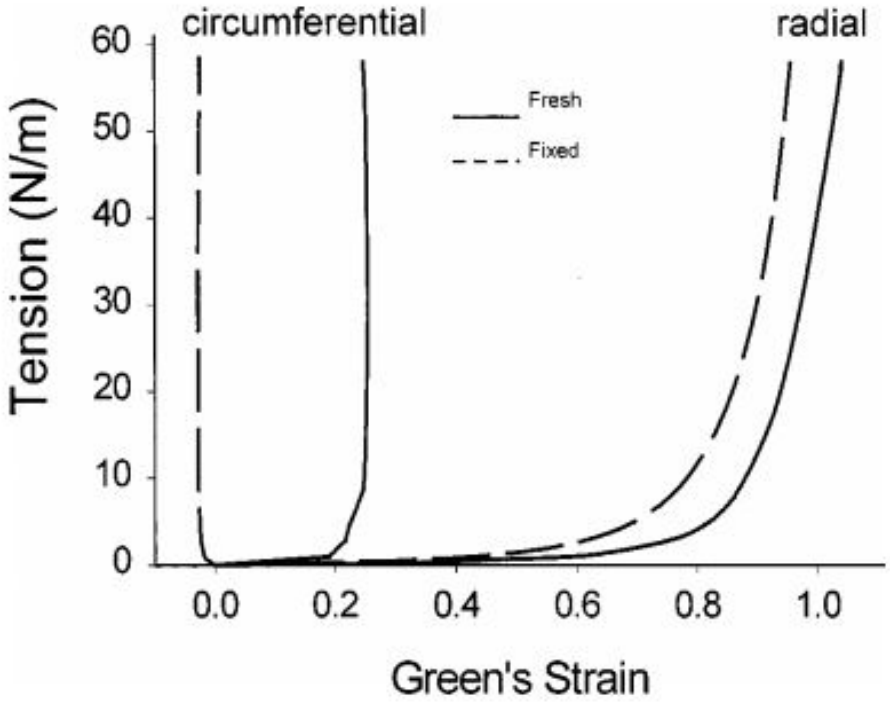

Figure 41: Representative circumferential and radial stress-strain curves from a fresh and a glutaraldehyde-fixed AV cusp, which show the pronounced mechanical anisotropy of both tissues [3].

The model proposed by Billiar and Sacks is completely different from the Guccione model, in that a Gaussian distribution is assumed for the direction of collagen fibers within the tissue instead of assuming a single preferential direction. According to that model, the following exponential stress-strain law for the Lagrangian fiber tensions (force/unit length):

$$S^*_{ff} = A^*(e^{BE_{ff}} - 1) \tag{17}$$

where A^* and B are material parameters and E_{ff} is the fiber Green's strain calculated as $E_{ff} = 0.5(\lambda^2_{ff} - 1)$. The fiber stretch ratio λ_{ff} of a fiber orientated at an angle θ with respect to the commissure-commissure direction is obtained starting from the deformation gradient $\boldsymbol{F}$ referred to the biaxial test directions (1 = commissure-commissure; 2 = radial, i.e. basis-to-free edge; 3 = out of plane):

$$\begin{aligned} \lambda^2_{ff} = {} & (\lambda^2_{11} + \lambda^2_{21})\cos(\theta)^2 + \\ & + 2(\lambda_{11}\lambda_{12} + \lambda_{22}\lambda_{21})\cos(\theta)\sin(\theta) + \\ & + (\lambda^2_{22} + \lambda^2_{12})\sin(\theta)^2 \end{aligned} \tag{18}$$

The angular collagen fiber distribution in the leaflet area was described with a Gaussian

distribution given by:

$$R(\theta) = \frac{1}{\sigma\sqrt{2\pi}} e^{\frac{-(\theta-\mu)^2}{2\sigma^2}} \tag{19}$$

The final form of the structural constitutive model yields the following relationships for the Lagrangian membrane tensions along the test axes (circumferential and radial):

$$T_{11} = \int_{-\frac{\pi}{2}}^{\frac{\pi}{2}} S_f^* R(\theta)(\lambda_1 \cos(\theta)^2 + \lambda_{21} \cos(\theta)\sin(\theta))d\theta \tag{20}$$

$$T_{22} = \int_{-\frac{\pi}{2}}^{\frac{\pi}{2}} S_f^* R(\theta)(\lambda_2 \sin(\theta)^2 + \lambda_{12} \cos(\theta)\sin(\theta))d\theta \tag{21}$$

To find the set of parameters needed, we calculated the analytical stresses predicted by the Guccione and Billiar models in a virtual displacement controlled biaxial test, where we imposed a circumferential and radial deformation; in this test we let the nominal circumferential deformation ϵ_{cc} increase from 0.0 to 0.25 and the nominal radial deformation ϵ_{ff} increase from 0.0 to 0.75. Those two different values have been chosen to reach for both the direction the steepest zone of the stress-strain curve (Figure 41). Minimizing the mean quadratic error, we found the parameter set for the Guccione's model which best fitted the values predicted by the Billiar's model. In this context, we decided to neglect the volumetric term imposing the incompressible condition $J = det\boldsymbol{F} = 1$, setting $F_{nn} = \frac{1}{\lambda_{ff}\lambda_{ss}}$. The first parameter set that we obtained assured a very good fitting (Figure 42), with an average mean quadratic error $err = 5.4 \cdot 10^{-5}$MPa, for average stresses in the order of $5 \cdot 10^{-2}$MPa:

$$C = 1.41 \cdot 10^{-4}\text{MPa}, b_1 = 0.0, b_2 = 22.7785, b_3 = 3.4995, b_4 = 9.9630 \tag{22}$$

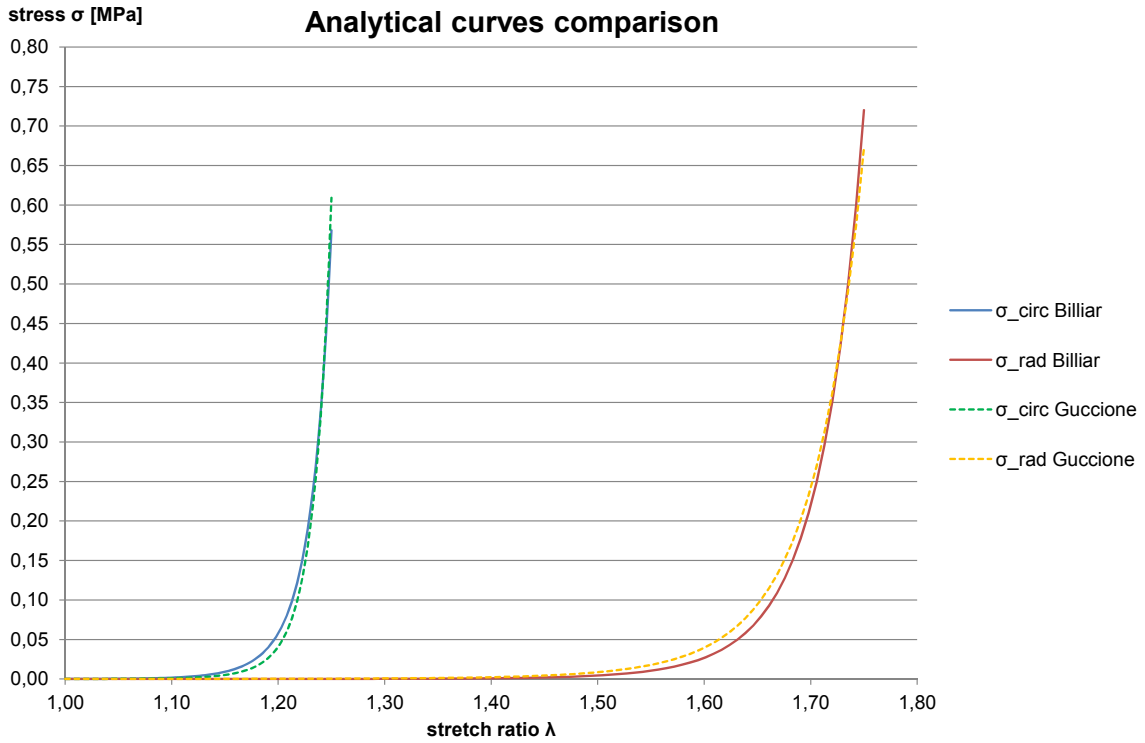

Figure 42: Analytical stress-strain curves for the Guccione model (dashed lines) and the Billiar model (continuous lines) using the first parameter set.

To further test this set of paramenter, we simulated the same displacement controlled biaxal test in ABAQUS/Explicit© for two patches geometrically reproducing the specimens used in the experiments of Billiar [3] [4], one discretized with shell elements and the other one with C3D8 elements (Figure 43).

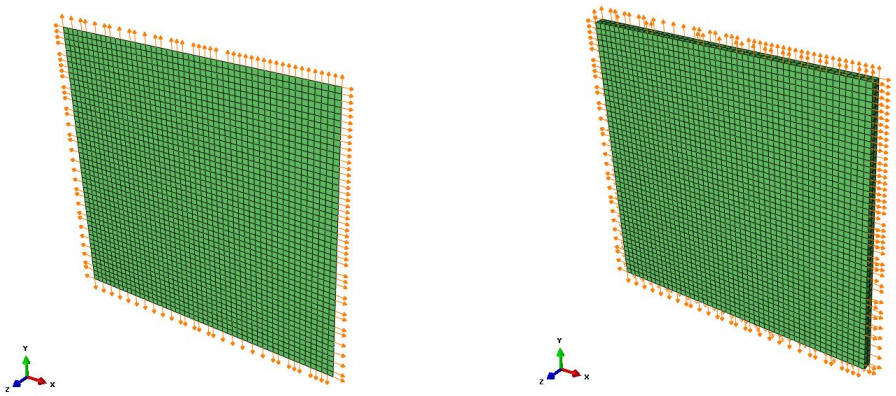

Figure 43: The two patch models used for the numerical simulations. *Right hand panel*: shell elements patch . *Left hand panel*: solid elements patch.

For both models we imposed the previously defined displacements as nodal displacements that linearly increased over a timeframe of 1 s, and we defined the material properties through the Guccione's model VUANISOHYPER_STRAIN subroutine. Two versions of the subroutine were implemented, taking into account the different formulation of the elements in the two cases (SH and 3D-HT). For these simulations we had to cope with the fact that ABAQUS/Explicit© is not able to reproduce perfectly incompressible material behaviours; for this reason we needed to define a value of K, which set equal to 1 MPa as in the work of Jerminov [20] as a first educated guess. With this initial set of parameters the numerical solution of the biaxial test was far from matching the analytical response predicted by the Billiar's model for an incompressible material. Hence, a finer tuning of the parameters was performed. As a result, the following values were identified:

$$C = 2.82 \cdot 10^{-3}\text{MPa}, b_1 = 0.0, b_2 = 12.8396, b_3 = 1.9672 b_4 = 9.9969, K = 50\text{MPa} \quad (23)$$

As we can see in the first graph of Figure 44, the agreement of the Guccione's analytical prediction with the numerical results provided by ABAQUS/Explicit© simulations is really good, whereas in the second graph the comparison between the numerical curves and the Billiar's model curves is less precise. However, in the range of deformation reached on the leaflet surface during the cardiac cycle [12], the error between the numerical and Billiard's curves was considered accetable.

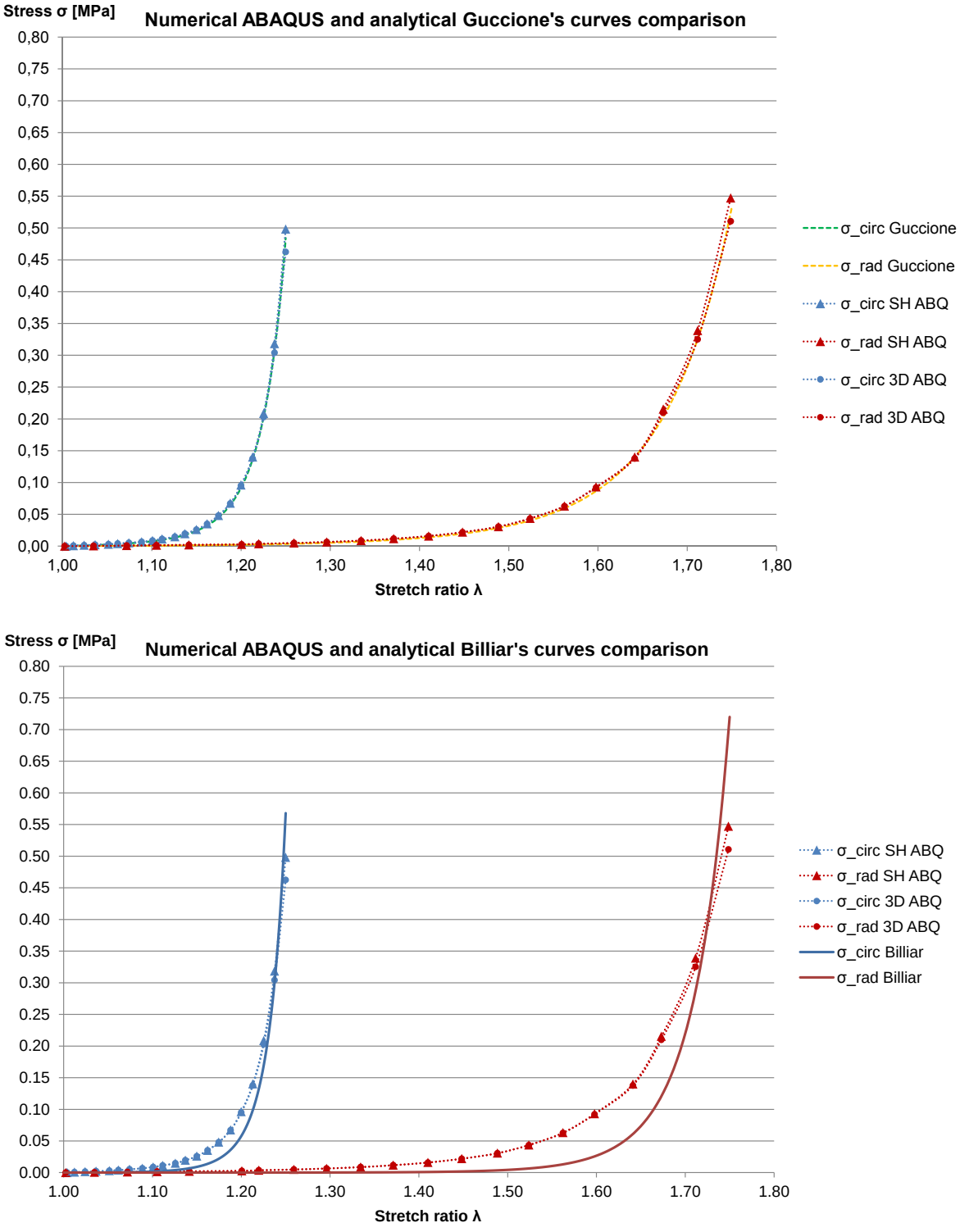

Figure 44: *Upper panel*: Analytical stress-strain curves for the Guccione model (dashed lines) and Abaqus© curves derived form the numerical biaxial experiments. *Bottomer panel*: Analytical stress-strain curves for the Billiar model (continuous lines) and Abaqus© curves derived form the numerical biaxial experiments.

Mass-scaling technique and Courant condition in explicit solver

The numerical solution for explicit methods is stable only if the *Courant condition* is satisfied:

$$\Delta t <= \frac{\Delta x}{\sqrt{\frac{E}{\rho}}}$$

where Δt is the time step, Δx the characteristic dimension of the smaller mesh element, E the Young's modulus of the material and ρ the material density. In order to increase the Courant number and hence reduce the computational expense of simulations the *mass-scaling* technique was used: the density of all tissues was assumed equal to $11\,\mathrm{g/cm^3}$, i.e. ten times higher than the real value($1.1\,\mathrm{g/cm^3}$); this choice also permit to taking into account the blood inertia in the leaflets dynamics, without introducing artefacts in the solution [15].

In addition, to reduce the number viscoity the bulk viscosity coefficient was assumed equal to 0.06.

5.5 Computation of the pre-stress field

The computation of pre-stresses exploited the possibility, allowed for by Abaqus©, to compute stresses in a simulation and to apply these as pre-stresses in a subsequent simulation, in which the components of the Cauchy stress tensor are initialized elementwise to the previously computed value [1]. The adopted approach is schematized in Figure 45. The AR geometry as reconstructed from cMRI (Ω_{cMRI}) was used as geometrical configuration of the AR. Pre-stresses (σ_{pre}) were initially set to zero $\sigma_0 = 0$. A pressurization simulation was performed starting from these initial conditions: consistently with the assumed end-diastolic loading conditions, an 82 mmHg pressure load was applied to the inner surface of the aorta and of the aorto-ventricular junction. The pressure load increased linearly through time over a time-frame of 0.4 s (Figure 46.a). Contextually, nodal displacement boundary conditions were imposed to the nodes at the proximal and the distal ends of the AR model, so to allow only radial expansion or contraction of the AR wall. To this aim, at each end of the model a local cylindrical reference frame was defined. The origin of this reference frame was set at the center of mass of the nodes belonging to the relevant end of the model; the z-axis of the reference

frame was oriented as the normal to the least square plane approximating the nodes of interest. In this reference frame, nodes were allowed for radial motion, but their displacement in the axial and circumferential direction was prevented from (Figure 46.b). This simulation was then iterated as following: in the inflated configuration (Ω_{82}) the computed nodal displacement field (u_{82}) was checked for the entire aortic wall; if the peak value of displacement magnitude did not exceed the in-plane resolution of cMRI (Im_{res}), i.e. 1.10 mm, configuration Ω_{82} is considered equivalent to Ω_{cMRI}, and the corresponding Cauchy true stress field (σ_{82}) characterizing the aortic wall is considered the pre-stresses field σ_{pre} to be applied when simulating AR biomechanics throughout the cardiac cycle. Otherwise, σ_0 was updated and set equal to σ_{82}, and the pressurization simulation was performed again.
In the work herein reported, two iterations were sufficient to achieve consistency between Ω_{82} and Ω_{cMRI} for all models (AR1, AR2, and AR3).

5.6 Computation of AR biomechanics throughout the cardiac cycle

In a subsequent simulation, the structural response of the pre-stressed AR over the cardiac cycle was computed. The AR model in its undeformed configuration, i.e. Ω_{cMRI}, was considered and the Cauchy true stress field σ_{82} yielded by the iterative computation of pre-stresses was applied elementwise to the model as initial condition. Hence, a three-step simulation was run:

1. In the first step, which lasted 0.05 s, the prestressed AR was pressurized to its end-diastolic configuration. A uniform pressure load linearly increasing from 0 to 82 mmHg was applied to the inner surface of the aorta and of the aorto-ventricular junction (Figure 46.a), while all nodes of the model were prevented from any translation (Figure 46.b).

2. In the second step, which lasted 0.35 s, a stable equilibrium of the model was achieved. The 82 mmHg pressure load was kept constant (Figure 46.a) and kinematic boundary constraints were imposed only at the proximal and distal ends of AR wall. Specifically, at each end a local cylindrical reference frame centered

and aligned with the aortic was defined; in this reference frame, the nodes at the corresponding end of the model were prevented from circumferential and axial motion, and could translate only radially (Figure 46.b).

3. In the final-third step two consecutive cardiac cycles, each one starting at end-diastole and lasting 0.8 s, were simulated. To this aim, a time-dependent aortic pressure ranging from 82 to 124 mmHg was applied to the inner surface of ascending aorta and Valsalva sinuses; a time-dependent ventricular pressures ranging from -6 to 126 mmHg was applied to the inner surface of the ILTs and of the basal ring, and the difference between ventricular and aortic pressure was applied to the ventricular surface of AV leaflets (Figure 46.a). Concomitantly, the kinematic boundary conditions imposed in the second step were applied (Figure 46.b). Contact between AV leaflets, and between these and the aortic wall, was modelled through the general contact algorithm available in ABAQUS/Explicit©; interactions in the direction normal to the contacting surfaces were modelled through a scale penalty method, while tangential interaction were modelled using a friction coefficient of 0.05.

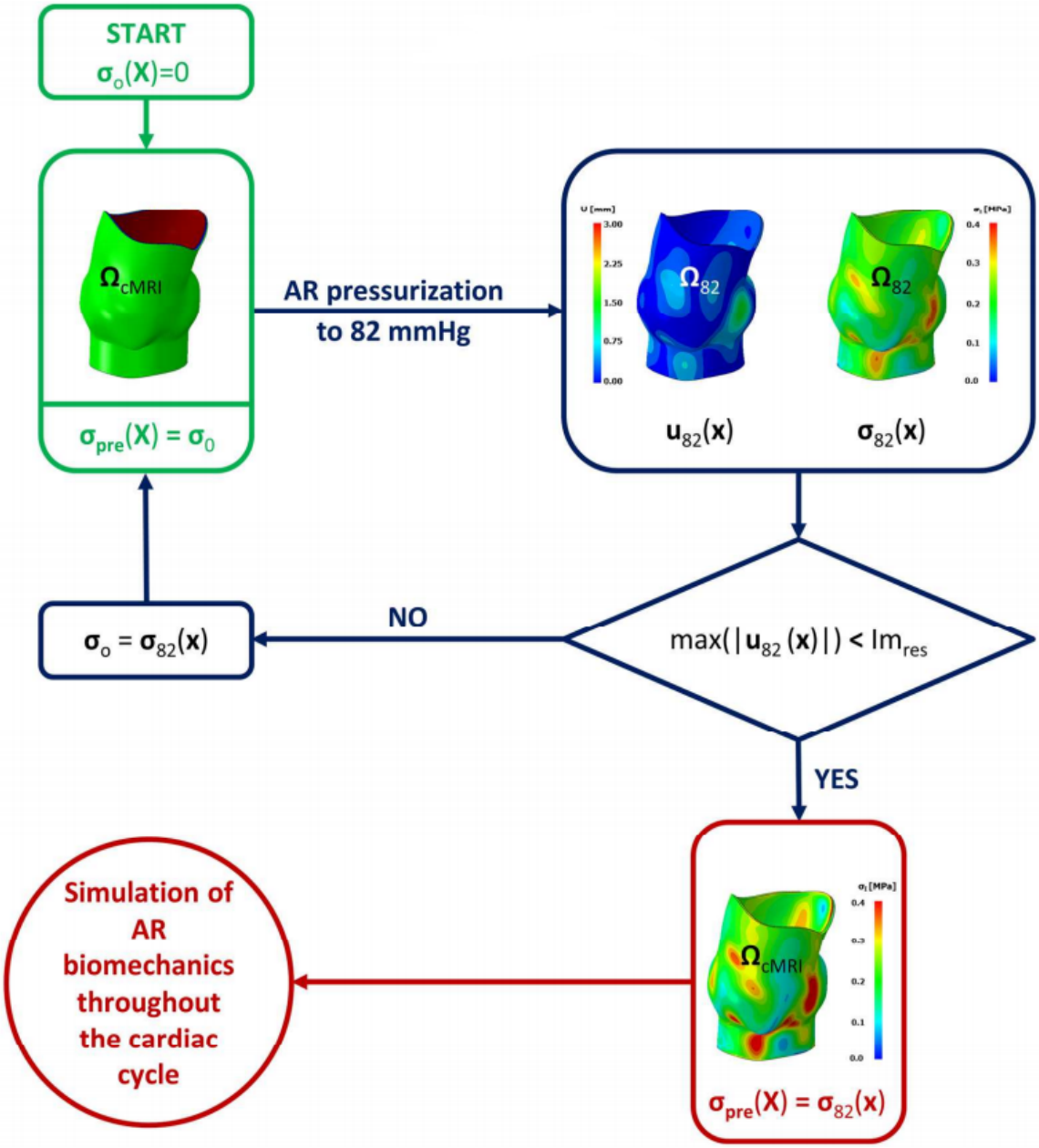

Figure 45: Workflow of pre-stress computation. AR geometry reconstructed from cMRI (Ω_{cMRI}) is initially characterized by zero pre-stresses ($\sigma_{pre} = \sigma_0 = 0$). The AR model is pressurized up to 82 mmHg through a uniform pressure load applied to the inner surface of the aorta and of the aorto-ventricular junction (Figure 46.a), while the ends of the AR are allowed only for radial expansion/contraction (Figure 46.b). From the pressurized configuration (Ω_{82}), aortic wall nodal displacements (u_{82}) and Cauchy stresses (σ_{82}) are extracted; if the magnitude of the peak nodal displacement is lower than the in-plane resolution of medical images (Im_{res}), the final pre-stress field is set equal to σ_{82}, otherwise the initial stresses are set to σ_{82} and the inflation simulation is iterated. X and x indicate the initial and current configuration of the model, respectively.

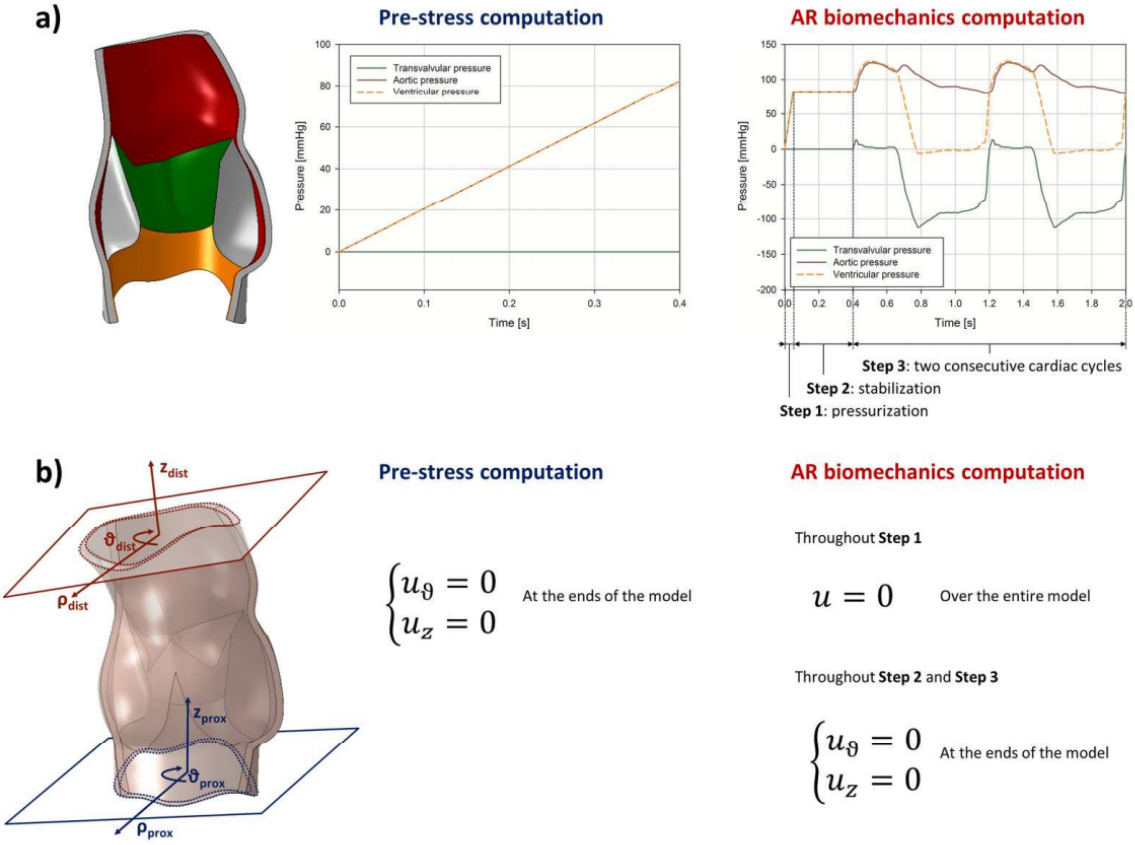

Figure 46: Boundary conditions applied in the simulations. a) *Loading boundary conditions - Left hand panel*: the inner surface of the aorta, the inner surface of the aorto-ventricular junction, and the ventricular surface of AV leaflets are depicted in red, orange, and green, respectively. The same color code is adopted to plot the aortic, ventricular, and trans-valvular pressure loads applied on the three surfaces. *Mid panel*: loads applied when pressurizing the AR to compute pre-stresses are depicted. The inner surface of the aorta and of the aorto-ventricular junction are both loaded with a pressure linearly increasing to 82 mmHg, while no pressure is applied on the ventricular surface of AV leaflets. *Right hand panel*: loads applied when simulating AR biomechanics are depicted for the three steps composing the simulation. In the first step, which lasts 0.05 s, the inner surface of the aorta and of the aorto-ventricular junction are both loaded with a pressure linearly increasing to 82 mmHg, while no pressure is applied on the ventricular surface of AV leaflets. In the second step, which lasts 0.35 s, the loading conditions reached at the end of step 1 are kept constant. In the third step, two consecutive cardiac cycles are simulated and consistent time-dependent aortic, ventricular and trans-valvular pressures are applied to the corresponding surfaces. b) *Kinematic boundary conditions - Left hand panel*: the two local cylindrical reference frames (ρ, θ, z) defined at the proximal (blue) and distal (red) end of the AR model are depicted. In each reference frame, the origin is the center of mass of the nodes at the corresponding end of the model, and the z-axis being the normal to their least square fit plane. *Mid panel*: when pressurizing the AR to compute pre-stresses, the nodes at the two ends of the AR model cannot translate tangentially ($u_\theta = 0$) nor axially ($u_z = 0$). *Right hand panel*: when simulating AR biomechanics, in the first step every node of the model is prevented from translations ($u = 0$). In the second and third step of the simulation, only the nodes at the two ends of the AR model are constrained, namely by preventing from tangential and axial motion ($u_\theta = u_z = 0$).

6 Results

6.1 Geometry reconstruction

As described in the previous chapter, we applied our modeling approach to cMRI data acquired on three healthy volunteers. For each subject, three different models of the AR were generated based on the manual tracing performed in the first systolic frame: SH model, 3D-HT model, and 3D-MT model. In each model, the reconstruction of leaflet geometry was carried out exploiting the smoothing procedure detailed in section 5.3.1.

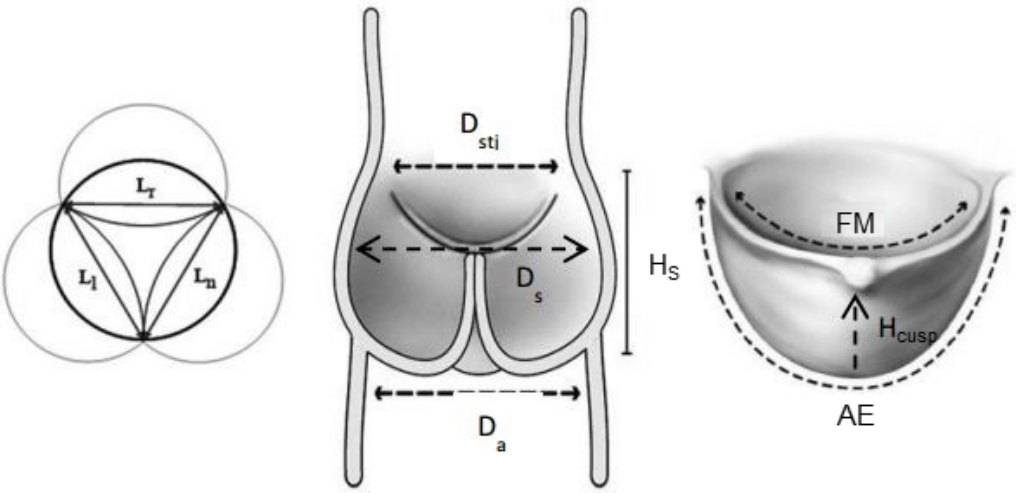

Figure 47: Schematic representation of the parameters evaluated in each model. *Left hand panel*: trasversal section of AR in which the right(L_r), left(L_l) and non-coronary(L_n) inter-commissural distance are shown. *Central panel*: longitudinal section of AR in which the Valsalva sinus height (H_s), the aortic annular diameter (D_a), aortic sinotubular diameter (D_{stj}) and aortic diameter at mid height of Valsalva sinuses (D_s) are shown. *Right hand panel*: schematic representation of AV cusp with its primary geometrical parameters, its height(H_{cusp}), its free margin (FE) and its attachment edge (AE).

Prior to any biomechanical analysis, the inter-subject variability of the geometrical features of the reconstructed ARs was quantified by measuring the following dimensions on each model: the annulus diameter (D_a), the STJ diameter(D_{stj}), the maximum diameter of the sinuses (D_s), the right, left and non-coronary inter-commmisural distance (L_{IC}), and the sinus height (H_S), i.e. the distance between the annulus and the STJ level. Further parameters were measured on the leaflets: the surface area of each cusps

(A), the free margin length (L_{FM}), the attachment edge length (L_{AE}) and the height of the cusps (H_{cusp}), i.e. the distance between the nadir and the nodulus of Arantius (Figure 47, Table 10). These measurements were inherently repeatable over the three models generated for a single AR: these differed by the approach to the generation of the leaflet mesh, which did not impact on the aortic wall dimensions nor on the leaflet extent.

	AR1	**AR2**	**AR3**
D_a **[mm]**	28.0	27.3	28.9
D_s **[mm]**	33.5	31.6	34.6
D_{stj} **[mm]**	27.4	23.9	32.1

	L	**R**	**NC**	**L**	**R**	**NC**	**L**	**R**	**NC**
L_{IC} **[mm]**	21.1	25.8	23.7	22.4	17.0	21.6	26.1	30.6	25.8
H_S **[mm]**	26.1	27.6	27.1	28.6	26.5	24.6	21.7	27.1	23.8
A_{cusp} **[mm]**	511.59	655.70	577.60	511.16	433.21	644.54	615.79	622.19	590.98
L_{FM} **[mm]**	23.43	28.69	26.59	24.19	21.31	25.38	28.24	32.60	29.36
L_{AE} **[mm]**	67.73	73.71	68.95	65.76	63.31	74.99	70.52	69.08	69.50
H_{cusp} **[mm]**	22.34	23.21	22,45	20.05	21.47	23.20	22.46	20.13	20.55

Table 10: Characteristic dimensions of each reconstructed AR anatomy. Top: dimensions referred to the entire aortic lumen; D_a = aortic annular diameter, D_s = aortic diameter at mid height of Valsalva sinuses, D_{STJ} = sinotubular diameter. Bottom: dimensions measured on each leaflet-sinus unit (L = left; R = right; NC = non-coronary): L_{IC} = inter-commissural distance, H_S = Valsalva sinus height, A_{cusp} = cusp area, L_{FM} = free margin length, L_{AE} = length of basal attachment edge, H_{cusp} = cusp height.

As reported in Table 10, model AR3 had the largest diameter at the annulus, STJ and sinus level, whereas model AR2 was characterized by the smallest value of these parameters. Concerning the leaflets, the ratio between the L_{FM} and the L_{AE} was always lower than one, consistently with the literature [21]. However, differences between the three leaflets changed markedly from model to model. In model AR1, the left-coronary leaflet was the smallest leaflet, characterized by the smallest value in every geometrical parameter and by a cusp area that was lower by about 20% and 11% as compared to the right and non-coronary leaflet, respectively. with respect to RC; 11% with respect to NC). In model AR2, the right-coronary leaflet was the smallest leaflet, despite not being characterized by the lowest cusp height; its cusp area was lower by about 15% and 32% as compared to the left and non-coronary leaflet, respectively. In model AR3,

instead, no notable differences were found among the three cusp areas.

Hence, despite the very low numerosity of the considered cohort of subjects, a satisfactory representation of the anatomical inter-subject variability characterizing the physiological population was obtained. However, it may be worth stressing two aspects that may have impacted on the leaflet dimensions and hence on the different levels of asymmetry in the three models. First, leaflets are difficult to trace, because they are not well visible in each image plane. Second, a smoothing procedure was applied when reconstructing leaflets geometry, possibly leading to an underestimation of leaflet extent.

The final geometry of the three models generated for each subject are shown in Figures 48, 49, 50.

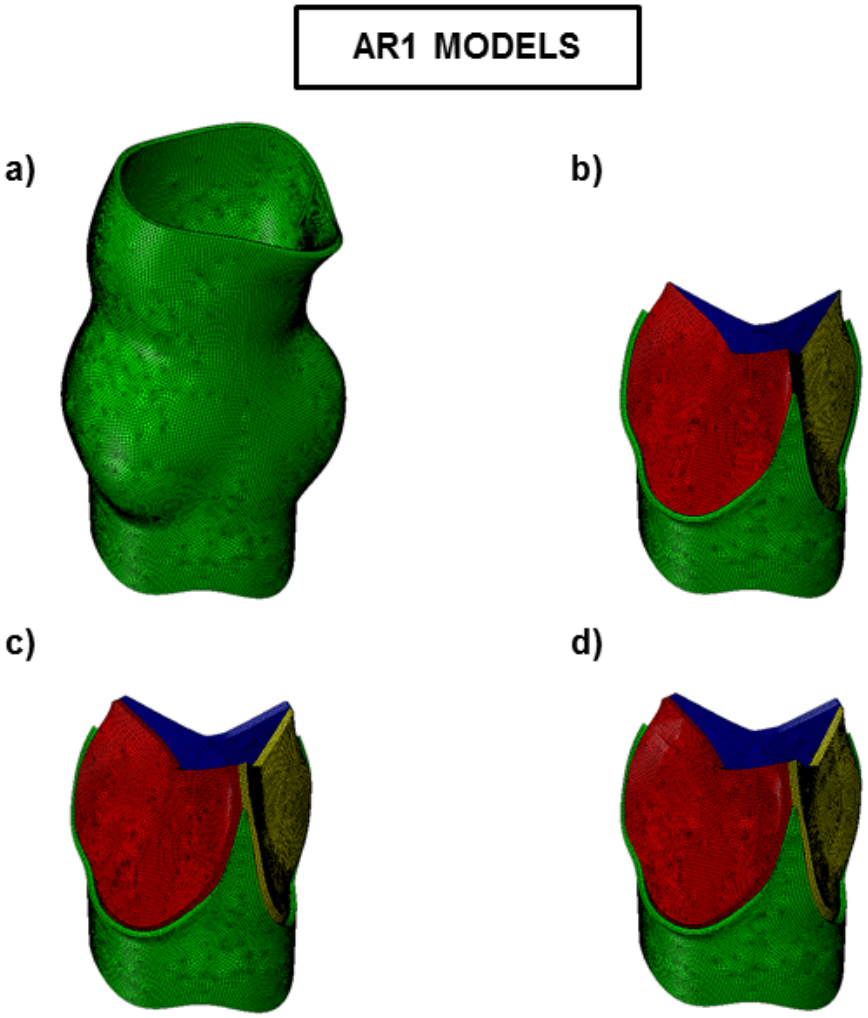

Figure 48: Geometry reconstruction of subject AR1 starting from cMRI. a) aortic root wall (equal for all models). b) leaflets' structure in the model SH. c) leaflets' structure in the model 3D-HT. d) leaflets' structure in the model 3D-MT.

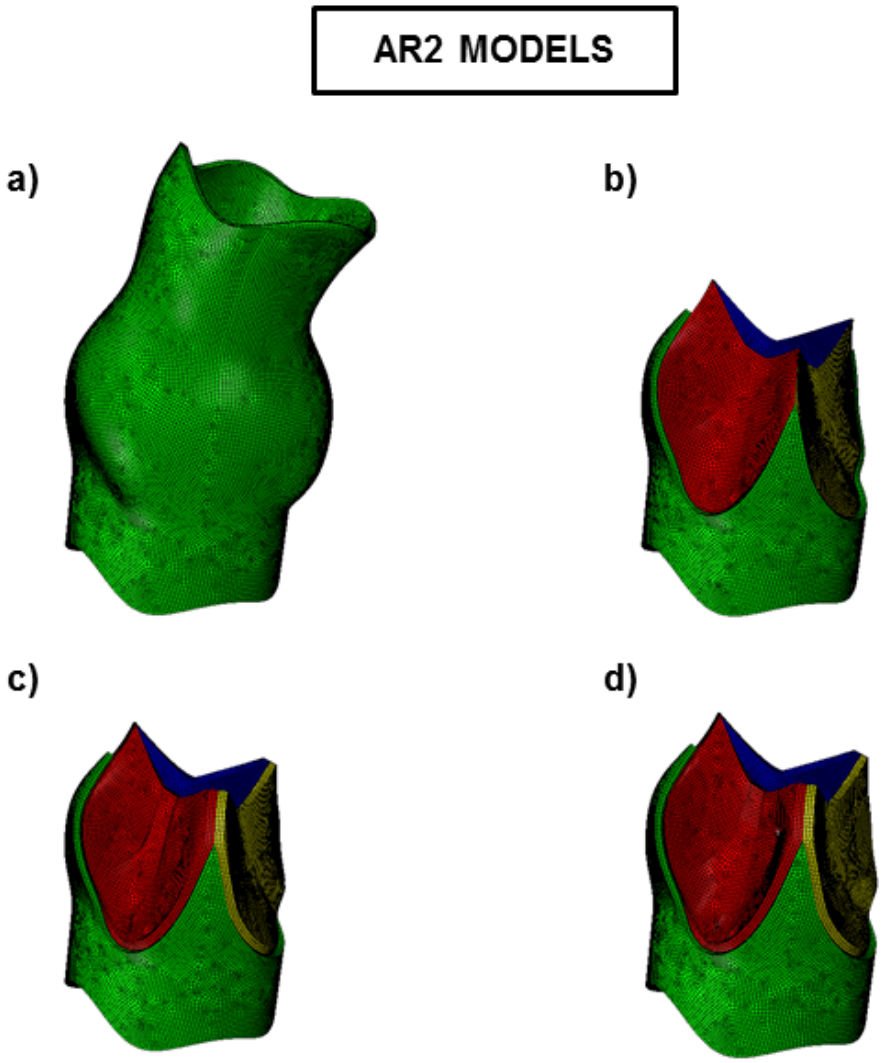

Figure 49: Geometry reconstruction of subject AR2 starting from cMRI. a) aortic root wall (equal for all models). b) leaflets' structure in the model SH. c) leaflets' structure in the model 3D-HT. d) leaflets' structure in the model 3D-MT.

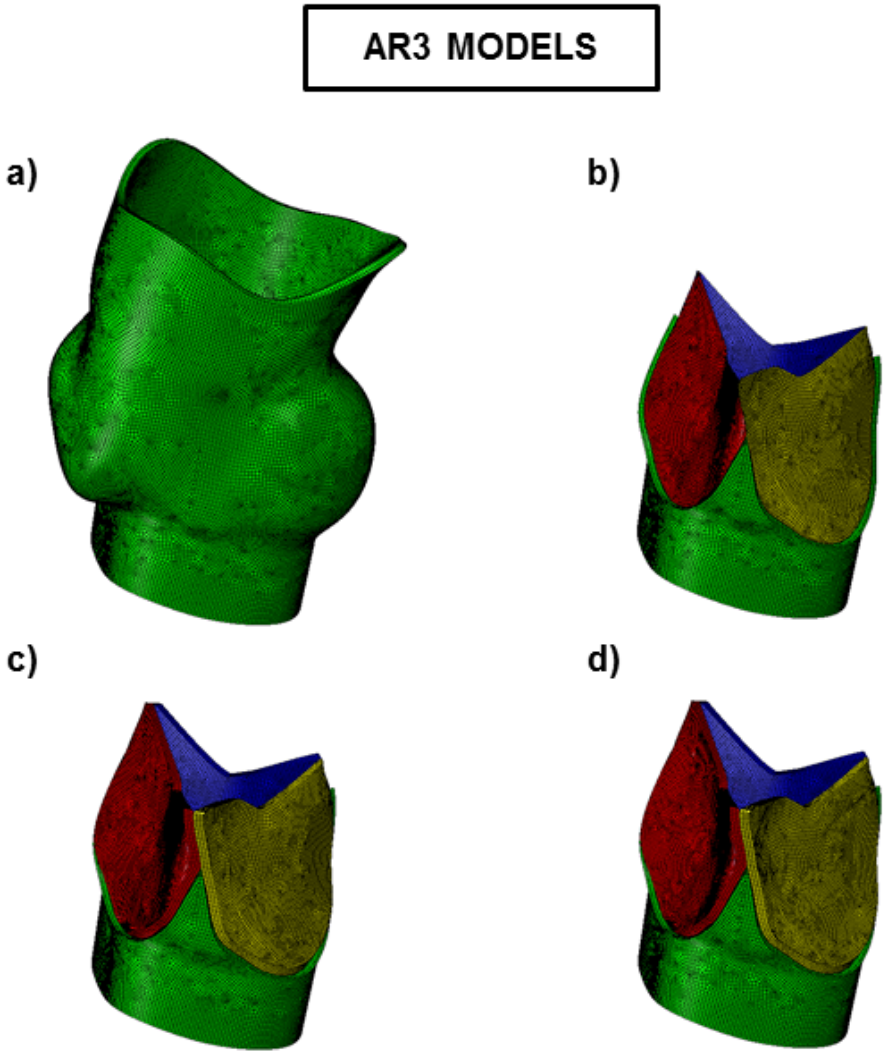

Figure 50: Geometry reconstruction of subject AR3 starting from cMRI. a) aortic root wall (equal for all models). b) leaflets' structure in the model SH. c) leaflets' structure in the model 3D-HT. d) leaflets' structure in the model 3D-MT.

6.2 Energy balances

Before the analysis of the results, two energy balaces were computed for each simulations in order to assure the consistency of the numerical data obtained. In particular two parameters were evaluated throughout the second cardiac cycle:

$$\omega_1 = \frac{K}{E_i}, \quad \omega_2 = \frac{E_a}{E_i} \tag{24}$$

where K is the *kinetic energy* of the model, E_i the *total internal energy* and E_a the *artificial strain energy*, i.e. the energy spent by the solver to avoid zero-energy deformations (e.g hourglass effect). Two threshold were defined to evaluate the reliability of

the results: one for ω_1, equal to 0.1, and one for for ω_2, equal to 0.05, as suggested from solver documentation [1]. The charts are below reported only for the three simulations on the AR1 subject geometry (Figure 51), whereas the charts of all other simulations can be found in Appendix B.

The SH models showed more irregular curves compared to the corresponding 3D-HT and 3D-MT models, and, in particular, the chart of ω_2 was higher than the threshold. The latter was due to the hourglass effect on the leaflets free margin of the SH model, where the solver spent a lot of artificial strain energy E_a; as a portion of energy was used for this reason, less energy could be spent to generate stresses and deformations, leading to non-accurate stress-strain state. In solid elements models instead, both ω_1 and ω_2 charts were regular and below the threshold; the only exception was related to the two kinetic energy peaks at opening and closing cardiac cycle frames.

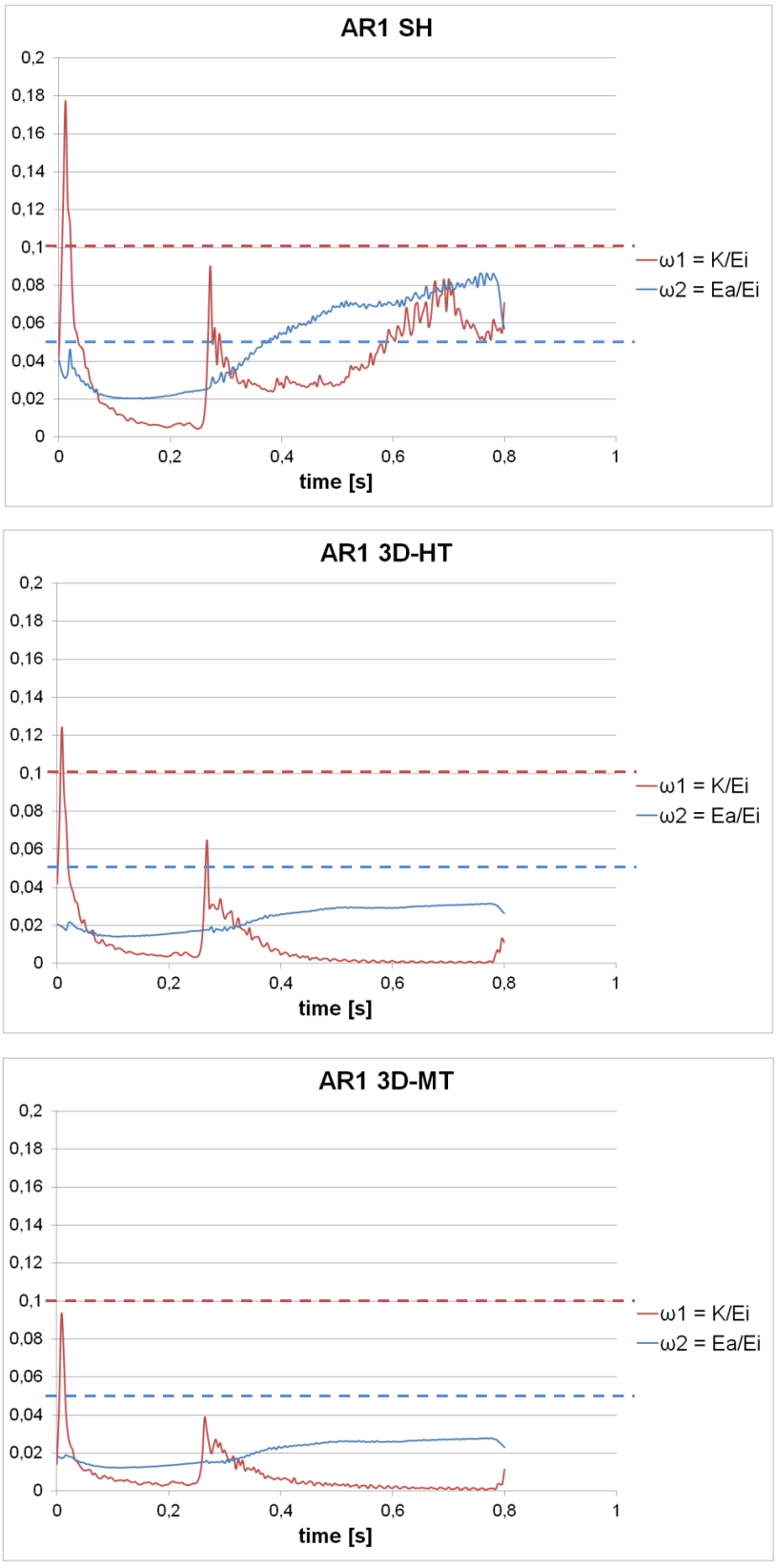

Figure 51: Energy balances for subject AR1. *Red* line: ω_1. *Blue* line: ω_2.

6.3 Biomechanical analysis performed using FEM simulations

As described in the previous chapter, for each model typology (SH, 3D-HT, 3D-MT) a simulation sequence was performed, which consisted in the iterative computation of aortic wall pre-stresses and in the subsequent simulation of the structural response of the pre-stressed AR throughout two consecutive cardiac cycles, starting from the first systolic frame yielded by cMRI.

Table 11 summarizes the time required by the different phases of our simulation process; the time-expense of simulations is referred to a workstation with 16 CPUs. It is worth noting that the output of the pre-stress computation (phase 1a) are manually integrated into the input file for the simulation of the cardiac cycles (phases 2a-b-c); this manual operation requires approximately 15 minutes. As already mentioned, pre-stress computation was an iterative process: for model AR1 two iterations were needed, for models AR2 and AR3 three iterations were needed.

		1a	*1b*	*2a*	*2b*	*2c*
		P-S [h]	**OP [min]**	**INIT [h]**	**CC #1 [h]**	**CC #2 [h]**
AR1	SH	6.5	∼15	6.9	14	13.5
	3D-HT	6	∼15	6.1	13	12
	3D-MT	6	∼15	6.1	13	12
AR2	SH	6	∼15	6.1	14	13
	3D-HT	5.7	∼15	6	13	12
	3D-MT	5.7	∼15	6	14	13
AR3	SH	7	∼15	7.1	17	16
	3D-HT	6.9	∼15	6.9	16	15
	3D-MT	6.9	∼15	6.9	16	15

Table 11: Time required by the different phases of our simulation process. The computation of AR pre-stresses required two iterations of phases 1a and 1b for model AR1, and three iterations for models AR2 and AR3. P-S = pre-stress evaluation step. OP = operator-dependent step. INIT: initial phase in which the pre-stressed AR configuration is reached. CC = cardiac cycle step.

Results were post-processed with reference to the second simulated cardiac cycle, in order to account for the transient condition characterizing the initial time-point of the phenomenon and for the associated inertial effects [12]. For each quantity of interest, results from SH models and 3D-HT models were compared in order to quantify the

effects of the use of solid elements in the discretization of leaflet geometry. Also, results from 3D-HT models and 3D-MT models were compared to assess the effects of different leaflet thickness distributions.

6.3.1 Aortic valve time-dependent configuration

AV configuration was assessed at two key time-points through the cardiac cycle: at peak systolic trans-valvular pressure ($t = 20\,\text{ms}$), and at peak diastolic-transvalvular pressure ($t = 380\,\text{ms}$).

At peak systole, the leaflet configuration was quantified in terms of orifice area (Figure 52). In a consistent way, for every simulated AR 3D-HT and 3D-MT models smaller orifice areas were computed as compared to the corresponding SH models: in models AR1, AR2, and AR3 such decrease was by 13%, 17%, and 10%, respectively.

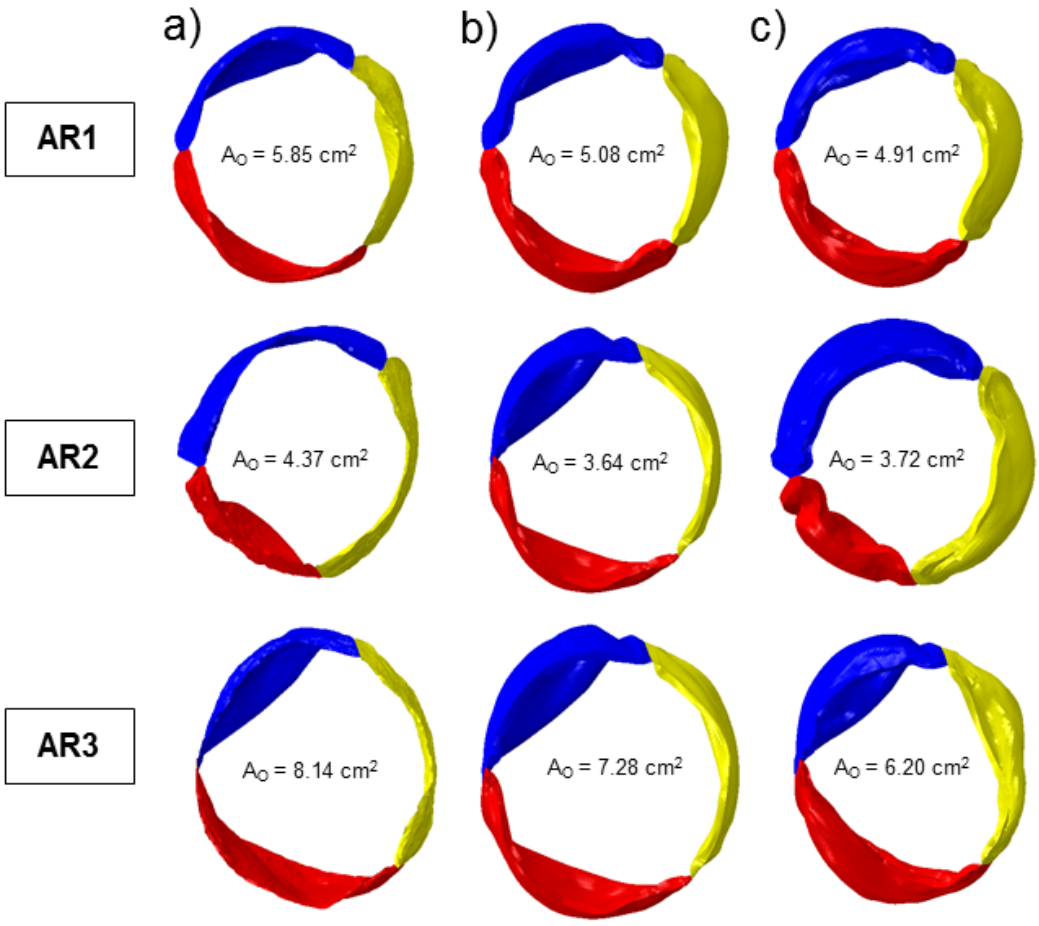

Figure 52: Opened AV configurations and the corresponding orifice area (A_O) at the systolic peak ($t = 20\,\text{ms}$). a) SH models. b) 3D-HT models. c) 3D-MT models.

This result is likely due to the different behavior of the leaflets at their line of insertion. When shell elements were used to discretize leaflets' geometry, the leaflet-aortic wall connection behaved approximately as a spherical joint, and leaflets were allowed for local wide rotations (Figure 53 , *left hand panel*). When solid elements were used to discretize leaflets' geometry, the leaflet-aortic wall connection behaved as a deformable encastre, preventing from free rotations of the leaflet section (Figure 53 , *right hand panel*). This effect reflected into a less pronounced outward motion of the leaflet during the opening phase.

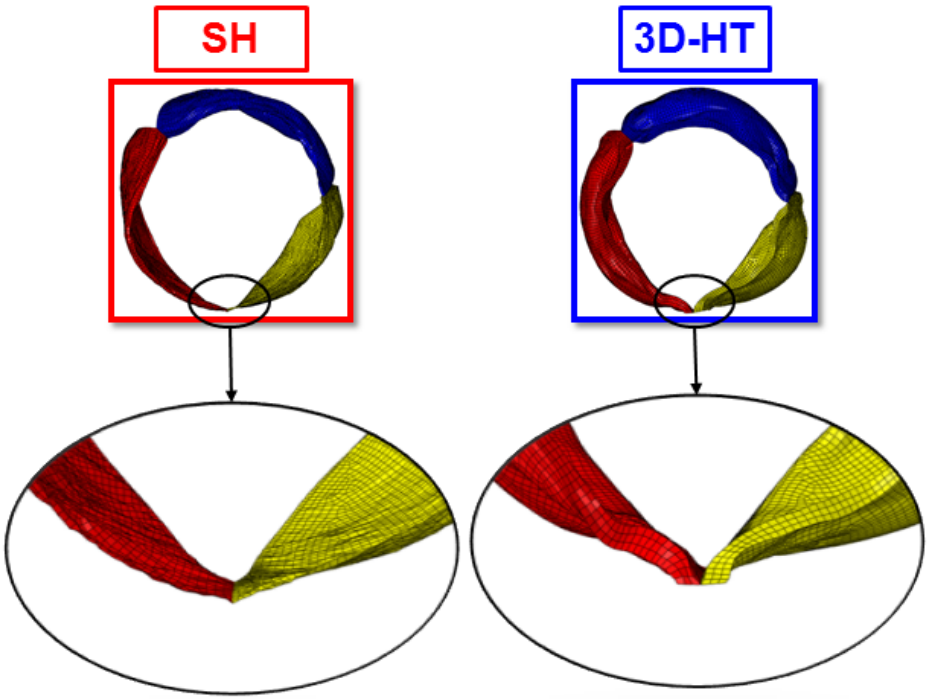

Figure 53: The different deformed configuration of the commissural region of the leaflets at peak systole when using shell elements (left panel) and solid elements with homogeneous thickness (right panel) to discretize the leaflets is depicted for model AR1. In particular, the junction between the aortic wall, the left-coronary leaflet (LC, yellow), and the right-coronary leaflet (RC, red) is reported.

At peak diastole, leaflet configuration was analyzed qualitatively (Figure 54) and quantitatively by measuring the coaptation height and the degree of prolapse of the leaflets. The former was defined as the axial distance in mm between the nodulus of Arantius and the annular plane. The latter was defined as the distance in mm, oriented towards the ventricle, between the lower point in the leaflet and the corresponding nadir (Table 12).

AR1

	SH model			*3D-HT model*			*3D-MT model*		
	LC	RC	NC	LC	RC	NC	LC	RC	NC
Coaptation height [mm]	19.81	17.85	17.58	19.69	18.40	18.53	20.21	17.66	17.95
Prolapse [mm]	1.67	3.77	1.51	0.50	1.65	1.35	0.66	2.07	2.11

AR2

	SH model			*3D-HT model*			*3D-MT model*		
	LC	RC	NC	LC	RC	NC	LC	RC	NC
Coaptation height [mm]	18.52	20.18	20.20	16.79	21.07	17.85	16.62	20.89	18.15
Prolapse [mm]	2.59	1.44	2.64	1.12	-0.64	0.75	1.65	-0.57	1.55

AR3

	SH model			*3D-HT model*			*3D-MT model*		
	LC	RC	NC	LC	RC	NC	LC	RC	NC
Coaptation height [mm]	22.03	17.27	17.70	16.89	18.58	18.87	15.85	16.23	17.39
Prolapse [mm]	2.23	1.08	1.84	0.86	1.53	1.12	2.44	2.45	1.84

Table 12: Coaptation height and degree of prolapse values computed for all models at peak diastole.

As regards the coaptation height, no systematic differences were observed between models using different types of element to discretize the leaflets' geometry. The main evidence was that in all AR models and in all models types coaptation height values were higher than the ones provided by previously published computational studies [12] and were all well above the 9 mm upper threshold characterizing almost all patients suffering from moderate or severe aortic insufficiency according to ultrasound analyses [9]. Of note, the high values of the coaptation height parameter may have been influenced by the smoothing procedure adopted in the 3D reconstruction of leaflets' geometry. Indeed, that procedure was aimed also at avoid unrealistically steep profiles of the leaflet free margin and, to this specific aim, slightly elevates the central portion of the free margin.

As regards the degree of prolapse, a notable difference was observed between the models using different elements to discretize the leaflets' geometry. In general, SH models were characterized by a more pronounced degree of prolapse, i.e. the belly region of the leaflets tended to invade the volume within the aorto-ventricular junction. Again,

this effect was likely due to the connection between the leaflet mesh and the aortic wall mesh, where nodes were allowed for finite rotations (Figure 54). This effect was markedly reduced in all 3D-HT models, owing to the connection between leaflet and aortic wall meshes, which in these models acts like a deformable encastre (Figure 54). Conversely, in 3D-MT models, even though these share with 3D-HT models the type of leaflet-wall connection, the reduction in level of prolapse was obtained only in model AR1. In models AR2 and AR3, instead, the belly region of the leaflets tended to bulge towards the ventricle, leading to a degree of prolapse that closely matched the one computed with SH models. This effects was related to the low thickness set for the belly region in 3D-MT models (Figure 54).

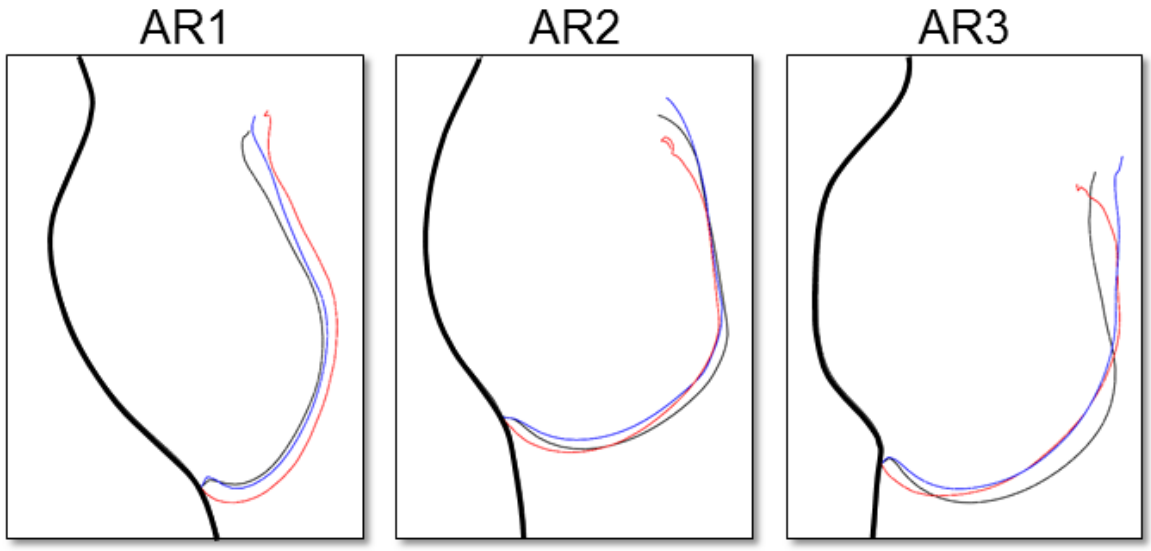

Figure 54: Longitudinal section of the left-coronary leaflet at the diastolic peak ($t = 380\,\text{ms}$). *Black* line: sinus side and the LC leaflet of the model 3D-MT with a modulated thickness. *Blue* line: the LC leafelt of the model 3D-HT with an homogenous thickness. *Red* line: the LC leafelt of the model SH with an homogenous virtual thickness.

6.3.2 Mechanical response of the aortic valve

The mechanical response of the AV during the cardiac cycle was evaluated through the analysis of the stress-strain state. In particular, we focused the attention on the stress and strain patterns of the belly throughout the cardiac cycle, due to the fact that it is the most stressed region of the cusp, as reported from literature [12] [16] [10]. To this aim, a $4\,\text{mm} \times 4\,\text{mm}$ patch in the central portion of the belly was considered; stress and strain values were assessed for all elements within the patch, and their values were

avereged over the patch (Figure 55, 56, 57).

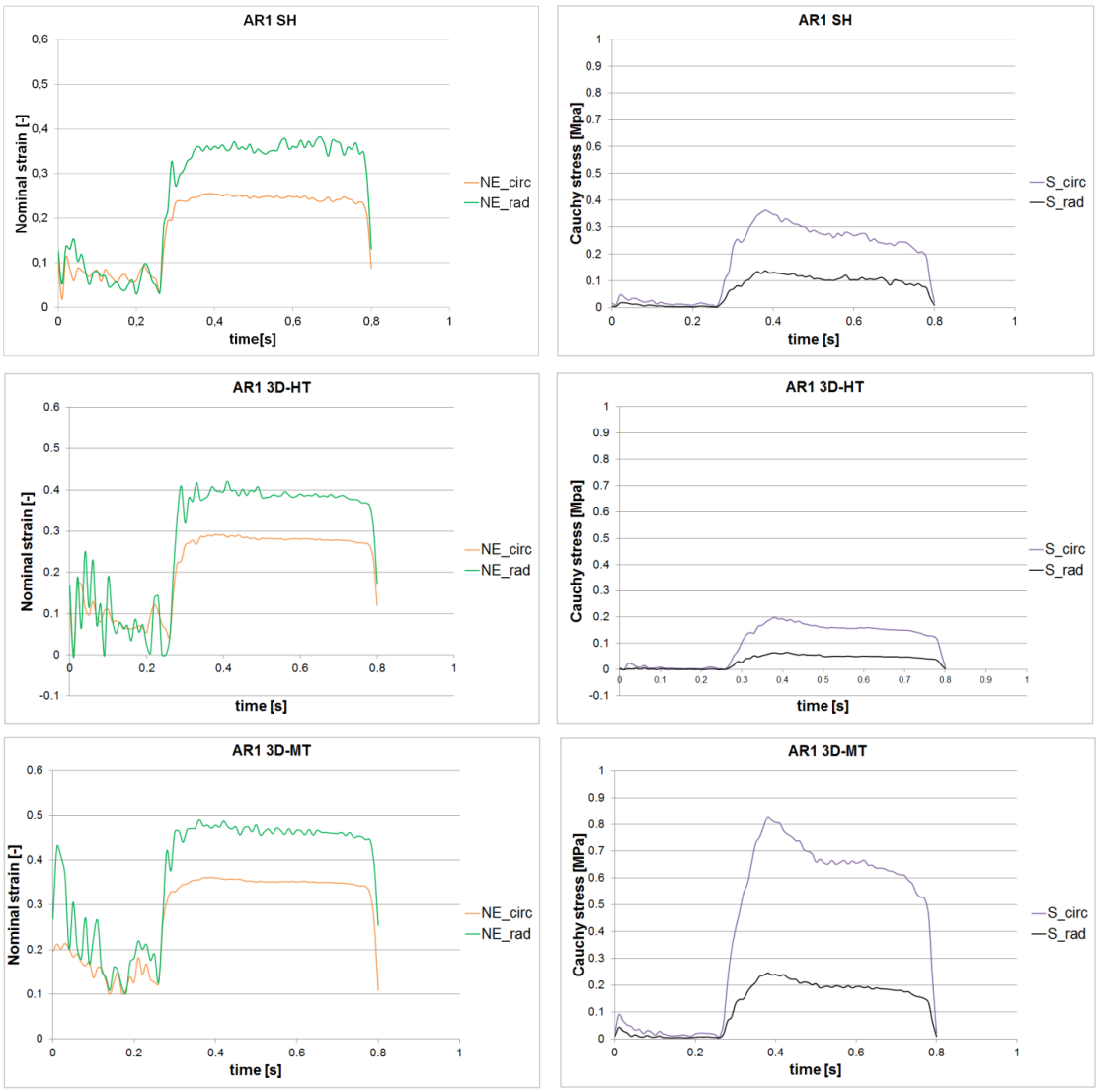

Figure 55: subject AR1. *Left hand panel*: nominal strain in the belly region at the diastolic peak ($t = 380\,\text{ms}$). *Right hand panel*: Cauchy stress in the belly region at the diastolic peak.

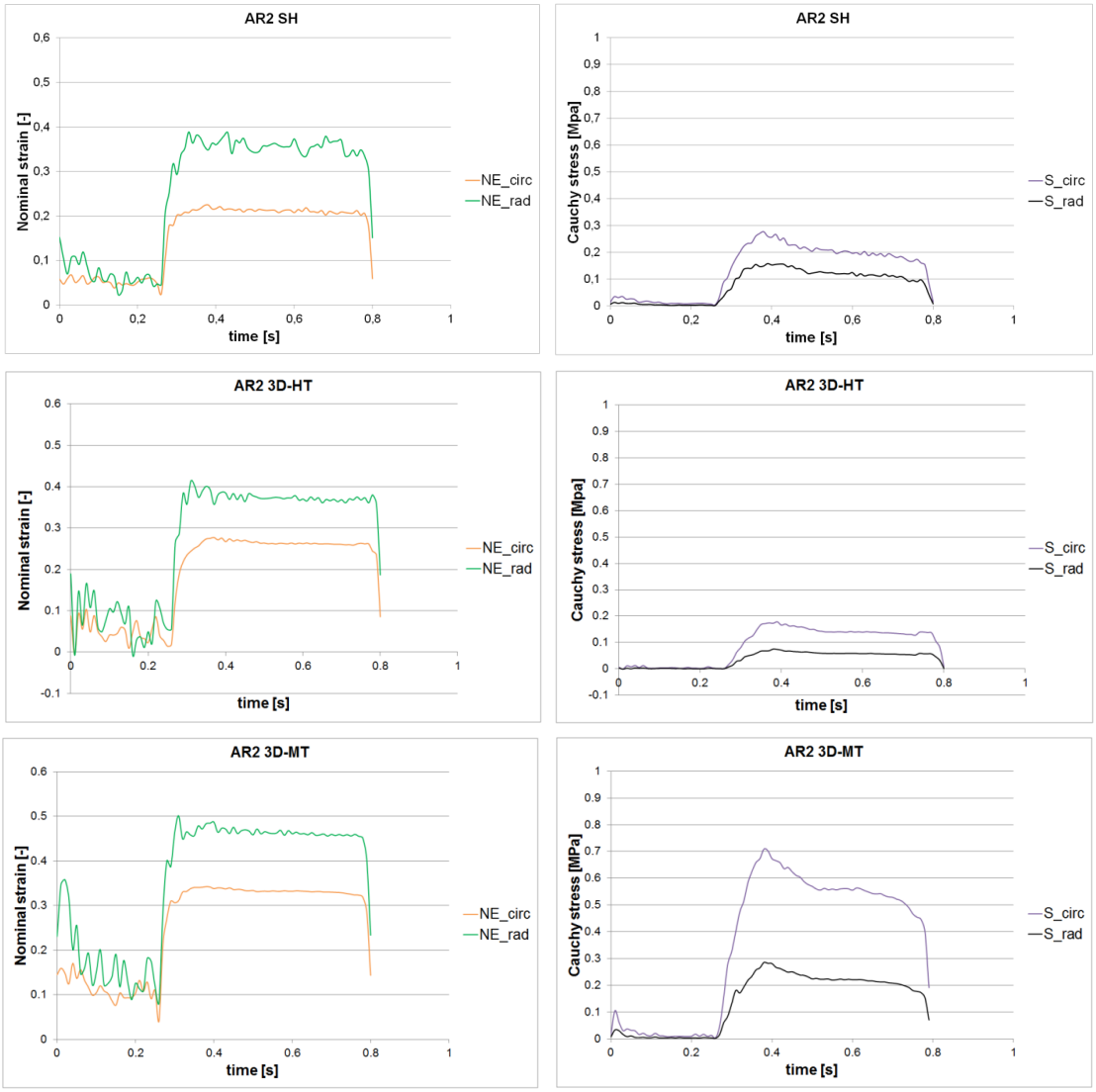

Figure 56: subject AR2. *Left hand panel*: nominal strain in the belly region at the diastolic peak ($t = 380\,\text{ms}$). *Right hand panel*: Cauchy stress in the belly region at the diastolic peak.

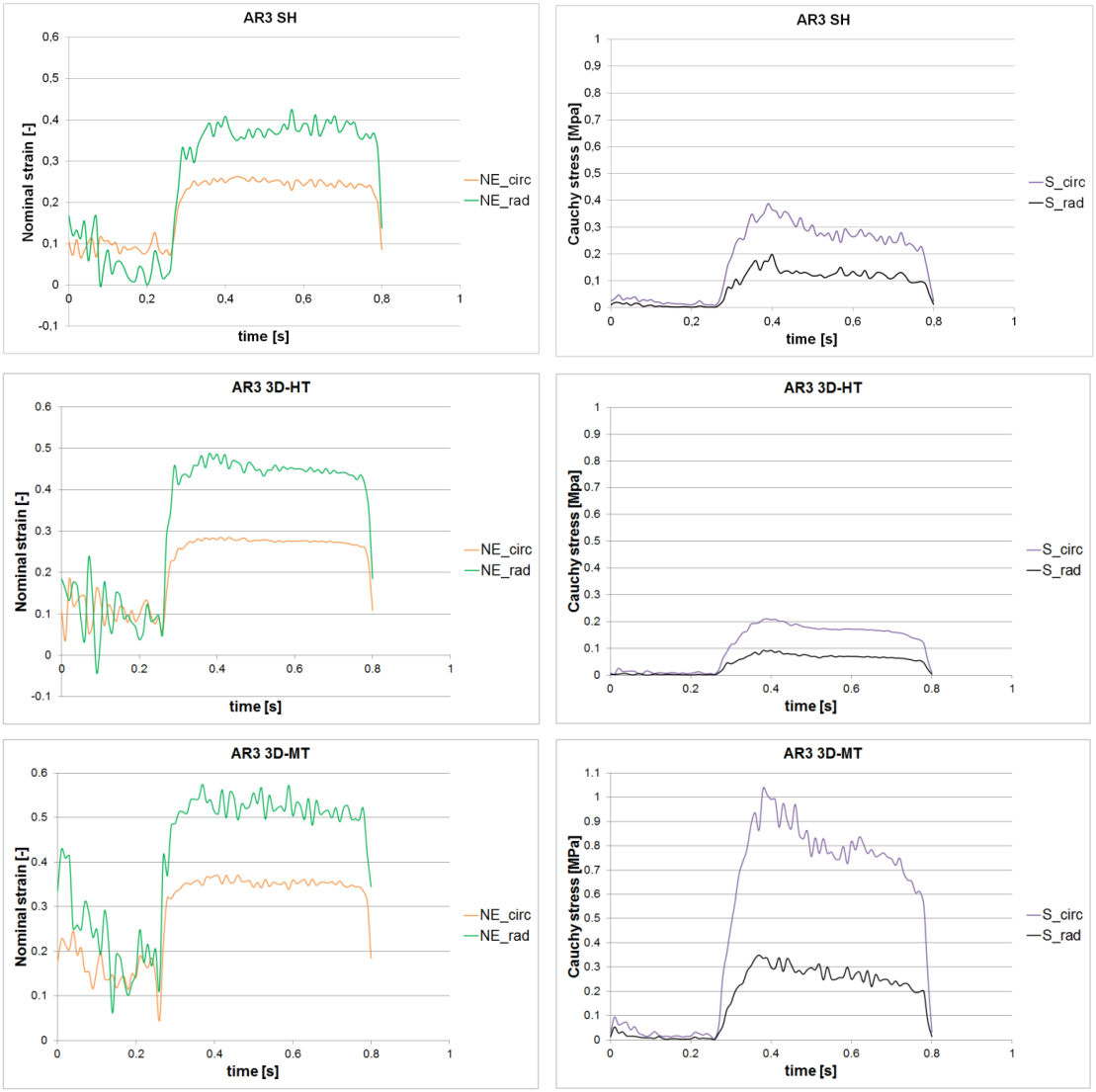

Figure 57: subject AR3. *Left hand panel*: nominal strain in the belly region at the diastolic peak ($t = 380\,\text{ms}$). *Right hand panel*: Cauchy stress in the belly region at the diastolic peak.

The first important result was the difference between the two characteristic directions of the models, circumferential and radial, highlighting the anisotropy of the aortic valve tissue. During the closing valve transient, the deformations of the cusps rapidly increase to reach a plateau during the diastole phase. Despite the magnitude, this behavior could be observed in all models, coehrently with the data reported in the work of Thubrikar [46]. In addition, while in the radial direction the deformation magnitudes were consistent with literature [46] [12], the ones in circumferential direction overestimated the *in vivo* values from more than 30%. Regarding the stress patterns, we could see a rapid increase during the closing valve transient, with the stress maximum

values at the diastolic peak. For the same reasons causing the high degree of prolapse, i.e. the thinned belly region, the stress in the 3D-MT models showed very high values compared to the corresponding SH and 3D-HT models.

In order to deeply investigate the mechanical response of the aortic valve, we focused our attention on the diastolic peak ($t = 380\,\text{ms}$), because it represents the moment within the cardiac cycle in which the belly region is more stressed [12]. In particular, two kind of results were analized: the maximum principal stress and the circumferential and radial stress (Table 13), and the max principal stress distribution along the leaflet surface viewed from the ventricular side (Figure 58).

AR1

	SH model			*3D-HT model*			*3D-MT model*		
	LC	RC	NC	LC	RC	NC	LC	RC	NC
Max principal stress [MPa]	0.338	0.566	0.317	0.163	0.254	0.196	0.681	1.028	0.861
σ_{circ} **[MPa]**	0.312	0.489	0.287	0.156	0.249	0.192	0.636	1.008	0.842
σ_{rad} **[MPa]**	0.088	0.220	0.103	0.037	0.102	0.056	0.136	0.375	0.225

AR2

	SH model			*3D-HT model*			*3D-MT model*		
	LC	RC	NC	LC	RC	NC	LC	RC	NC
Max principal stress [MPa]	0.418	0.116	0.462	0.197	0.100	0.231	0.801	0.390	0.946
σ_{circ} **[MPa]**	0.367	0.109	0.356	0.192	0.099	0.228	0.798	0.387	0.940
σ_{rad} **[MPa]**	0.155	0.023	0.269	0.083	0.013	0.131	0.405	0.050	0.402

AR3

	SH model			*3D-HT model*			*3D-MT model*		
	LC	RC	NC	LC	RC	NC	LC	RC	NC
Max principal stress [MPa]	0.390	0.461	0.390	0.204	0.233	0.193	0.977	1.125	1.042
σ_{circ} **[MPa]**	0.300	0.405	0.353	0.201	0.228	0.192	0.976	1.095	1.041
σ_{rad} **[MPa]**	0.216	0.165	0.136	0.123	0.087	0.066	0.427	0.312	0.270

Table 13: Max principal stress, circumferential stress (σ_{circ}) and radial stress (σ_{rad}) for the three leaflets (LC, RC, NC) of each model at diastolic peak ($t = 380\,\text{ms}$).

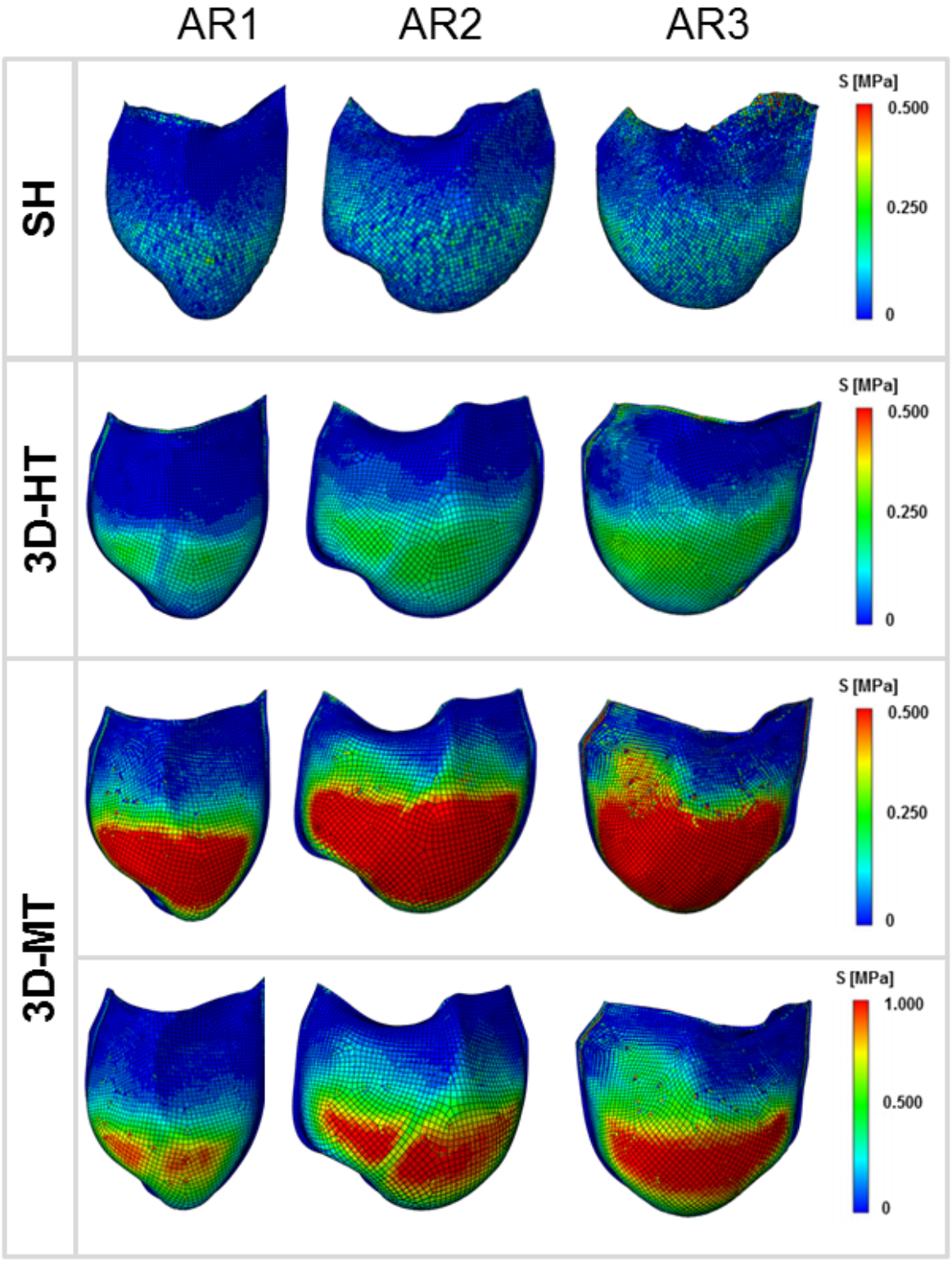

Figure 58: Max principal stress computed at the diastolic peak ($t = 380\,\text{ms}$) for the AR1 subject (*left column*), AR2 subject (*central column*), AR3 subject (*right column*). *First line*: max principal stress distribution on the mid surface of the three SH models. *Second line*: max principal stress distribution on the mid solid level of the three 3D-HT models. *Third line*: max principal stress distribution on the mid solid level of the three 3D-MT models. *Fourth line*: max principal stress distribution on the mid solid level of the three 3D-MT models in a different stress scale to better highlight the stress distribution in these models.

The differences in the element formulation between shell and solid models were evident (Figure 58): in shell leaflets, indeed, the stress shows a patchy distribution, and a clear separation between the belly region and the coaptation area based on the stress pattern could not be detected. Conversely, in the solid 3D-HT and 3D-MT models the stress distribution was much more regular and a clear separation between these two regions was evident.

Calculated stress values (Table 13) proved the strong impact of the thickness modulation procedure, described in section 5.3.5, on the 3D-MT models; in particular, max principal, radial and circumferential stresses were notably increased in the thinned belly region. For example, the circumferential stress values averaged over the three leaflets for the 3D-MT models are more than 4-fold as compared to the corresponding values for 3D-HT models, and more than 2-fold as compared to the corresponding values for SH models (Table 14).

	AR1			**AR2**			**AR3**		
	SH	3D-HT	3D-MT	SH	3D-HT	3D-MT	SH	3D-HT	3D-MT
$\overline{\sigma}_{max\_principal}$ **[MPa]**	0.407	0.204	0.857	0.332	0.176	0.712	0.414	0.210	1.048
$\overline{\sigma}_{circ}$ **[MPa]**	0.362	0.200	0.829	0.277	0.173	0.709	0.353	0.208	1.037
$\overline{\sigma}_{rad}$ **[MPa]**	0.137	0.065	0.245	0.149	0.076	0.286	0.172	0.092	0.336

Table 14: Average max principal, circumferential and radial stress over the three leaflets (LC, RC and NC) for all subjects. $\overline{\sigma}_{max\_principal}$ = averaged max principal stress. $\overline{\sigma}_{circ}$ = averaged circumferential stress. $\overline{\sigma}_{rad}$ = averaged radial stress.

As one of the primary aims of this work was the investigation of the stress distribution across the leaflet thickenss, the circumferential and radial stress were evaluated across the leaflet surface in all models. The measures were performed at the diastolic peak ($t = 380\,\text{ms}$) in three different points (A, B, C) of the left-coronary leaflet (Figure 59).

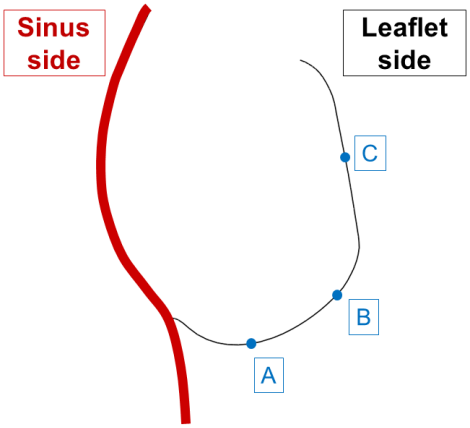

Figure 59: Schematic longitudinal section representing the locations (*green* points) across the leaflet surface in which the max principal stress was evaluated.

In this analysis a particular aspect has to be accounted in regarding how the stress values are computed through the leaflet thickness. For each location the stress value were available in three integration point across the leaflet thickness for all models: for the SH models this three points refer to three shell layers (virtual ventricular layer, mid layer, virtual aortic layer), while for the 3D-HT and 3D-MT models the integration points lay in three different solid elements layers (solid ventricular layer, solid mid layer, solid aortic layer). Due to the different formulation between shell and solid elements, the stress values at the integration points are computed in a completely different way, leading to different levels of precision (Table 15).

Location		**AR1** models: σ_{circ}			**AR2** models: σ_{circ}			**AR3** models: σ_{circ}		
		SH	3D-HT	3D-MT	SH	3D-HT	3D-MT	SH	3D-HT	3D-MT
A	*V layer*	0.252	0.144	0.315	0.682	0.096	0.183	0.018	0.209	0.469
	mid layer	0.045	0.066	0.241	0.036	0.056	0.127	0.069	0.131	0.477
	A layer	0.109	0.029	0.183	0.539	0.028	0.087	0.709	0.074	0.450
B	*V layer*	0.526	0.229	0.770	0.480	0.259	0.851	1.054	0.321	1.108
	mid layer	0.096	0.170	0.640	0.078	0.154	0.758	0.073	0.237	0.995
	A layer	0.169	0.135	0.548	0.351	0.091	0.682	0.497	0.169	0.909
C	*V layer*	0.022	0.009	0.051	0.025	0.069	0.141	0.099	0.124	0.270
	mid layer	0.016	0.021	0.071	0.025	0.060	0.137	0.031	0.048	0.202
	A layer	0.038	0.046	0.106	0.140	0.054	0.218	0.053	0.036	0.154

Location		**AR1** models: σ_{rad}			**AR2** models: σ_{rad}			**AR3** models: σ_{rad}		
		SH	3D-HT	3D-MT	SH	3D-HT	3D-MT	SH	3D-HT	3D-MT
A	*V layer*	0.133	0.074	0.149	0.279	0.129	0.222	0.018	0.175	0.476
	mid layer	0.026	0.040	0.117	0.034	0.077	0.153	0.042	0.114	0.468
	A layer	0.140	0.021	0.090	1.105	0.043	0.104	0.531	0.067	0.494
B	*V layer*	0.115	0.063	0.232	0.038	0.152	0.509	0.299	0.145	0.521
	mid layer	0.025	0.050	0.198	0.030	0.099	0.459	0.032	0.116	0.477
	A layer	0.127	0.037	0.170	0.230	0.065	0.413	0.776	0.088	0.439
C	*V layer*	0.005	0.001	0.023	0.008	0.032	0.088	0.061	0.088	0.240
	mid layer	0.005	0.002	0.029	0.009	0.028	0.105	0.040	0.048	0.204
	A layer	0.035	0.010	0.036	0.033	0.027	0.119	0.145	0.052	0.117

Table 15: Circumferential stress(σ_{circ}) and radial stress (σ_{rad}) within the cross section of the LC leaflet at diastolic peak ($t = 380\,\text{ms}$). *V side* = ventricular layer of the leaflet surface. *mid plane* = middle layer of the leaflet surface. *A side* = aortic layer of the leaflet surface.

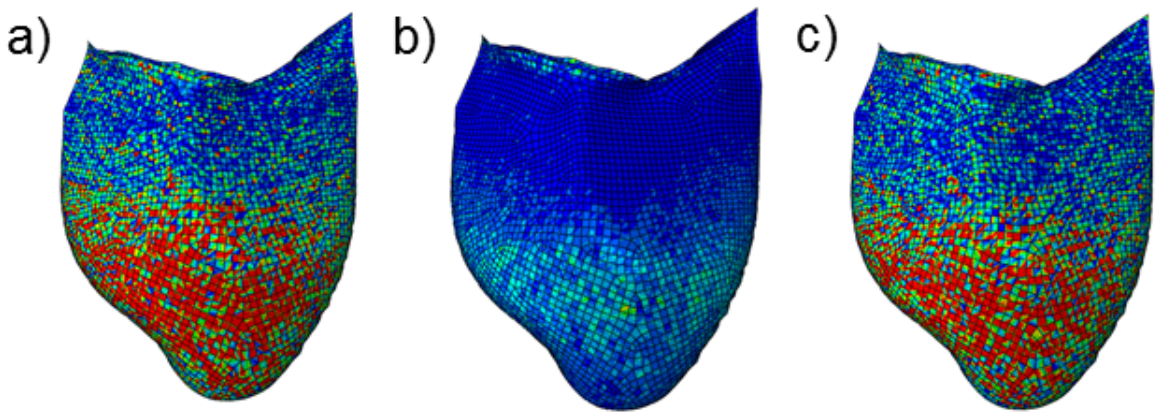

Figure 60: Stress distribution on the V side (a), mid-section (b) and A side (c) for the SH model of the AR1 LC leaflet.

The most evident stress gradient through the leaflet thickness was obtained at location A and B, consistently with the marked local curvature. Of note, in SH models the V side and the A side exhibited an even more patchy and noisy stress distribution as compared to the mid section (Figure 60); hence, side-to-side stress variations are not reliable in these models, and only results for 3D-HT and 3D-MT models can be considered reliable.

6.3.3 Mechanical response of the aortic root wall

The mechanical response of the AR wall is evaluated through the analysis of the max principal stress values at the aortic pressure peak ($t = 100\,\text{ms}$) (Table 16).

	SH	3D-HT	3D-MT
AR1	0.610	0.635	0.624
AR2	0.683	0.727	0.765
AR3	0.698	0.772	0.784

Table 16: Max principal stress at aortic pressure peak ($t = 100\,\text{ms}$) for each subject.

The three models of each subject exhibited similar values; this means that for the same aortic root geometry the mesh abopted for the leaflets discretization had not a strong impact on the variation in peak value of the max principal stress of the wall. In particular, each model of subject AR3 and AR2 showed higher wall stress value than the corresponding model of AR1; this implied that indipendently of the mesh abopted for the leaflets discretization, AR2 and AR3 present higher wall stress values due to the fact that their geometry was very irregular compared to the one of AR1, leading to the presence of areas with high stress concentration (Figure 61).
Once again, the differences found between the three subjects were representative of the anatomical inter-subject variability. Our results (Figure 61) were in agreement with the fact that our wall thickness, equals to 1.0 mm, was less thick than the physiological AR wall and consequently it produced stress values higher than the ones reported in literature [12].

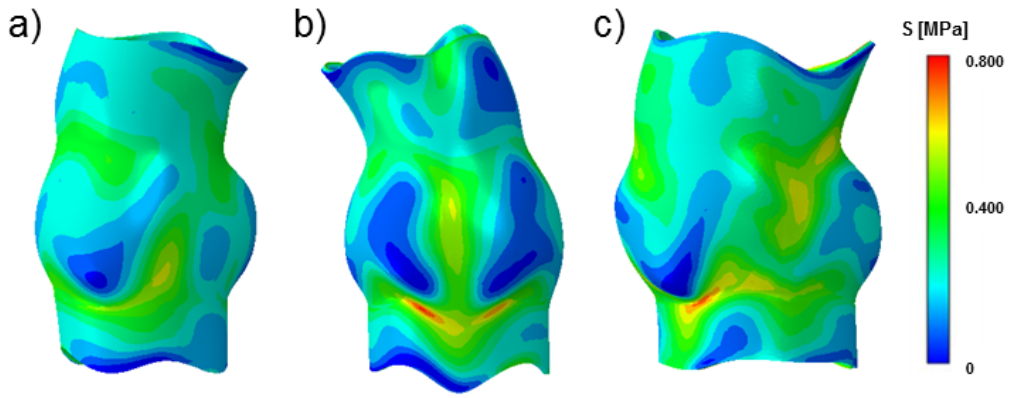

Figure 61: Max principal stress pattern at aortic pressure peak ($t = 100\,\text{ms}$) for each subject (a) AR1; b) AR2; c) AR3).

7 Conclusions and future developements

The principal novelty of this work is the development of an automated tool allowing for i) creating subject-specific, image-based AR geometrical models capturing fine anatomical details, ii) discretizing the reconstructed geometry obtaining a high quality mesh of hexahedral elements, iii) defining a space-dependent pattern of leaflet thickness, which can be tuned based on patient-specific data or on data from the literature, and iv) preparing the input files required to run the finite element simulations required to compute AR pre-stresses through an iterative process [35], and to simulate the structural response of the pre-stressed throughout the cardiac cycle. To the best of our knowledge, no previous work published in the literature combines these features.

Among these features, the second and third ones proved particularly relevant when computing aortic valve biomechanics, and in particular when assessing peak diastolic stresses on a preliminary cohort consisting in the ARs of three healthy volunteers. In a consistent and repeatable way, the simulations performed for the three ARs provided two main indications. On one hand, we compared their distribution computed when aortic valve leaflets were discretized into uniformly thick hexahedral elements and into uniformly thick shell elements, respectively. In the former case, the computed stress distribution was much more regular and consistent with the function fulfilled by the different leaflet regions. This first result strongly suggests that the use of hexahedral elements represents an advancement as compared to the more common use of shell elements. Moreover, when hexahedral elements were used the stress gradient through the leaflet thickness could be reliably computed, whereas this computation was not reliable when using shell elements. This second result has implications regarding a possible application of this type of models, i.e. the analysis of the different strain and stress levels characterizing the three aortic leaflet layers, which could be relevant to the better understanding of pathological processes such us the progression of calcific aortic valve disease.

On the other hand, we also compared the stress distribution computed when discretizing the valve leaflets into hexahedral elements with uniform and space-dependent thickness, respectively. In the latter case, the entity of computed stresses changed no-

tably; in particular, stresses experienced by the belly region, which was thinner when setting a space-dependent thickness distribution from the literature [12], were increased by up to 5-fold. This result highlights that, as expected, changes in leaflet thickness have a major impact of leaflet stresses. In the context of subject-specific AR structural modeling, the implication of this third result is that it should be mandatory to exploit image modalities that, differently from cMRI, allow for quantifying the subject-specific regional thickness of aortic valve leaflets, in that this is a key feature when quantifying aortic valve structural response. In this regard, 3D ultrasound imaging may represent a valuable option. Alternatively, age- and gender-matched, as well as class-matched (e.g. healthy valve, calcific valve, Marfan syndrome-affected valve) thickness patterns should be identified based on *ex vivo* measurements on cadavers or on tissue samples resected during surgical procedures.

Despite being an advancement of the state of the art, the modeling approach herein proposed could be further improved.

As far as geometrical reconstruction is concerned, the most important improvement should regard the generation of the solid model of the aortic wall. As explained in detail in Appendix A, with the current procedure wall thickness cannot be set to any reasonable value; if wall regions with a marked concavity towards their outward surface are present, in these regions the generation of hexahedral elements works only if relatively small values ($\leq 1\,\text{mm}$) are assigned to the wall thickness. Otherwise, "twisted" elements are generated. In order to overcome this limitation, the extrusion process implemented to generate the hexahedral elements should be modified. Alternatively, extra functions should be added to the developed script to correct *ex post* the twisted elements, for instance by manipulating the connectivity of the generated solid mesh.

As far as the modeling of tissues' mechanical properties is concerned, two improvements should be implemented in the future. The first one regards the modeling of aortic wall mechanical properties and would consist in moving from a linear, elastic and isotropic constitutive model to a hyperelastic and anisotropic model. Of note, this improvement would imply a major complication in the computation of AR pre-stresses in the initial geometrical configuration reconstructed from medical images. Currently, the computation of pre-stresses exploits the *INITIAL CONDITION keyword available in the com-

mercial solver used to perform the finite element simulations, i.e. ABAQUS/Explicit. However, this keyword is not compatible with the use of hyperelastic and anisotropic materials, and its exploitation become not trivial when simply a non-linear stress-strain behavior is assumed. As a result, a different method should adopted to compute pre-stresses. The second improvement regards the modeling of aortic valve stress-strain response: the different mechanical properties of the three layers composing the leaflets could be assigned to the different layers of the hexahedral mesh discretizing their geometry. This development would allow for moving towards a later specific structural analysis, and could pave the way towards multi-scale models aimed at quantifying the mechanical stimuli acting on the cell populations characterizing the different layers, which are supposed to play a role in different physio-pathological processes.

Appendices

A Wall full volume mesh creation issues

The creation of new nodes for the wall thickening procedure was performed using an extrusion process, where the original aortic wall nodes were copied and translated along the corresponding outward node normal. The simplicity of this technique allows to obtain a thicken wall in a short time with a simple copy procedure but, depending on the patient specific geometry of the AR, problems may occurs in some regions of the geometry. In some models it is possible to find very high radius of curvature in the 3D reconstruction: here the extrusion along the outward node normal is regulated by a threshold on the extrusion distance.

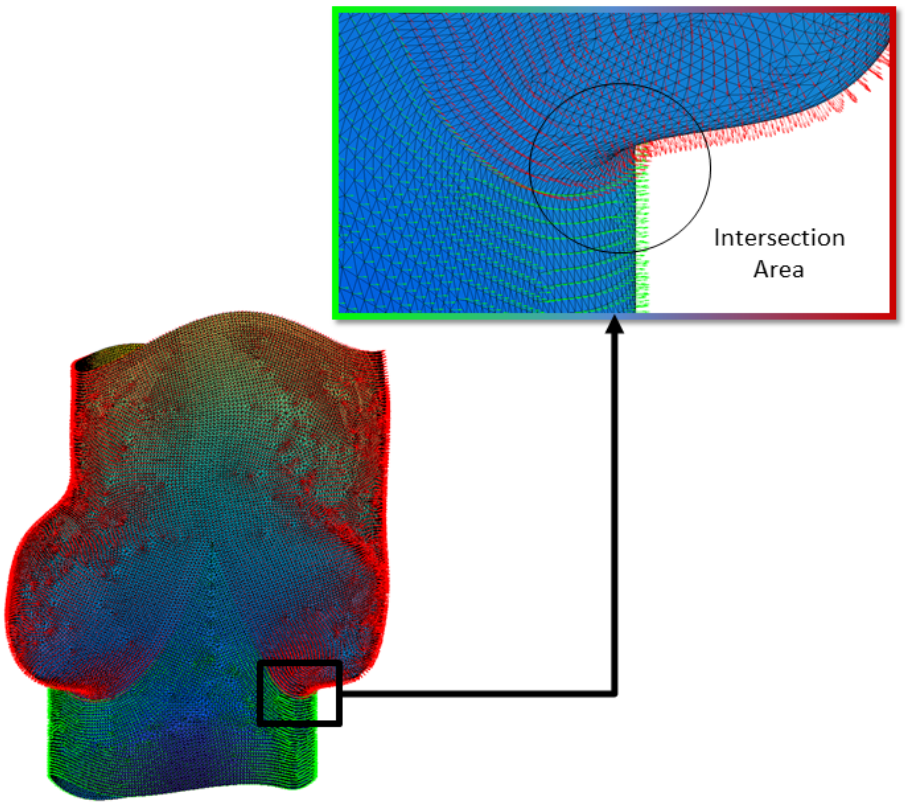

Figure 62: The red and green arrows represent the nodes normal along the entire AR wall. The intersection area is the region where there is a high risk that those vectors cross each other before a distance comparable with the AR wall mean thickness, $\sim 1.6\,\text{mm}$ [16].

As shown in Figure 62, in these regions the nodes normal cross each other after a

certain distance; this makes impossible to simply copy the nodes in the new position along the normal, because it would implies "twisted" elements with negative volumes.

B Hyperelastic theory equations

A material is said to be hyperelastic when the work performed by the stress state during the deformation process only depends on the initial configuration at time t_0 and on the final configuration at time t. The behavior of such a material can be described using a *potential function* U, with $U > 0$, representing the energy stored into the body during the deformation process.
Two principal formulation can be used to write U, the invariant-based formulation and the strain-based formulation.

Invariant-based: in this approach U is defined as a function of the invariant and pseudo-invariant of the right Cauchy-Green tensor $\boldsymbol{C}$:

$$\boldsymbol{C} = \boldsymbol{F}^T \cdot \boldsymbol{F}$$

where $\boldsymbol{F}$ is the deformation gradient. In this case the Cauchy stress $\boldsymbol{\sigma}$ are defined as follows:

$$\boldsymbol{\sigma} = \boldsymbol{F} \sum_{i=1, i\neq 3}^{N} (U_i \frac{\partial I_i}{\partial \boldsymbol{F}}) - p\boldsymbol{I}$$

where p is the Lagrangian multiplier, $\boldsymbol{I}$ the identity matrix and U_i is the partial derivatives of U respect to the i-th invariant I_i

$$U_i = \frac{\partial U}{\partial I_i}$$

Strain based: in this second approach the potential function U is defined as a function of the components of the Green-Lagrange tensor $\boldsymbol{E}$

$$\boldsymbol{E} = \frac{1}{2}(\boldsymbol{C} - \boldsymbol{I})$$

and the Cauchy stress are calculated as follows:

$$\boldsymbol{\sigma} = \boldsymbol{F} \frac{\partial U}{\partial \boldsymbol{E}} \boldsymbol{F}^T - p\boldsymbol{I}$$

C Energy balances

The energy balance parameters, ω_1 and ω_2, regarding the second cardiac cycle are reported for all models in the following pages, where:

$$\omega_1 = \frac{K}{E_i}, \quad \omega_2 = \frac{E_a}{E_i}$$

where K is the *kinetic energy*, E_i the *total internal energy* and E_a the *artificial strain energy*.

Dashed lines in the charts represents the threshold which assure a good consistency of the numerical data.

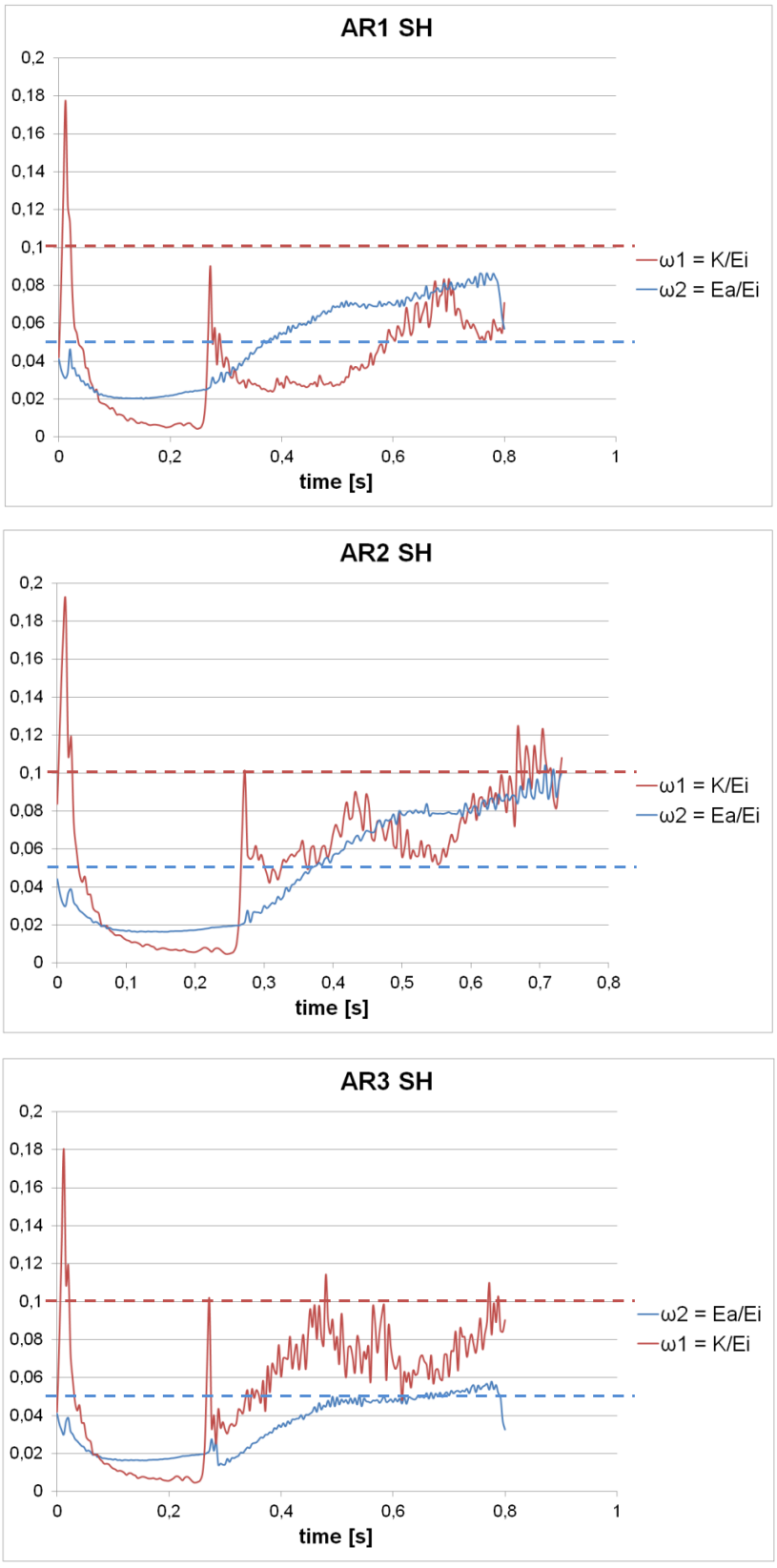

Figure 63: Energy balances for SH models. *Red* line: ω_1. *Blue* line: ω_2.

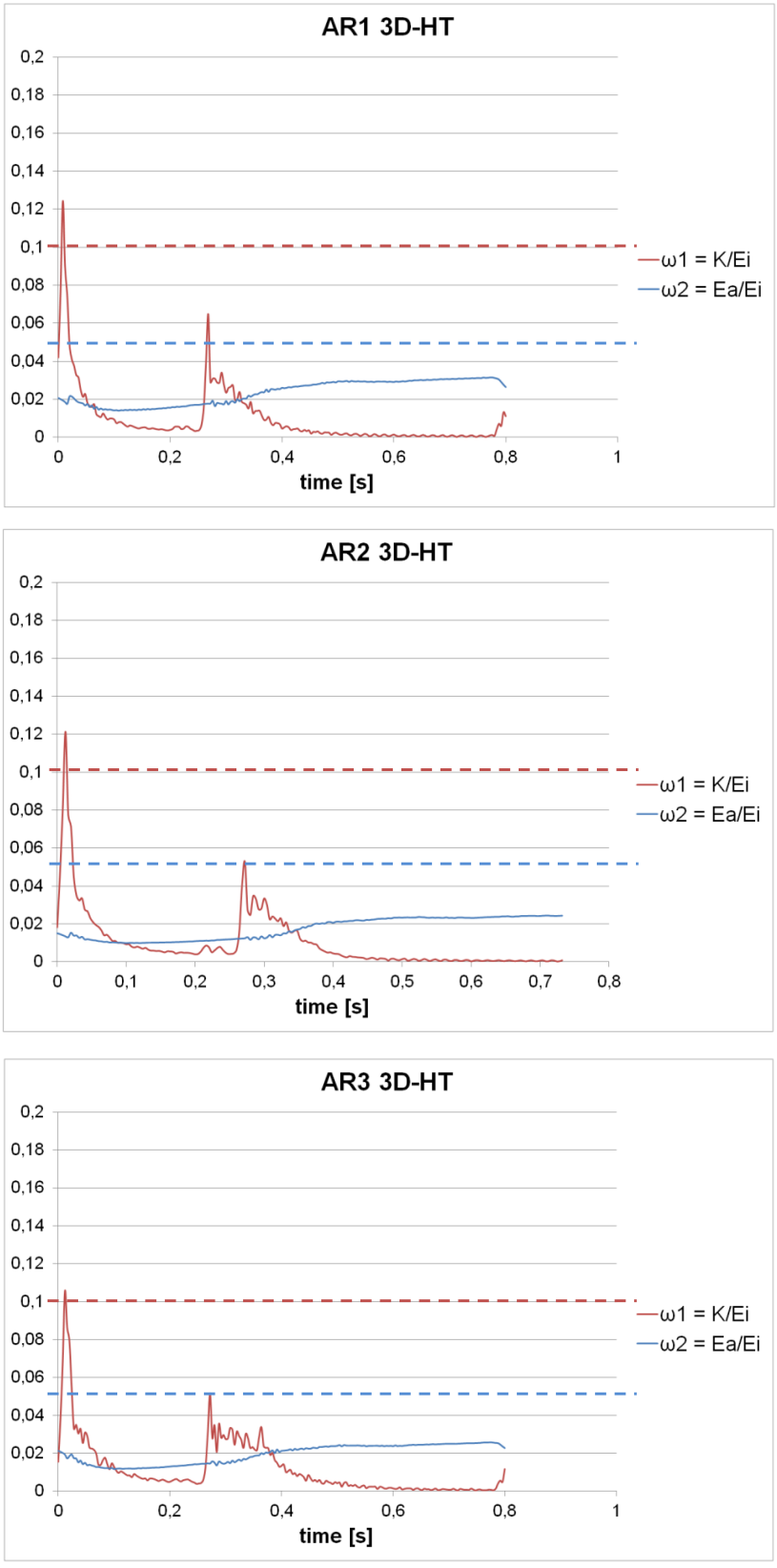

Figure 64: Energy balances for C3D8 models. *Red* line: ω_1. *Blue* line: ω_2.

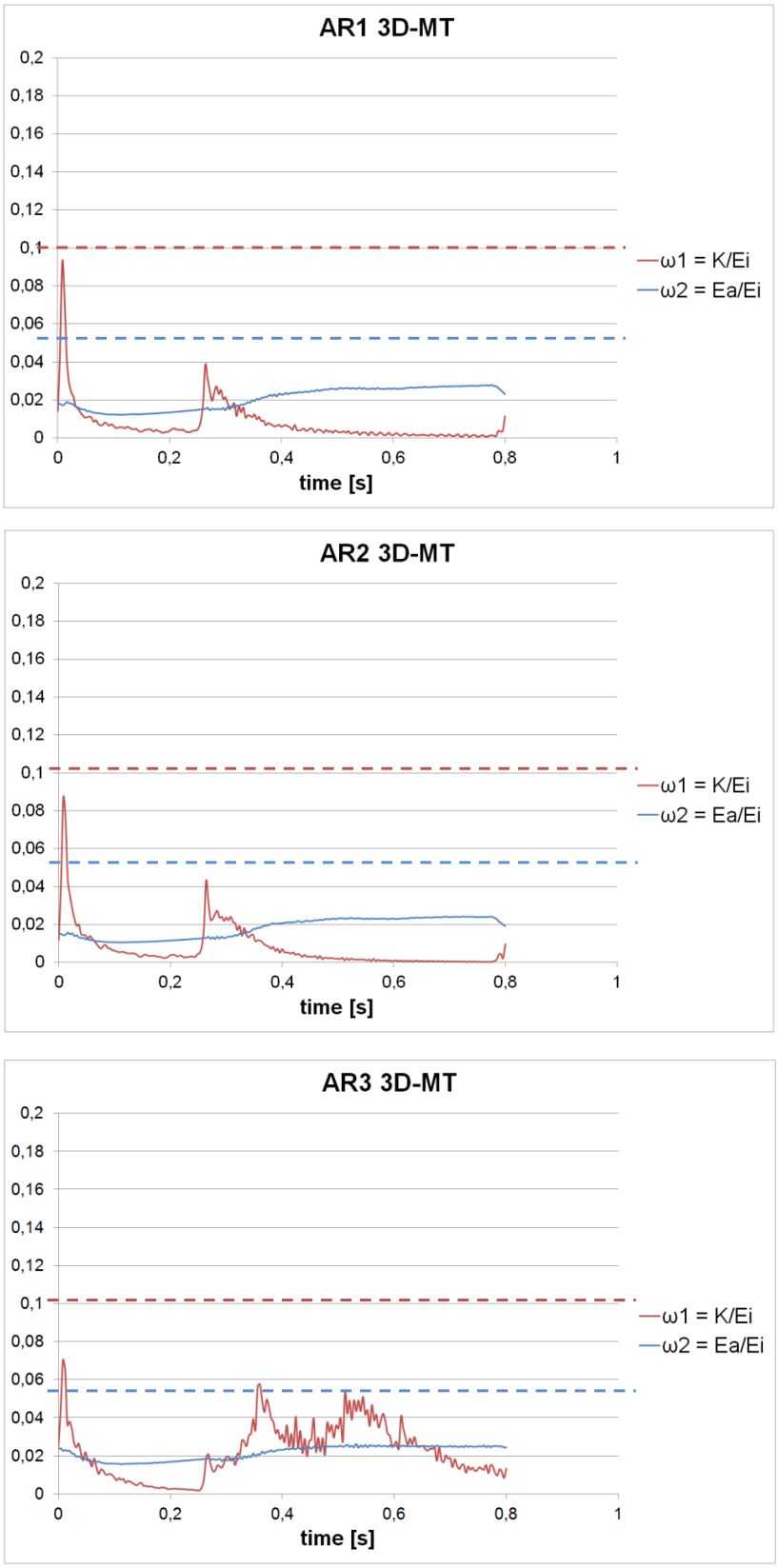

Figure 65: Energy balances for C3D8-M models. *Red* line: ω_1. *Blue* line: ω_2.

References

[1] ABAQUS. "6.10 Documentation, Abaqus Analysis User's Manual". In: *Dassault Systemes, Providence, RI, USA* (2010).

[2] Lajos P Berdajs D. "The anatomy of the aortic root". In: *Journal of Cardiovascular Surgery* (2002).

[3] Sacks MS Billiar KL. "Biaxial mechanical properties of the native and glutaraldehyde-treated aortic valve cusp: Part I, Experiment results". In: *J Biomech Eng* (2000).

[4] Sacks MS Billiar KL. "Biaxial mechanical properties of the native and glutaraldehyde-treated aortic valve cusp: Part II, A structural costitutive model". In: *J Biomech Eng* (2000).

[5] Rittgers SE Chandran KB Yoganathan AP. *Biofluid mechanics: the human circulation.* CRC press, 2007.

[6] Barratt-Boyce BG Christie GW. "Age-dependent changes in the radial stretch of human aortic valve leaflets determined by biaxial testing." In: *The Annals of Thoracic Surgery* (1995).

[7] Fung YC Chuong CJ. "Compressibility and constitutive equation of arterial wall in radial compression experiments". In: *Journal of Biomechanics* (1984).

[8] Atkins SK et al. "Bicuspid aortic valve hemodynamics induces abnormal medial remodeling in the convexiy of porcine ascending aortas". In: *Biomechanics and Modeling in Mechanobiology* (2014).

[9] Bierbach BO et al. "Aortic root and cusp configuration determine aortic valve function." In: *European Journal of Cardio-thoracic Surgery* (2010).

[10] Chandran KB et al. "Patient-specific bicuspid valve dynamics: overview of methods and challenges". In: *Journal of Biomechanics* (2013).

[11] Clark RE et al. "Scanning and light microscopy of human aortic leaflets in stressed and relaxed states". In: *Journal of Thoracic and Cardiovascular Surgery* (1974).

[12] Conti CA et al. "Dynamic finite element analysis of the aortic root from MRI-derived parameters". In: *Medical Engineering and Physics* (2010).

[13] Dagum P et al. “Deformational dynamics of the aortic root: modes and physiologic determinant”. In: *Circulation 100 (Suppl II)* (1999).

[14] Dreger SA et al. “Immunohistochemical characterization of the interleaflet triangle of the human aortic valve”. In: *Journal of Heart Valve Disease* (2003).

[15] Gnyaneshwar R et al. “Dynamic analysis of the aortic valve using a finite element model”. In: *Annals of Thoracic Surgery* (2002).

[16] Grande-Allen KJ et al. “Stress variations in the human aortic root and valve: the role of anatomic asymmetry”. In: *Annals of Biomedical Engineering* (1998).

[17] Guccione JM et al. “Passive material properties of intact ventricular myocardium determined for a cylindrical model”. In: *ASME Journal of Biomechanical Engineering* (1991).

[18] Gundiah N et al. “Asymmetric mechanical properties of porcine aortic sinuses.” In: *The Annals of Thoracic Surgery* (2008).

[19] Jermihov PN et al. “Effect of geometry on the leaflet stresses in simulated models of congenital bicuspid aortic valves.” In: *Cardiovascular Engineering and Technology* (2011).

[20] Jerminhov PN et al. “Effect of Geometry on the Leaflet Stresses in Simulated Models of Congenital Bicuspid Aortic Valves”. In: *Cardiovascular Engineering Technology* (2011).

[21] Kunzelman KS et al. “Aortic root and valve relationships: impact on surgical repair”. In: *Journal of Thoracic and Cardiovascular Surgery* (1994).

[22] Labrosse MR et al. “Geometric modeling of functional trileaflet aortic valves: development and clinical applications.” In: *Journal of Biomechanics* (2006).

[23] Labrosse MR et al. “Mechanical characterization of human aortas from pressurization testing and a paradigm shift for circumferential residual stress.” In: *Journal of the Mechanical Behavior of Biomedical Materials* (2013).

[24] Labrosse MR et al. “Subject-specific finite-element modeling of normal aortic valve biomechanics from 3D+t TEE images”. In: *Medical Image Analysis* (2015).

[25] Lansac E et al. “A four-dimensional study of the aortic root dynamics”. In: *European Journal of Cardio-thoracic Surgery* (2002).

[26] Mangini A et al. “The aortic interleaflets triangles annuloplasty: a multidisciplinary appraisal.” In: *European Journal of Cardio-thoracic Surgery* (2011).

[27] Mao S et al. “Normal Thoracic Aorta Diameter on Cardiac Computed Tomography in Healthy Asymptomatic Adult; Impact of Age and Gender”. In: *Academic Radiology* (2008).

[28] McDonald PC et al. “The challenge of defining normality for human mitral and aortic valves – geometrical and compositional analysis.” In: *Journal of Cardiovascular Pathology* (2002).

[29] Newman KM et al. “A hyperelastic constitutive law for aortic valve tissue”. In: *Journal of Biomechanical Engineering* (2009).

[30] Sacks MS et al. “On the biomechanics of heart function.” In: *Journal of Biomechanics* (2009).

[31] Sahasakul Y et al. “Age-related changes in aortic and mitral valve thickness: implications for two-dimensional echocardiography based on an autopsy study of 200 normal human hearts.” In: *Journal of Cardiology* (1988).

[32] Soncini M et al. “Aortic root performance after valve sparing procedure: a comparative finite element analysis”. In: *Medical Engineering & Physics* (2008).

[33] Sutton JP et al. “The forgotten interleaflets triangles: a review of the surgical anatomy of the aortic valve”. In: *Annals of Thoracic Surgery* (1995).

[34] Underwood et al. “The aortic root: structure, function, and surgical reconstruction”. In: *Heart* (2000).

[35] Votta E et al. “A novel approach to the quantification of aortic root in vivo structural mechanics”. In: *under review for the International Journal for Numerical Methods in Biomedical Engineering* (2016).

[36] Votta E et al. “Aortic Valve Repair via Neo-Chordae Technique: Mechanistic Insight Through Numerical Modelling”. In: *Annals of Biomedical Engineering* (2012).

[37] Weinberg EJ et al. “A computational model of aging and calcification in the aortic heart valve.” In: *PLOS ONE* (2009).

[38] Yacoub MH et al. “The aortic outflow and root: tale of dynamism and crosstalk”. In: *Annals of Thoracic Surgery* (1999).

[39] Netter FH. *Atlas of Human Anatomy.* Saunders, 2014.

[40] Holzapfel GA. “Determination of layer-specific mechanical properties of human coronary arteries with nonatherosclerotic intimal thickening and related constitutive modeling”. In: *American Journal of Physiology: Heart and Circulatory Physiology* (2005).

[41] Grasser TC Holzapfel GA. “A new constitutive framework for arterial wall mechanics and a comparative study of material models”. In: *Journal of Elasticity* (2000).

[42] Vesely I. “The role of elastin in aortic valve mechanics”. In: *Journal of Biomechanical Engineering* (1998).

[43] Vesely I Lo D. “Biaxial strain analysis of the porcine aortic valve”. In: *Annals of Thoracic Surgery* (1995).

[44] Presicce M. “Progettazione e implementazione di un nuovo algoritmo semi-automatico per la generazione di modelli ad elementi-finiti paziente-specifici di radice aortica: applicazione alla simulazione della biomeccanica in vivo della radice aortica fisiologica e affetta da bicuspidia valvolare congenita”. In: *Bioengineering, Politecnico di Milano – Master Thesis* (2015).

[45] Sun W Martin C. “Biomechanical characterization of aortic valve tissue in humans and common animal models.” In: *Journal of Biomedical Materials Research* (2012).

[46] Thubrikar MJ. *Geometry of the aortic valve.* CRC press, 1990.

[47] Sun W Sacks MS. “Multiaxial mechanical behavior of biological materials.” In: *Annual Review of Biomedical Engineering* (2003).

[48] Sacks MS Stella JA. “On the biaxial mechanical properties of the layers of the aortic valve leaflet”. In: *Journal of Biomechanical Engineering* (2007).

[49] Field ML Zhao AR. “Blunt trauma and acute aortic syndrome: a three-layer finite element model of the aortic wall”. In: *European Journal Cardio-Thoracic Surgery* (2008).

Acknowledgements

We would like to express our most sincere thanks to our supervisors Cesare Alberto Redaelli and Emiliano Votta; with their competence and passion they taught us not only biomechanical notions, but also the method to handle the projects and to solve the problems. A special thanks to Francesco Sturla who transferred us his devotion for the scientific research, following our work since the beginning with kindness and patience. Thanks also to Matteo Selmi who always had time for us and our "technical issues", and Emanuele Cattarinuzzi who helped us to face the difficult world of Abaqus.
We would also like to express our gratitude to all the people in the laboratory who have always been helpful and friendly with us. Thanks to the colleagues working on their thesis with us in the Cube: we shared the hardest moments of this work.
To conclude thanks to our families and friends, always supporting us to overcome all the difficulties. Thanks once again!